Exploring nanomagnets for quantum devices with NV magnetometry

Inauguraldissertation

zur

Erlangung der Würde eines Doktors der Philosophie

vorgelegt der

Philosophisch-Naturwissenschaftlichen Fakultät

der Universität Basel

von

Liza Žaper

2025

Genehmigt von der Philosophisch-Naturwissenschaftlichen Fakultät
auf Antrag von

Erstbetreuer: Prof. Dr. Martino Poggio
Zweitbetreuer: Prof. Dr. Patrick Maletinsky
Externe Expertin: Prof. Dr. Claire Donnelly

Basel, den 19.11.2024

Prof. Dr. Marcel Mayor
Dekan

Abstract

Focused electron beam induced deposition (FEBID) offers a promising single-step technique for patterning nanomagnets. In this thesis, we explore how nanomagnets for spin qubit control can be fabricated using FEBID. We extend our research by demonstrating how magnetic nanodots can be deposited on phononic membranes, potentially mediating interactions between an NV qubit and mechanical systems. To characterize these nanomagnets, we employ NV magnetometry. Additionally, we investigate magnetization textures in nanoscale permalloy dots, unveiling their intrinsic properties and contributing to their application in neuromorphic and spintronic technologies.

Acknowledgements

I am grateful to my supervisor Prof. Dr. Martino Poggio for the opportunity to conduct research in the laboratory of *Nanomechanics, nanomagnetism and nanoimaging* at the University of Basel. I appreciate his trust and encouragement of the vision for my doctorate, which would not have been possible without his support. I am grateful for his patience and kindness during the challenging moments. I also thank Dr. Floris Braakman for his guidance and thoughtful and patient discussions which were essential to the completion of this doctorate.

I would also like to thank Dr. Peter Rickhaus for his trust and the mentorship he provided during the initial stage of my doctorate. I appreciate the conversations I had the chance to have with him which enriched my perspective on science and research. Moreover, I am grateful for the trust and the opportunity to work beside him on interesting scientific challenges, including presenting our work in front of a highly respected community of researchers.

I would also like to thank the generous support of my second supervisor Prof. Dr. Patrick Maletinsky. I truly appreciate the inspiring discussions, his kindness and the opportunities to work on the room temperature setup in his group.

I would also like to thank Dr. Francesco Fogliano, Dr. Kousik Bagani, Dr. Estefani Marchiori, Luca Forrer, Aurèle Kamber, Simon Phillip, Gulio Romagnoli, Hinrich Mattiat, Andriani Vervelaki, Daniel Jetter, Matthias Claus, Lukas Schneider, David Jägger, Dr. Vicent Borras, Guillaume Clement and Dr. Patrick Hsia for the fun moments together.

I thank the Swiss National Science Foundation (SNSF) for the financial support to carry out my doctorate.

Finally, I would like to thank my friends and family for their continuous support.

Basel, December 2, 2025 *Liza Žaper*

Contents

1 Introduction

On December 29th, 1959, during the annual meeting of the American Physical Society at Caltech, the renowned physicist Richard Feynman introduced the concept that would eventually evolve into the field of nanotechnology [1]. His visionary ideas have inspired scientists and researchers for decades. Feynman posed a groundbreaking question: *"What would happen if we could arrange the atoms one by one the way we want them?"* This inquiry not only challenged the prevailing scientific paradigms of his time but also catalyzed efforts that will later manifest as advancements in materials science, molecular biology, and numerous other disciplines [2].

Over 60 years later, this thesis echoes Feynman's vision by posing a new question in the context of the modern data revolution: *"In a world where data is generated at an unprecedented rate, the need for faster and more efficient storage solutions has never been greater. But how can we push beyond the limitations of current technologies?"*

Nanoscience is concerned with phenomena occurring in objects with dimensions ranging from 1 nm to 100 nm [3]. This size range encompasses many viruses and molecules, and it also represents the characteristic length scale of numerous physical processes [4]. Today's integrated circuits are constructed using gates within this nanoscopic range [5, 6], and memory arrays are built on nanometer-scale units. From a fundamental perspective, materials at the nanoscale exhibit behaviors that differ significantly from their bulk counterparts when one or more dimensions are reduced to this size. The increased proportion of surface atoms in nanostructures leads to fascinating phenomena, with various forces scaling differently compared to bulk materials. These properties open doors to innovative applications in medicine, electronics, and molecular biology [7, 8, 9, 10, 3].

Nanomagnetism, a specific area within nanoscience, focuses on the magnetic properties of structures in this nanoscopic range. While structures between 100 nm and 1000 nm are referred to as mesoscopic [3, 11], this thesis primarily focuses on nanoscopic structures. However, mesoscopic structures are also considered in order to understand general material properties such as magnetization saturation. Nanomagnetic systems can exist in various forms, including thin films and multilayers (2D), nanoparticles (0D), nanowires and nanotubes (1D), as well as nanodisks, nanodots, and nanorings (2D or quasi-2D). Each of these structures, despite being classified by size, exhibits significant differences in geometry, physical properties, and potential applications [3, 12].

Of particular interest in this work are magnetic nanowires and nanodisks, which have promising applications as bit-units in high-density memory arrays [13, 14, 15], for spin qubit control and as mediating elements for fundamental experiments in magneto-mechanics. Nanotubes and nanorings, on the other hand, offer potential for information storage and processing through magnetic domain-wall motion [3]. These unique characteristics in low-dimensional systems present widespread opportunities for advancing memory technology.

The progress Feynman envisioned is increasingly visible today, especially in the rapidly advancing field of quantum computing. Exploiting quantum-mechanical properties of confined electrons or holes in semiconductor devices, and constructing suitable nanomagnets to encode quantum information, offers a revolutionary avenue for increasing computing efficiency. This thesis will address how such nanomagnets can be built and characterized for use in spin qubit control and future single-spin magneto-mechanics experiments. In addition, nano-printing techniques will be used to fabricate these magnets, and their properties will be analyzed using atomic-based sensing methods, such as NV center magnetometry.

By answering these questions, this thesis contributes to the growing body of research on nanomagnets for spin qubit control and adds to the research surrounding material science for spintronics [16, 17], as well as an innovative approach in building a system for investigating fundamental physics of spin-mechanical interactions. Furthermore, it highlights potential future directions for research in the pursuit of more efficient and sustainable technologies, by using 3D-nano-printing [18, 19] and cryo-FEBID [20], aligning with Feynman's original vision and the demands of the modern world.

2 Fundamental physics

2.1 Introduction to magnetism

Magnetism is a complex phenomenon arising from the quantum-mechanical interaction between one-electron and multi-electron effects. Materials are fundamentally classified into distinct regimes based on their magnetic response to an external field, leading to categories such as diamagnetism, paramagnetism and ferromagnetism.

Diamagnetic materials (e.g., gold, water and silver) exhibit paired electrons and generate a magnetic moment that weakly opposes the applied field. Paramagnetic materials (e.g., aluminum, magnesium, and oxygen) contain unpaired electrons, causing a weak alignment with the applied field.

The focus of this thesis is ferromagnetism (e.g., cobalt, nickel, and iron). In these materials, a strong exchange interaction causes the magnetic moment of many unpaired electrons to align spontaneously, resulting in long-range magnetic order. This cooperative alignment creates magnetic domains, which are responsible for the material's strong attraction to magnets and the ability to retain permanent magnetization.

Another distinctive feature is the materials temperature dependence. Curie temperature T_C is a temperature at which the spontaneous magnetization arising from the alignment of the atomic magnetic moments depends on temperature, and at this temperature it falls to zero. It is often used to indicate the stability of the magnetisation saturation.

A ferromagnetic material's response to an external magnetic field is a nonlinear response of magnetization $\mathbf{M}$ to an applied magnetic field $\mathbf{H}$. Magnetization is the magnetic dipole moment per unit volume of material, and it is measured in the same units as the H-field, in amperes per metre ($\mathrm{A}m^{-1}$) [11].

2.2 Physics of micromagnetism

2.2.1 Energy balance

In this Section, we follow [11], [10] and [21].

2.2.2 Total energy

The total energy of a magnetic system can be described using the micromagnetic theory framework as [22]:

$$E_{tot} = E_{ex} + E_a + E_d + E_z + E_{strs} + E_{ms} \tag{2.1}$$

The first three terms: the exchange (E_{ex}), anisotropy (E_a) and dipolar (E_d) energy are always present. The Zeeman energy contribution comes from the application of an external magnetic field on a ferromagnet, and the last two terms result from stress and magnetorestriction.

2.2.3 Exchange energy

Exchange energy is a quantum mechanical effect that arises from the tendency of ferromagnetic materials to align their magnetization in a single direction, known as spontaneous magnetization. Any deviation from this alignment incurs an energy cost, as described by the following equation:

$$E_{ex} = \int A(\nabla e_M)^2 d^3r \tag{2.2}$$

where $e_M = \mathbf{M}(\mathbf{r})/M_s$ is the unit vector along the local direction of the magnetization, and A is the exchange stiffness. This constant, approximately given by $A \propto JS^2Z_c/a_0$, is proportional to the exchange constant J and the number of atoms per unit cell, Z_c, with a_0 being the lattice parameter.

The expression is derived from the classical Heisenberg Hamiltonian for two neighboring classical spins, S_i and S_j, which models the exchange interaction between indistinguishable particles. Thus, exchange is fundamentally a short-range phenomenon.

It is described using the spin operators as:

$$E_H = -\frac{1}{2}\sum_{ij} J_{ij}\mathbf{S}_i \cdot \mathbf{S}_j,$$

where E_H is the Heisenberg Hamiltonian, and it is minimized when spins align in parallel ($\mathbf{S}_i \parallel \mathbf{S}_j$). The so-called exchange integral J leads to ferromagnetism when positive, and to antiferromagnetism when negative.

2.2.4 Anisotropy energy

Magnetocrystalline anisotropy arises from spin-orbit coupling. Depending on the crystal structure of the ferromagnet, it is often energetically favorable for the magnetization to align along one or more specific axes. The ferromagnet reaches a local energy minimum when its magnetization is aligned along the easy axis.

$$E(\mathbf{M}) = E(-\mathbf{M}) \tag{2.3}$$

In the simplest case, where the specimen displays uniaxial anisotropy, the energy can be reduced to the following expression:

$$E_a = \int K_1 sin^2(\theta) d^3r + \int K_2 sin^4(\theta) d^3r \tag{2.4}$$

where Θ is the angle between the easy axis and the actual magnetization direction, and K_1 and K_2 are the first and second order anisotropy constants, respectively, which can be experimentally determined. These constants are temperature-dependent, and thus, higher-order terms are usually neglected, as they are only relevant at low temperatures.

It is important to note that any other forms of anisotropy are not considered in this energy term, such as shape anisotropy or surface-induced anisotropies.

Dipolar energy is the energy resulting from dipole-dipole interactions between the magnetic moments. This energy tends to favor arrangements where the dipole moments are aligned in a way that reduces the long-range magnetic interactions. Typically its effect is visible in the formation of domains and domain walls in the material. The energy evolves as a consequence of externally applied field, or in the case of the absence of the field, on the previous magnetic field direction and value applied.

Since $\mathbf{B} = \mu_0(\mathbf{M}+\mathbf{H})$ and $\nabla \cdot B = 0$, then $\nabla \cdot \mathbf{H}_d = -\nabla \cdot \mathbf{M}$, where H_d is the demagnetizing field.

The energy related to the stray field is:

$$E_d = -\frac{1}{2} \int \mu_0 \mathbf{H}_d \cdot \mathbf{M} d^3r \tag{2.5}$$

The factor of 1/2 arises from the reciprocity principle, as the magnetic field is generated by the spins within the material. Due to the long-range nature of this interaction, it leads to significant effects like shape anisotropy. In non-spherical particles, the demagnetizing field varies in different directions, resulting in one or more easy axes.

As an approximation, the demagnetization energy can be expressed as:

$$E_d = -\frac{\mu_0}{2} N M_S V \tag{2.6}$$

The demagnetizing factor, which varies based on the geometry of the system, is a critical determinant of the overall anisotropy in ferromagnetic materials. The contribution of demagnetization energy is particularly relevant in numerous applications. Magnetocrystalline anisotropy, for instance, underlies the distinction between magnetically hard and soft materials. Materials with high magnetocrystalline anisotropy are typically more resistant to demagnetization and are commonly classified as hard magnetic materials, a necessary characteristic in applications such as permanent magnets. Conversely, soft magnetic materials, or superparamagnetic materials that exhibit no magnetization in the absence of an external field, are of particular importance in biomedical applications.

Thus, magnetocrystalline and shape anisotropy play pivotal roles in the design of ferromagnetic materials with tailored properties. Each form of anisotropy provides a degree of control that can be exploited to engineer specific magnetic configurations for various technological purposes.

2.2.5 External energy and stress contributions

Among the other energy terms, Zeeman energy (E_z) is used to describe the interaction between the ferromagnet and the externally applied magnetic field. It can be expressed as:

$$E_z = -\int \mu_0 \mathbf{H}_{ext} \cdot \mathbf{M} d^3 r \tag{2.7}$$

If there is an external stress σ applied to the sample, it can give rise to another energy term (E_{str}):

$$E_{str} = -\sum_{i,j} \sigma_{ij} \epsilon_{ij} \tag{2.8}$$

ϵ_{ij} is the magnetoelastic strain tensor. Correspondingly, local stress can cause magnetorestriction in the material. The relevant energy (E_{ms}) is defined as:

$$E_{ms} = \frac{1}{2} \int (p_\epsilon - \epsilon) \cdot c \cdot (p_\epsilon - \epsilon) d^3 r \tag{2.9}$$

where p_ϵ is the deviation from the magnetorestrictive state, ϵ is the strain in the freely deformed state and c is the elastic tensor [11].

2.3 Physics of quantum devices

In this section, we follow [23, 24].

2.3.1 Zeeman splitting

Electron spin qubit is a foundational representation of a qubit. Qubit has quantum mechanical spins states which split due to the Zeeman interaction once a magnetic field is applied. In the presence of a magnetic field, the states split to up and down, and their splitting is defined as the Zeeman splitting: [23, 25]

$$\Delta E = hf = g\mu_B B \tag{2.10}$$

where g is the electron g-factor, μ_B is the Boltzmann constant, and B is the magnetic field.

2.3.2 The notation of a qubit

We can define the qubit state based on the physical qubit states. When an electron is in a state up $|\uparrow\rangle$ or down $|\downarrow\rangle$, the qubit state is in a state $|1\rangle$ or $|0\rangle$. These definite states are defined in information theory and they are classical states. The lowest energy state in a physical qubit corresponds to a 0 while the highest energy state in a physical qubit corresponds to 1. These states can also be in a superposition state. In a physical qubit, this can be a superposition of spin up and spin down:

$$|\psi\rangle = \alpha\,|\uparrow\rangle + \beta\,|\downarrow\rangle \tag{2.11}$$

In a qubit, its equivalent is a superposition of 1 and 0:

$$|\psi\rangle = \alpha\,|1\rangle + \beta\,|0\rangle \tag{2.12}$$

2.3.3 Phase of a qubit

Over time, the spin up state will acquire a phase relative to spin down state defined by the magnetic field (see eq.2.10). The frequency which defines this phase is called the Larmour frequency. Hence, once a qubit is in a superposition state, the phase is

accumulating with time. The phase is a significant parameter in understanding qubit devices. When a quantum algorithm is applied, and an operation is performed, we need to be able to track the phase with high precision to ensure high-fidelity operation. Inherently, there are experimental drawbacks that can lead to a phase delay which causes the loss of phase information. Some examples of phase loss causes can be imprecision of the oscillator clock in the equipment or environmental noise. This noise can come from the qubit device or it can come from the outside environment. For example, magnet which is used to create a magnetic field can fluctuate over time and create changes in the Larmour frequency, resulting in a phase that fluctuates over time.

Qubit control is achieved by applying time-dependent microwave pulses to drive a transition between the qubit states, performing a rotation on the spin state (e.g., a $\pi/2$-pulse for Hadamard, or a π-pulse for spin flip). This pulse sequence manipulates the qubit state by inducing an accumulated phase during the operation time. The maximum duration for which the qubit can remain in a superposition state and retain this phase information before losing it to environmental interactions is defined by the coherence time (T_2). For any reliable operation, the gate time must be much shorter than T_2. The operational quality of the control pulse sequence its reliability is separately quantified by the Gate Fidelity (F), a figure of merit that measures how accurately the executed operation matches the ideal quantum gate.

2.3.4 Electron confinement

The first requirement for realizing a solid-state spin qubit is the creation of a highly localized potential well to confine a single electron. This is achieved using a material system, such as the heterostructures Si/SiGe or Ge/SiGe where the precise control over the material interfaces and band alignments enables the formation of quantum dots capable of hosting the electron's charge in one region. By applying a voltage to the electrostatic gates, one can create a potential well, thereby forming a quantum dot that traps a single electron. The confinement quantizes the electron orbital motion. The electron states within this dot form a qubit with up $|\uparrow\rangle$ and down $|\downarrow\rangle$ states.

Valley splitting:
Within this work, we will be discussing the implementation of nanomagnets for $Si/Si0_2$ devices. In silicon-based systems, the valley splitting plays a fundamental role. Silicon has a conduction band with six degenerate energy minima, which we call valleys. These valleys can split into different energy levels when silicon

is confined in quantum well, especially at the interfaces. The reason is that the confinement and strain can lift the degeneracy, thereby creating energy branching. If the energy splitting between the two lowest levels is too small, the electron could occupy a higher valley state. This is degree of freedom, related to the valley/orbital splitting, can interfere with the spin state, leading to fast decoherence and poor gate fidelity. To ensure this is avoided, we need to have a valley splitting much larger that the thermal energy ($\Delta E_v >> k_B T$) and the Zeeman splitting, in order to ensure the electron is safely confined to the robust ground state.

Spin-orbit interaction (SOI):
Another fundamental effect that takes place in silicon materials is the spin-orbit coupling (SOI). It is a relativistic effect which couples the electron orbital motion and its spin. We study this effect because it is the origin of decoherence, which we explained as a coupling between the spin and environmental charge noise. Silicon exibits a weak instrinsic SOI, compared to other solid-state material systems, such as GaAs, leading to long decoherence times. In this work we focus on the application of magnets for spin rotation, however, in some other cases, one can use the SOI to perform single-qubit operation, in electron-spin dipole resonance (EDSR) experiments, as an example.

3 Technical and experimental background

This chapter provides an overview of the experimental techniques and methods used in the subsequent chapters. We begin by introducing the technique used for developing nanomagnets: Focused-Electron-Beam-Induced Deposition, and explain its basic working principle in detail. The application of Scanning NV magnetometry for characterizing the magnetic properties of the nanomagnets will be explored in later chapters, while here, we outline the underlying physical principles that enable its diverse uses. Finally, we conclude with a description of the characterization setups employed in the measurements.

3.1 Focused-electron-beam-induced deposition (FEBID)

3.1.1 Fundamental principle

Focused-electron-beam-induced deposition is a lithography technique that allows the definition of patterns on a substrate using electron beams [26, 27]. In this thesis, we employ FEBID to fabricate magnetic nanostructures, with a particular emphasis on cobalt-based nanostructures. First, a precursor molecule containing cobalt, Co_2CH_8, is introduced inside a chamber pumped to a high vacuum. Irradiating the precursor molecules adsorbed on the sample surface with an electron beam causes them to decompose, leaving the nanostructured Co deposits on the exposed areas of the sample substrate [28]. By directing the beam using a scanning electron microscope, this technique can be used to, in a single step, pattern Co nanodeposits with high resolution [29, 30]. The schematic of the deposition is shown in Fig.3.1. The technique is suitable for the definition of patterns in the nanometre or micrometer range [26, 30]. While electron microscopes can achieve remarkable imaging resolution, such as the 59 pm reached in an aberration-corrected TEM using electron ptychography [31], this should not be confused with the resolution for direct material deposition. The resolution of techniques like focused electron beam induced deposition (FEBID) is governed by factors beyond the electron beam's spot size, including the properties of the precursor and the generation of secondary electrons. For this reason, the typical resolution for depositing cobalt is on the order of tens of nanometers. Our work utilizes the FEI Helios NanoLab system, which has an imaging resolution of 0.8 nm at 15 kV and 1.5 nm at 200 V [32].

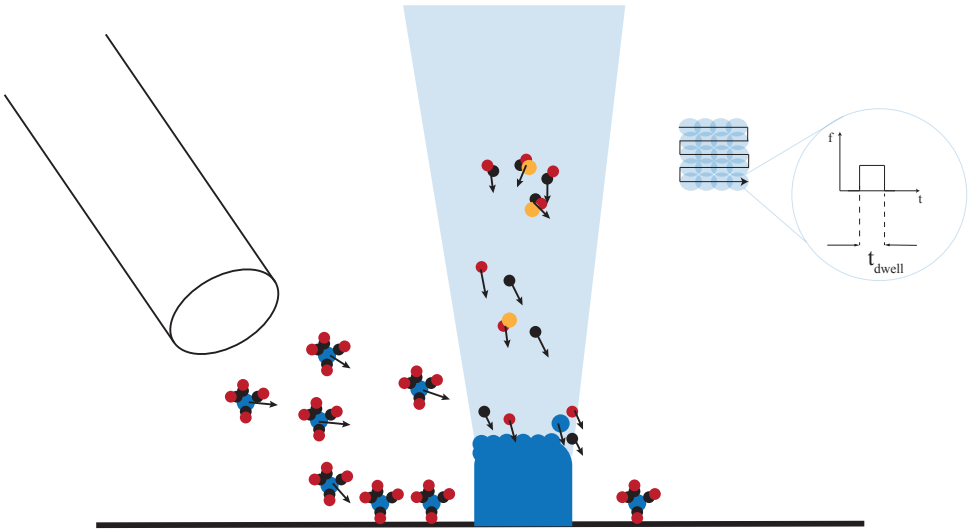

FIGURE 3.1 — Illustration of the working principle of FEBID fabrication technique. First, a precursor molecule containing cobalt, Co_2CH_8, is introduced inside a chamber pumped to a high vacuum. Irradiating the precursor molecules adsorbed on the sample surface with an electron beam causes them to decompose, leaving the nanostructured Co deposits on the exposed areas of the sample substrate. By directing the beam using a scanning electron microscope, this technique can be used to, in a single step, pattern Co nanodeposits with high resolution. [29]

3.1.2 Interaction mechanisms

As outlined in [33], we proceed by describing the interaction mechanisms of the FEBID process. In general, there are three types of interactions that occur during the deposition: substrate-precursor interaction, electron-substrate interaction, and electron-precursor interaction.

Substrate-precursor

Substrate-precursor molecules are characterised by the interactions of: diffusion, adsorption, and desorption. Adsorption of the precursor molecule can occur as chemisorption or physisorption depending on the combination of precursor molecule type, substrate material, and temperature. Further, the time the precursor molecule resides on the substrate affects the dissociation mechanisms, where a longer residence time τ[1] gives a higher probability of dissociation by the incoming or emitted electrons. The exact state of the surface and the vacuum are typically unknown when the deposition starts because FEBID is typically performed in pressure ranges that are below UHV. Once the deposition starts, the interaction transitions from precursor-surface to electron-substrate interaction.

[1]The residence time is defined as the time a molecule, reversibly adsorbed, spends on a surface before undergoing chemical reaction or desorption. From [34].

Electron - substrate

We will examine the interactions between the electron beam and the substrate. At the outset of the FEBID experiment, a beam of primary electrons (PEs) is focused onto a clean substrate. In a simplified view, these PEs collide with the solid material, causing them to deviate from their original path. When an inelastic collision occurs, a portion of the PEs initial energy is transferred to other electrons within the solid, which then interact with the material and scatter. The electrons generated in this way are categorized as secondary electrons (SEs) if their energy upon exiting the substrate is less than 50 eV, or as backscattered electrons (BSEs) if their energy exceeds 50 eV. The distance these electrons travel between collisions (mean free path) depends on their energy. Due to the numerous collisions, a volume of scattering events forms within the solid beneath the irradiated spot, often described as ”onion-shaped”. The shape and size of this volume are determined by the energy of the PEs and the nature of the substrate. From this volume, SEs and BSEs can escape the substrate and enter the vacuum, creating an energy spectrum and a spatial distribution of emitted electrons on the surface around the irradiated spot [33]. Monte Carlo simulations have been developed to model this process [35, 36, 37, 38]. Precursor molecule dissociation can occur whenever an electron crosses the interface between the substrate and the vacuum. The situation is further complicated by the fact that both the shape and composition of the target often change during the FEBID experiment. For example, in beam-induced deposition, a pillar may grow, causing the electron scattering volume to become increasingly confined to the pillar as it extends. Additionally, electrons, such as forward scattered electrons (FSEs), can repeatedly cross the target-vacuum interface. This electron scattering leads to a continuous energy transfer from the primary electrons (PEs) to the substrate or the growing structure, potentially resulting in e-beam-induced heating. Moreover, if the target is electrically non-conductive, a disparity between the incoming PEs and outgoing secondary electrons (SEs) and backscattered electrons (BSEs) can cause the sample to charge.

Electron - precursor

Finally, there is the interaction between electrons and precursor molecules, with dissociation being the most critical process for this discussion. E-beam-stimulated desorption can also occur. The probability of an electron breaking a bond in a precursor molecule depends on the electron energy and is typically represented by a cross-section ($\sigma(E)$, measured in cm^2). A larger cross-section indicates a higher probability of bond breakage. However, determining the cross section for dissociating adsorbed molecules is complex, as it depends on various factors, including the

bond energy within the molecule and the surrounding environment. Several studies have shown that secondary electrons (low-energy electrons) are the most significant contributors to the deposition process. Nevertheless, higher energy electrons can also contribute to the growth, for instance, by dissociative ionization. The studies of these mechanisms are continuously ongoing and at the moment no definite conclusions can be made. Moreover, along with influencing the growth rates, the dissociation processes can influence the composition of the deposit. In the ideal case, all carrier groups desorb and only the target material, in our case, Co for precursor molecule $Co_2(CO)_8$ would remain in the deposit. However, as shown by TEM later in the thesis, and by numerous studies, this is not the case. If we consider all these effects, it is to be concluded that there are many factors involved in the deposition process. Several factors come into play, including the electron flux, the energy spectrum of electrons crossing the substrate-vacuum interface, the spatial distribution of electron scattering in the irradiated target, and the cross-section of the precursor as a function of electron energy. Additional considerations include the precursor's adsorption behavior (physisorption or chemisorption), its residence time on the substrate, electron-stimulated desorption, e-beam induced heating, gas flux, the orientation of the precursor source with respect to the deposition spot, the geometry of the deposit or the surface, available chemical reaction pathways, background pressure and composition, and the thermal and electrical conductance of the substrate and the deposit. All of these factors act simultaneously, in and around the irradiated area. These factors are interconnected, and because the shape changes during the deposition, their mutual dependence is also dynamic. Moreover, since most of the deposition occurs under pressures that are not UHV, a lot of the parameters are unknown and/or uncontrolled. Therefore, the interplay of all these factors can result in unexpected phenomena, or behavior that isn't fully consistent with the existing studies [33].

3.1.3 Theoretical model

Following the explanation of the process as described in eq.3.1.2, we can observe a simple model suggested by Scheuer et al. [39]. It is to be noted, that the complexity of the process goes beyond this model since not all the parameters can be considered theoretically before the experiment.

We define the precursor molecule coverage $N(cm^{-2})$, which depends on the number of molecules that get adsorbed from the gas phase, the number of molecules that are decomposed by the e-beam, and the number of molecules that desorb to the gas

phase. It follows:

$$\frac{dN}{dt} = gF\left(1 - \frac{N}{N_0}\right) - \sigma(E)NJ - \frac{N}{\tau} \tag{3.1}$$

where g is the sticking factor, $F(cm^{-2}s^{-1})$ the gas flux arriving at the substrate, and $N_0(cm^{-2})$ the available adsorption site density in a monolayer, J (electrons $s^{-1}cm^{-2}$) the current density, and $\tau(s)$ the residence time of precursor molecules on the surface. We consider the following simplifications: for $\sigma(E)$, its value is unknown and we will consider its integral value σ. Further, in reality, the current density J is a sum of three components; J_{PE}, J_{BSE} and J_{SE}, which are the primary electron, backscattered electron, and secondary electron current densities, respectively. Since J_{BSE} and J_{SE} are typically not measured during experiments, we assume that $J = J_{PE}$.

In steady-state, the coverage N is reached when $\frac{dN}{dt} = 0$, from where:

$$N = N_0\left(\frac{\frac{gF}{N_0}}{\frac{gF}{N_0} + \sigma J + \frac{1}{\tau}}\right) \tag{3.2}$$

If we define the growth rate $R(cms^{-1})$ as:

$$R = V_{molecule}N\sigma J, \tag{3.3}$$

where $V_{molecule}(cm^3)$ is the volume of the deposited molecule, when substituting eq.3.3 in eq.3.2, it follows:

$$R = V_{molecule}N_0\frac{\left(\frac{gF}{N_0}\right)\sigma J}{\left(\frac{gF}{N_0} + \sigma J + \frac{1}{\tau}\right)} \tag{3.4}$$

3.1.4 Growth parameters

The main parameters that govern the writing process are the primary energy beam voltage V_{acc} (acceleration voltage), the beam current I, the time for which the beam is kept constant on a particular point on the surface, the dwell time t_{dwell}, the distance between neighboring dwell points, the pitch p, and the number of loops for which the writing pattern is repeated, n_L (see Fig.3.1). Other relevant parameters are the beam pattern, or the geometry of the writing path, i.e. serpentine, spiral, or zig-zag, as the most commonly used, and the replenishment time, which is the period between consecutive writing loops for which the writing is paused t_r [40].

Following the method described in [33] we. continue the discussion from Section 3.1.3. More insight into the deposition process is given when we look into two simplified cases. For simplicity, we neglect desorption in eq.3.4, assuming $\tau \gg 1$. From there, two regimes can be defined, from where eq.3.4 is reduced to:

$$\frac{gF}{N_0} \gg \sigma J, R = V_{molecule} N_0 \sigma J \tag{3.5}$$

and:

$$\frac{gF}{N_0} \ll \sigma J, R = V_{molecule} gF \tag{3.6}$$

From eq.3.5, the growth rate is limited by the current density, and it is independent of the gas flux. This case is defined as the **electron-limited regime**. In the eq.3.6, the growth rate is determined by the number of molecules arriving at the irradiated area and it is independent of the current density. This regime is referred to as the **precursor-limited regime**. The growth rate is frequently studied in the literature because it indicates the rate of the contamination growth in an electron optical system, to find suitable conditions for practical applications, or for the fundamental studies of the deposition process. It can also be noted that in the literature, some parameters indicate the growth rate, e.g. some authors report $V_{deposit}(nm^3)$, some $R(nms^{-1})$, and the deposit height $h(nm)$. The measurements of these parameters can be explained with the following relations:

$$V_{deposit} = R t_{dwell} A_{deposit}, \tag{3.7}$$

$$h = R t_{dwell}, \tag{3.8}$$

$$I = J A_{beam}, \tag{3.9}$$

$$Q = I t_{beam}, \tag{3.10}$$

with $t_{dwell}(s)$ the dwell time, $A_{deposit}(cm^2)$ is the area of the e-beam.

All these ways of representing the data are correct, however, they complicate one-to-one comparison of different data sets. In addition, different electron-optical systems alter the beam diameter when the current I, is adjusted. A change in d_{beam} can affect the growth rate because $d_{deposit}$ changes as correspondingly to the diameter. When $V_{deposit}$ is held constant and $d_{deposit}$ increases, R decreases. However, quite often in the research literature, $d_{deposit}$ or d_{beam} are not measured or reported, making it difficult to accurately interpret R or h. To circumvent this issue in cases where only I is reported, we focus on measurements of $V_{deposit}$ as a function of I. This

complication does not arise for measurements where h is reported as a function of J, as both parameters are normalized per area.

Notably, the two different regimes can have a significant impact on the growth rate and deposit height. If we observe the regimes in more detail, we note that for low current densities, $\frac{gF}{N_0} \propto J$, making h linearly dependent on J. At higher current densities, $\frac{gF}{N_0}$ saturates and becomes independent of J. If we substitute $V_{deposit}$ with h, we observe similar behavior, unless h is scaled by $d_{deposit}$.

On the other hand, we can write h as a function of I, where this can be done in two ways. If we vary J (or I), and keep t_{dwell} constant, or we vary t_{dwell} and keep I constant (from eq.3.9). In the first approach, the behavior is the same as explained for the case where we increase the current density and measure h. In the second approach, the electron-limited and the precursor-limited regimes are distinguished by their slope [33].

Another way to represent the deposit growth behavior is by plotting h as a function of t_{dwell} for a constant I. This plot essentially displays the same data as for the second approach, where we vary t_{dwell} and keep I constant and both can be derived from the same experiment. The key difference is that the time scale is explicity shown. Similarly to the plot where h is varied against Q, the two regimes are not easily distinguishable, because they are again characterized only by different slopes [33].

Measuring the amount of material deposited under various growth conditions enables the determination of growth efficiency, which can be defined as the increase in h per primary electron (nm/electron). Based on the definitions of the two regimes, it is evident that growth efficiency is highest in the electron-limited regime and lowest in the precursor-limited regime.

3.1.5 Temperature dependence

The simplifications of the theoretical model are no longer applicable when desorption effects cannot be ignored. This situation arises, for example, when temperature variations are used to study their impact on the growth rate, deposit composition, or conductivity, or when the temperature is not constant during the deposition process. In such cases, temperature affects the residence time of molecules on the substrate. The dependence of the temperature to the residence time of the molecule can be expressed by:

$$\tau = \frac{1}{\vartheta} exp\left(\frac{E_{des}}{kT}\right), \tag{3.11}$$

where ϑ is the vibrational frequency of an adsorbed molecule (s^{-1}), E_{des} is the desorption energy (J), and k is the Boltzmann constant ($m^2 kg s^{-2} K^{-1}$), and T is the temperature (K).

Quantifying the impact of temperature on the growth rate is not straightforward. While it is still possible to encounter scenarios where growth is either electron-limited or precursor-limited, the conditions that lead to these regimes become more difficult to predict [33].

3.1.6 Substrate heating

Substrate heating is one common way to improve the conductivity of the deposit. If the substrate temperature is in the order of the precursor thermal decomposition temperature, it can lead to thermally-induced dissociation simultaneously with the electron-induced dissociation. However, the effect of heating can be a lower vertical growth rate, caused by the shorter residence times of the adsorbed precursor molecules. On the other hand, changes in the lateral growth will occur only if the temperature increase has caused a change in the growth regime [33].

An interesting project on 3D nanopillars has shown that depositions at cryogenic temperatures result in increased growth rates. In this study, a Peltier cooler was mounted on the stage, and growth rates were measured across different primary voltages [41, 42, 43].

3.1.7 Post-growth purification methods

One major drawback of the FEBID process is the high amount of carbon impurities that originate from incomplete dissociated precursor molecules or non-volatile fragments [44]. As the share of carbon in the overall structure content can significantly change the nature of the material, and thereby impact the intended functionality, a number of post-growth purification methods have been explored [45].

Annealing under UHV conditions at temperature of 600 °C is one of the common methods that allows purifying the material [46]. The carbon atoms inside the structure graphitize and the conductivity of the metallic element can increase. It is to be noted that not every annealing process will result in an improvement of the conductivity. In some cases, the carbon matrix can oxidize and dissappear, leaving the oxidized metal grains. A common situation is also the diffusion of substrate material into the deposit, and the deformation of the structure [17, 45].

Another method is postdeposition irradiation, that is, exposure of the deposit with a high current after the precursor supply has stopped. One of the possible effects of irradiation is graphitization of carbon deposits, and it can change the morphology of the sample from smooth to rough through induced heating. As a result, deposit conductivity increases, and the shape of the deposit can be smoothened [33].

3.2 Scanning NV magnetometry

Scanning nitrogen-vacancy magnetometry (SNVM) is a technique that uses properties of an NV center to measure magnetic fields with remarkable sensitivity [47, 48, 49]. A nitrogen-vacancy (NV) center is a type of point defect in a diamond lattice, where two neighboring carbon atoms are replaced by a nitrogen atom and a vacancy, respectively. This defect forms four covalent bonds with the neighboring carbon atoms, thereby leaving one electron from the nitrogen atom unpaired. This configuration results in a system of spin 1/2, also known as NV^0. The NV^0 configuration changes the energy distribution within the diamond bandstructure, allowing the NV center to capture an additional electron from the conduction band (CB) [50]. This forms a negatively charged NV^- complex, that is the essence of diverse capabilities of SNVM [48, 51].

3.2.1 Electronic and optical properties of the NV center

Inside the diamond bandgap 5.5 eV wide, a ground state $|g\rangle$, a shelving state $|s\rangle$, and an excited state $|e\rangle$ are settled. When there is no external field applied, the ground state $|g\rangle$ splits into $|m_s = 0\rangle$ and $|m_s = \pm 1\rangle$. Because the atoms are tightly confined in a non-cubic lattice, there is spin-spin interaction between the electron and the NV center, which is evident as the separation between these two ground states, also known as zero-field-splitting (ZFS), $D_G = 2.87\,\text{GHz}$. The excited state splits into two distinct states due to spin-orbit coupling, with a separation denoted as D_E. The shelving state $|s\rangle$ arises from the intrinsic electronic configuration of the NV center [51, 48].

When the NV center is illuminated by a green laser ($\lambda = 515\,\text{nm}$), electrons decay via two spin-conserving pathways, and the emitted fluorescent photons from this decay are collected by an APD camera (see Section 3.3.2). Each NV spin state in the orbital ground state can optically transition to the excited state. This direct optical excitation preserves the spin during the transitions. Additionally, electrons in the excited state with $m_s = \pm 1$ have a probability of 50% under typical conditions of decaying non-radiatively via the shelving state $|s\rangle$, eventually ending up in the orbital ground state $m_s = 0$.

The combination of these mechanisms means that the spin state can be continuously initialized by optically pumping the NV center into the orbital ground state. This process typically lasts a few microseconds and results in 95% fidelity in transferring the spin population to the ground state. Secondly, one can also read-out the NV spin-state by monitoring the fluorescence rate. If initial state was $m_s = \pm 1$, the NV

center will decay into the singlet state and appear "dark". If the initial state was $m_s = 0$, the NV will continuously emit photons, which will be recorded as "bright". Additionally, the spin-state in the ground state can be manipulated using a microwave signal resonant with the $|0\rangle \leftrightarrow |\pm 1\rangle$ transition [51].

3.2.2 Continuous Wave (CW) - Optically detected magnetic resonance (ODMR)

In the most basic picture, we can observe the optically detected Electron Spin Resonance (ESR) by probing the energy levels of the diamond with a microwave radiation source (e.g. copper antenna). While sweeping the frequencies corresponding to the diamond bandgap, we collect the fluorescence spectrum. This optically detected magnetic resonance spectrum consists of regions where the microwave frequency coincides to energy level NV spin being in the orbital ground state ($m_s = 0$), and the energy levels where the NV spin has transitioned into the excited state ($m_s = \pm 1$). In this case, when we continuously excite the population optically, the outcome of the transition process between the energy levels depends on both the optical laser power and the microwave radiation power. The resonance peak will split into two peaks shifted by $\Delta\vartheta$ in the presence of an external magnetic field. The smallest magnetic field detectable is limited by the shot noise in the setup:

$$\eta_{cw} = \frac{4}{3\sqrt{3}} \frac{h}{g_e \mu_B} \frac{\Delta\vartheta}{C_{cw}\sqrt{R}} \tag{3.12}$$

From equation 3.12, the prefactor comes from choosing the steepest point on the Lorentzian resonance fitting curve, h is the Planck's constant, g_e is the electron gyromagnetic ratio, and μ_B is the Boltzmann constant, $\Delta\vartheta$ is the linewidth, C_{cw} is the contrast, and R is the photon detection rate. For shot noise, it is valid that $R = \frac{N_{ph}}{t}$, where N_{ph} is the number of photons, and t is the time interval over which the photons are measured. The amount of shot noise in the setup depends on the environment and the current conditions during the measurement. We also observe that the integration time has a significant impact on the sensitivity, thereby enabling more sensitive measurements for longer integration times. Of course, this is practically limited by the time available for one measurement run. Further, the linewidth $\Delta\vartheta$ is inversely proportional to the dephasing time of the NV center T_2^*. Typically, this time can be anywhere in the range 1 µs to 50 µs. It is dependent on the specific type of diamond family, and it can be directly deduced from pre-characterizing the diamond tip.

This technique is frequently used in investigation of static magnetic fields of samples

(for frequencies below 10 kHz), showing its best advantage when measuring stray fields in the range of $1\,\mu\text{T} \leq |\mathbf{B}| \leq 5\,\text{mT}$.[51, 48]

3.2.3 Pulsed-ODMR

The pulsed-ODMR technique is a commonly used DC method that allows measurements constrained by the T_2^* of the NV center. In a typical pulsed-ODMR sequence, the NV^- spin state is first optically initialized to $m_s = 0$ state. After the initialization, the laser is turned off, a microwave pulse of duration τ_π is applied, where $\tau_\pi = \tau$ represents the time window set for the measurement. After the microwave pulse, the laser is turned back on, and the spin population is optically read out. Any change in the magnetic field will shift the spin resonance relative to the microwave frequency, leading to an incomplete π pulse and a change in the population transferred to the $m_S = \pm 1$ state before optical readout.

In this scheme, the average number of collected photons is reduced by the readout duty cycle, given by $t_R/(t_I + T_2^* + t_R)$. Here t_R is the readout time, and t_I is the initialization time. If we define $N_{ph} = Rt_R$ as the number of photons collected per optical readout cycle (as defined in Section 3.2.2) and after replacing C_{cw} with the pulsed ODMR contract C_{pulsed}, the pulsed ODMR sensitivity yields:

$$\eta_{pulsed} \approx \frac{8}{3\sqrt{3}} \frac{\hbar}{g_e \mu_B C_{pulsed} \sqrt{N_{ph}}} \frac{\sqrt{t_I + T_2^* + t_R}}{T_2^*} \tag{3.13}$$

where $\hbar$ is the reduced Planck's constant. The pulsed-ODMR technique, therefore, has a higher sensitivity compared to the CW-technique, and it is therefore used for measuring samples that have a very small magnetic field signal, as well as for studying the dynamics of the system, such as spin relaxation (T_1) or coherence time (T_2^*). This type of time-resolved data can be particularly useful when studying the interaction of the system with its environment as will be shown separately in Section 3.2.6 and 3.2.7. The pulsed-ODMR technique, therefore, offers higher sensitivity compared to the CW technique and is particularly useful for measuring samples with very weak magnetic field signals [48].

3.2.4 Measuring magnetic fields with the NV center

The susceptibility of the NV center's ground state $|g\rangle$ to a wide range of external parameters, including magnetic and electric fields, pressure, and temperature, enhances its applicability in multiple sensing domains. In other research papers, many

interesting details about its versatility can be discovered [52, 53, 54]; however, for the purpose of this work, we will concentrate solely on the impact of an external magnetic field.

The NV center interacts with the magnetic field, which is described by the following Hamiltonian:

$$\mathbf{H}_{\text{int}}/h = \frac{g\mu_B}{h}(BS) = \gamma_{NV}\mathbf{B}\cdot\mathbf{S}^{\dagger} \tag{3.14}$$

where $g_e = 2.003$ is the NV electronic Landé factor, μ_B is the Bohr magneton, h is Planck's constant, $\mathbf{S}^{\dagger} = (S_x, S_y, S_z)$ is the dimensionless electronic spin-1 operator, and $\gamma_{NV} \approx 27\,\text{MHz/mT}$ is the gyromagnetic ratio of the NV center. Here, z corresponds to the quantization axis. Applying a finite static field $\mathbf{B}$ results in the splitting of the energy levels $|+1\rangle$ and $|-1\rangle$, which is known as the Zeeman effect. In the Zeeman splitting we observe lifting of the degeneracy of the $|+1\rangle$ and $|-1\rangle$ spin states and an increase in splitting $\Delta\vartheta$ between the resonance frequencies as the external field $\mathbf{B}$ increases.

From equation 3.14, we can derive the equation that we will employ for further quantitative analysis of the amplitude of the magnetic fields:

$$\Delta\vartheta = \frac{2g_e\mu_B}{h}B_z = 2\gamma_{NV}B_z \tag{3.15}$$

In some cases, the analysis becomes more complex; for these specific situations, we refer to the literature [51, 48].

3.2.5 Imaging modalities

For the purpose of this work, we are interested to acquire quantitative and qualitative information about the magnetic field, the topography and the magnetic noise of the samples we are investigating. The commercial system we use has implemented features that allow us to perform a scan and observe directly the images which contain the information of interest. From now on, we are always referring to the points of information to have a spatial size of pixel by pixel, where we define the pixel size by selecting the size of the image and the number of points. Working with imaging modalities that have been previously implemented requires knowledge of the user about the capabilities of each modality, the sample being measured, and the type of data which is of interest. Within this subsection, we will provide a brief introduction of all the modalities which have been used in this study for acquiring magnetic field

and topography data. In Section 3.2.6 we will describe the T1 relaxometry method, used to acquire the information about the magnetic noise on the sample.

Quenching mode The quenching mode is based on the fundamental contrasting mechanism of NV magnetometry. The working principle is scanning with the NV tip over the sample while continuously exciting the NV center with a green laser, simultaneously followed by the acquisition of the fluorescence decays (red light) via the photodiode camera. The resulting number of the fluorescent photons is determined by the local magnetic structure of the sample. The local magnetic field is defined by its magnitude and direction, both of which can vary based on the magnetic field sources present in the sample. The final image answers the question: *how does the magnetic field vary across the structure of the sample when projected to the NV quantization axis?* We can choose the tip direction, such that this information is even more pronounced in the final image. However, for this purpose, one must know the expected direction of the magnetic field of the sample, and choose a tip which aligns with that direction. More commonly, we are looking into a sample with unknown stray magnetic field. In this case, we can conclude about the direction of the magnetic field based on the final image and the tip we used for the scanning. In the regions where the fluorescence is very low (dark), we lose the information about the strength of the field but we know the magnetic field direction is perpendicular to the NV quantization axis. In the region where the fluorescence is very high (bright), we can obtain more detailed overview of the magnitude of the magnetic field by using some of the following methods.

Full-B To answer a more frequent question: *what is the magnitude of the magnetic field at a distance $z = d_{NV}$ above a given point $P = (x_p, y_p)$ of the sample?*, we adopt the Full-B method. For each pixel, a full ODMR spectrum is recorded, and the value of the resonance frequency is automatically extracted. The resulting image contains data showing the magnetic field value calculated via equation 3.14 for a spatial map with a defined number of pixels N_{points}. To perform the calculation, the ODMR spectrum is fitted with the Lorentzian. It is worth noting that the Lorentzian fitting might contain "meaningless" data points in some cases. If the resonance peak exits the frequency window it will give an unfeasible value. This effect is visible in the final images as a spurious point, which is a clear outlier in the data. This measurement method typically requires a couple of hours, and for larger pixel maps, a longer overnight scan.

Iso-B The iso-B (or iso-field) method is a highly efficient technique for measuring small variations in the magnetic field (ΔB) around a known, stable bias field (B_0) using

the NV center, thus optimizing measurement time. The method starts by measuring the ODMR resonance curve (fluorescence intensity I versus microwave frequency ν_{MW}) to determine the optimal operating point. For measurement, the microwave frequency is set to a fixed value ν_{MW} that corresponds to the steepest slope of the ODMR curve. The sensor's sensitivity is maximized at this point, where a small change in the magnetic field (ΔB) causes a corresponding shift in the NV's electron spin resonance frequency ($\Delta\nu_{\mathrm{res}}$). This frequency shift is converted directly into a large, highly sensitive, and measurable change in the fluorescence intensity (ΔI). By monitoring ΔI, the technique allows one to rapidly and sensitively track ΔB without needing to continuously sweep the microwave frequency, thereby maximizing the magnetic field sensitivity of the sensor.

Dual Iso-B

The Dual Iso-T1 technique is a differential sensing method based on the NV center's spin relaxation time, T_1. This technique exploits the fact that the T_1 time exhibits sharp minima when the external magnetic field B aligns the NV spin level splittings with the Larmor frequency of surrounding spin baths.

To measure small variations in the local magnetic field $\mathbf{B}_L$ of the sample, we select two magnetic field values, $\mathbf{B}_1$ and $\mathbf{B}_2$, which are known as iso-sensitive points. These points are chosen symmetrically around the T_1 minimum ($\mathbf{B}_{\mathrm{min}}$) such that the unperturbed T_1 times are initially equal ($\mathrm{T}_1(\mathbf{B}_1) = \mathrm{T}_1(\mathbf{B}_2)$).

The technique measures the NV fluorescence (**PL**) after a fixed T_1 evolution time τ at both $\mathbf{B}_1$ and $\mathbf{B}_2$, and then calculates the difference $\Delta PL = PL_1 - PL_2$. The primary benefit is that this differential measurement cancels common-mode noise and instrumental drift (e.g., laser power fluctuations) which affect both fields equally. This significantly enhances the signal-to-noise ratio and provides a highly sensitive, linear output for small changes in the local field ΔB_L

3.2.6 T_1 relaxometry

The principle of the measurement is illustrated on Fig.3.2. The NV center is modelled as a closed two-level system with its corresponding ground states with spin levels m_s=0 and m_s=±1. By continuously shining the NV center with a laser, we initialize the spin population, and after giving the system time to evolve, we collect the photoluminescence. There are two competing mechanisms that influence the distribution of the spin population: the spin relaxation rate $\Gamma_1 = \frac{1}{2T_1}$ and optically-induced spin

polarization in the m_s=0 level where the photoluminescence depends on the excitation power, and the related rate is Γ_p.

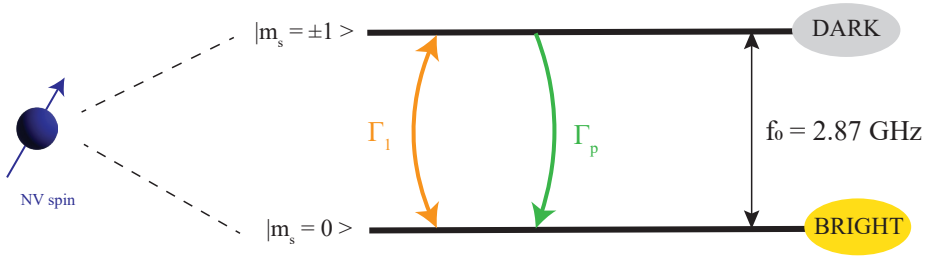

FIGURE 3.2 — Principle of T_1 relaxometry of an NV center in diamond.
T_1 relaxometry is a technique used to measure the longitudinal relaxation time (T_1) of spins in a magnetic field. This method provides insight into the dynamics of spin-lattice interactions, allowing for the characterization of material properties. The process involves applying a radiofrequency (RF) pulse to disturb the equilibrium state of the spins, followed by monitoring their return to equilibrium over time. The resulting T_1 values can indicate the presence of specific environments and interactions within the sample. [55, 56]

Depending on the excitation power, the photoluminescence evolves differently with the evolution time. We here consider the case where $\Gamma_1 \ll \Gamma_p$, which leads to efficient initialization of the spin population in the m_s=0 and leads to a high photoluminescence signal. In case the magnetic noise increases the spin relaxation rate, such that $\Gamma_1 \sim \Gamma_p$, the NV spin polarization mechanism is disturbed, resulting in a reduced photoluminescence intensity. Thus, one can directly measure the impact of the magnetic noise by measuring the photoluminescence [55].

3.2.7 T_1 and Iso-T_1 measurement techniques

In the measurement scheme as depicted in Fig.3.3, we follow the flow of the experiment with time t. The measurement starts by sending a pulse of a certain duration we call t_{laser}, after we don't send any pulses for a time τ. This time is often referred to as the evolution time because it is the time duration for which the system is no longer perturbed by our measurement but only by the conditions in its environment, from a starting condition we set. After this time, we measure the photoluminescence PL_1 and PL_2, in two time windows, at the beginning and at the end of the pulse. The resulting normalized photoluminescence is given by the ratio P_1/P_2. We repeat the measurement sequence for increasing evolution times τ_1, τ_2,...τ_N and we collect the normalized PL for each τ_N (N=0,1,2...). These points make an exponential curve which can be fitted with a function $e^{-\frac{t}{T_1}}$. The time T_1 from the denominator of this function is called the normalized T_1 time. The same reasoning applied to a case when

we measure the photoluminescence only once at the beginning of the pulse. In this case it is simply referred to as T_1 [51].

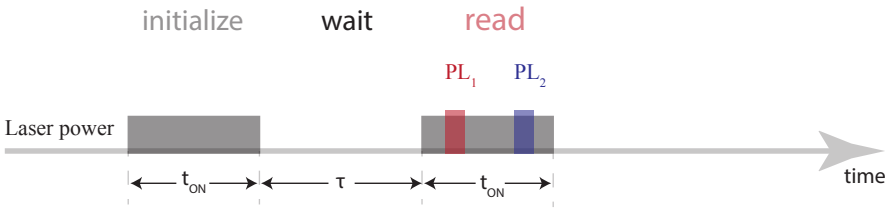

(a)

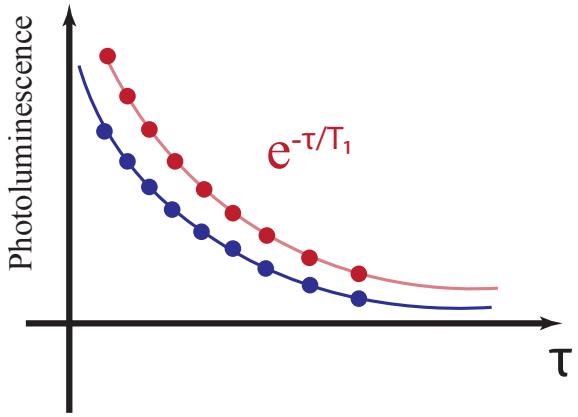

(b)

FIGURE 3.3 — Measurement schemes for T_1 relaxation.
(a) Experimental flow of the T_1 relaxation measurement, starting with a laser pulse of duration t_{ON}, followed by an evolution time τ. After the evolution period, photoluminescence signals PL_1 in red and PL_2 in blue are recorded, leading to the normalized ratio P_1/P_2. This sequence is repeated for various τ, resulting in an exponential decay fitted to $e^{-\frac{t}{T_1}}$ to determine the normalized T_1 time. (b) Iso-T_1 measurement scheme, where the time between the laser pulse and photoluminescence acquisition is fixed, allowing for consistent evolution time across the entire scan. The normalized ratio $\frac{PL_1}{PL_2}$ is calculated for each point, providing insights into the impact of perturbation under uniform conditions.

Similarly, we can fix the time between the laser pulse and the acquisition of the photoluminescence. We then collect the photoluminescence at the beginning of the acquisition pulse and at the end, and for each point of the scan, we measure $\frac{PL_1}{PL_2}$. The advantage of this measurement technique is that we let the system evolve for the same time for each point, and we can observe the impact of the perturbation on the whole area in consistent conditions. This measurements is referred to as iso-T_1.

3.3 Experimental setups

For the fabrication of Co nanomagnets in this work, we utilized the FEI Helios Nanolab 650 [32], an experimental setup located at the Swiss Nanoscience Institute in Basel. A detailed description of the system components can be found in Section 3.3.1.

In Section 3.3.2, we describe a commercial quantum microscope used for the SNVM magnetic imaging studies presented in this thesis. The measurements reported in this work were conducted at the Quantum Sensing Laboratory at the University of Basel and at the facilities of the spin-off company Qnami AG in Muttenz.

3.3.1 FEI Helios Nanolab 650

The FEI Helios Nanolab 650 is an advanced system capable of both focused-electron-beam and focused-ion-beam deposition. It includes an electron column, an ion column, and a gas injection system equipped with platinum (Pt), cobalt (Co), carbon (C), tungsten (W) and SCE (selective chemical etching). The system also includes a nano-manipulator, an Elstar in-lens secondary electron (TLD-SE) detector, an Elstar in-lens backscatter electron (TLD-BSE) detector, and an Everhart–Thornley SE detector (ETD).

Before starting deposition, we check the temperature of the cooling water that dissipates heat from the electron column and the system's electronics. If the temperature is below 20 °C, we proceed safely.

For Co, Pt and Au depositions, we place the sample in the chamber and pump for at least 12 h, for achieving the best possible vacuum so that the concentration of the intended elements is higher. When mounting the sample, it is crucial to ensure proper grounding. This can be achieved using a sample holder with a top screw or by applying aluminum tape around the sample's edge to provide additional discharge paths for electrons. For nA currents, a grounded sample holder is preferred, while for pA currents, a carbon tape holder is more suitable.

After mounting the sample, we begin venting the system by pressing the "V" button on the side of the chamber. The sample is inserted using the quick loader, which minimizes pressure fluctuations inside the deposition chamber when changing the samples. This method is particularly advantageous when depositing on multiple substrates in one day. For Co, using the quick loader yields similar structural properties, even if the system is not pumped overnight for subsequent samples. Once the sample holder is properly positioned on the mechanical rod, we start pumping the system by

pressing the "P" button on the side of the chamber. The system will reach a pressure below 2.5×10^{-6} mbar within a few minutes, and the pressure can be monitored from the software window.

Next, we start setting the electron column. After positioning the stage at the center, we select the e-beam quadrant in the software and turn on the beam. We adjust the beam shift and set the desired voltage and beam current values. We check if the ETD detector is selected, then focus on the highest area of the sample using a magnification below 5000X. When zooming in on any region of the sample, the microscope's Z coordinate will change correspondingly. Finally, we link this height to the free working distance (FWD).

We continue by aligning the electron column. To properly align the electron column, we first locate a small particle on the sample surface and focus on it using a magnification higher than 20000X. The software includes a built-in reduced window option, which is useful for quickly focusing and identifying very small particles on the surface. We then adjust the stigmation in the X and Y directions with very controlled turns of the knob, alternating between them to maintain a good balance based on the changes we observe in the image. After a few adjustments, it becomes clear how to further fine-tune the settings to achieve the best resolution. We repeat the same procedure with the fine focus. Next, we adjust the Source Tilt, the Crossover, and Lens Alignment. After making these adjustments, we focus once more on the tiny particles using the fine focus.

Before starting the patterning process, we set the eucentric height. First, we adjust the stage to a working distance of Z = 4 mm. We then focus and relink the stage's Z parameter to the free working distance (FWD). Next, we change the beam current to 13 pA, and align a feature on the sample to the center cross on the screen. We tilt the column incrementally to 5°, 10°, 15°, 35°, 52°. After reaching 15°, we tilt the column back to zero and check if the longitudinal shift of the beam is minimized. If not, we repeat the tilting process.

We then proceed with patterning the structure. We select the pattern type and dimensions, and adjust other parameters such as dwell time, dose, etc. to each shape. The software allows for depositing sequences of shapes with specific parameters. Additionally, any geometry shape can be imported via a bitmap, which the program can use for deposition.

After setting the geometry and its parameters, we warm up up the GIS cell and open the gas flow. As the gas is released, we observe the system's pressure increasing. This step must be performed carefully, as the pressure must be consistently monitored

and should never exceed the system's upper limit of 10×10^{-5} mbar (set value in this specific system). After some time, the pressure will stabilize as the gas flow continues. Once this happens, we fully open the gas cell and allow the pressure to settle. This point is noted as our pressure flux for depositing the structure. We then insert the GIS nozzle and begin the patterning process once the cell is fully in. After the deposition is complete, we retract the GIS nozzle and turn off the gas flow in the GIS cell. We take a snapshot of the deposit, ensuring we minimize the time the deposit is exposed to the SEM to reduce carbon incorporation into the sample. Once the patterning process is finished, we manually reduce the Z distance and start pumping the system again by pressing "Pump" on the software interface. We remove the sample stage by using the rod after hearing a click sound in the chamber. Once the sample is securely in the quick loader, we press "V" button to vent and remove the sample with the holder completely from the machine.

3.3.2 Commercial ProteusQ system for SNVM

The system is equipped with an atomic force microscope that has its own software and can be independently run for quick AFM inspections, particularly useful in the starting phase of measuring a new sample. The scanning magnetometry measurements are enabled with the laser and the confocal optics which is built in the microscope, antenna, and a separate microwave delivery unit. The measurement is controlled through a special interface (LabQ) which connects the microwave delivery unit (MicrowaveQ) and the microscope. The laser and the microwave power are set through the interface and effectively changed by the microwave unit. Once the measurement is done, the final image is displayed in the interface and there are options to filter the image, choose specific points on the image to inquire the ODMR spectrum, etc. One can change the scan directions through the interface, which interacts back to the AFM platform that adopts the requests made by the user.

Initially, we check the parameters of the tuning fork to assure the AFM scan is of high quality. The initialization of the tunning fork is done through the AFM interface. At the end of the calibration measurement, a Q factor in the range 1000-2000 is expected to ensure safe operation, where we anticipate high AFM quality.

The diamond tip containing the NV center is mounted on the Akiyama probe, with the diamond sensor positioned at the very tip of the cantilever. The sensor is optically aligned with the objective, and then the antenna is positioned close to the sensor for optimal microwave power delivery. The sample scanner, situated directly below the

sample holder, allows for manual adjustment of the sample's position in the x, y, and z directions via a console window accessible through the AFM interface.

The sample is illuminated by white light coming from the confocal microscope module, using a high numerical aperture objective lens (0.7). The fiber-coupled single-photon counting module collects the emitted signal from the diamond sensor. The data is then processed by the Qudi software and displayed in the LabQ interface window.

The scanning magnetometry measurements are controlled through a special interface (LabQ) that has built-in measurement procedures for different target parameters. Full-ODMR, fluorescence, iso-B, height measurement, frequency shift measurements, etc. can be run, where some of these measurements run in parallel, for instance, Full-ODMR and fluorescence, height and frequency shift measurements can be obtained in separate graphs for a simple and quick data analysis of relevant measurement parameters.

After locating the area of interest on the sample using AFM, we proceed with performing ODMR in real-time. First, we select the laser and microwave power to maximize the sensitivity of our measurement, focusing on optimizing parameters for the specific sample being measured. By selecting two or more points on the scan where we expect to obtain the highest signal, we can estimate the frequency window of our measurement based on the observed frequency shifts.

For instance, in samples where the magnetic stray field changes are small, such as on the order of μT, we benefit from a very sharp resonance peak. This peak can be enhanced by increasing the microwave power, though it will ultimately be limited by the specific tip we are using (i.e., $\Delta\vartheta \sim T_2^*$). Further improvements are possible by employing pulsed-ODMR or tritone excitation measurement schemes.

If the shifts are in the order of 100 µT to a few mT, a broader resonance peak might be more satisfactory. Additionally, the magnetic field direction relative to the NV quantization axis also affects the amount of fluorescence signal we collect. If we observe a significant reduction in contrast compared to measurements in air, it may indicate the presence of strong perpendicular components on the sample. In this case, we might consider increasing the laser power to maximize the detected fluorescence signal, though this will be limited by laser saturation. Alternatively, one could consider magnetizing the sample with the external magnet and choosing a tip with a quantization axis parallel to the magnetization direction.

For measurements requiring sample magnetization and for acquiring hysteresis data of the magnetic material under a varying external field, we need to install the external magnet in the ProteusQ system. The package set with the external magnet includes an external Hall sensor used for magnetic field calibration. It is positioned below the sample, very close to the ends of the leads. The external magnet and Hall sensor are connected via a USB cable to the controller unit, which is then connected to the PC. We set the desired value of the magnetic field on the surface of our sample using the AFM software. This value is sent to the magnet controller, which rotates the magnet until the Hall sensor senses a value proportional via a calibration factor. The field can be applied in-plane and out-of-plane, with a limit of 500 mT for the in-plane field and 150 mT for the vertical field. It is necessary to align the tip and bias field before starting the measurements, noting that when the magnetic field component parallel to the NV axis is 50 mT or 100 mT, measurements are not possible due to energy anti-crossings. Beyond 150 mT, all measurements become more robust.

4 Focused-electron-beam-induced deposition of cobalt magnets on different substrates

Part of the results from this chapter are published in: Scanning NV magnetometry of focused-electron-beam-deposited cobalt nanomagnets, ACS Applied Nano Materials 7, 3854-3860 (2024), the rest is described in: Measuring high field gradients of cobalt nanomagnets in a spin-mechanical setup, arXiv (2025)

Fabricating well-defined geometries on very thin silicon nitride membranes using Focused-Electron-Beam-Induced Deposition presents a significant challenge [57, 58, 59]. This is primarily due to the high charging effects associated with depositing on insulating substrates and the complex growth mechanisms on such thin materials. While FEBID has proven effective for depositing cobalt on carbon-based thin membranes [26], achieving similar results on widely used, industrially compatible substrates like silicon nitride has not been extensively studied. Gaining control over FEBID on silicon nitride membranes would open the door to applications in common solid-state systems and high-Q resonators used in optomechanics.

In this chapter, we explore the challenges and solutions involved in fabricating cobalt nanowires on both silicon chips and cobalt hemispheres (dots) on thin silicon nitride membranes.

4.1 Focused-electron-beam-deposition on silicon chips

Within this work, we focused on the design of the part of the spin qubit device which will provide reliable magnetic gradients for efficient rotation of the spin qubits. For this purpose, we desire to fabricate cobalt nanomagnets. Cobalt is a ferromagnetic material, it has a high Curie temperature, it is highly durable and resistant to corrosion [60]. In addition, it is often used in industry and therefore, widely available [61, 62]. Typically, nanomagnets are patterned using a multi-step procedure, for instance involving resist-coating, electron-beam lithography, deposition of a thin film of a magnetic material such as cobalt, and lift-off. High-quality thin films of Co can be deposited in various ways, including ion beam sputtering, electron-beam evaporation [63], thermal evaporation[63, 64], electrolytic deposition [65], metal-organic chemical vapor deposition (MOCVD) [66], molecular beam epitaxy (MBE) [67], and pulsed laser deposition (PLD) [68]. Such a multi-step patterning procedure is prone to introducing misalignment of the lithography masks and incorporation of defects. Furthermore, such techniques are limited to fabrication of 2D patterns.

Here, we use FEBID to pattern Co nanomagnets. FEBID is an appealing technique for the fabrication of nanomagnets due to its single-step nature, and allows for the fabrication of 3D geometries [69, 70], opening up new ways of engineering magnetic gradients optimized for spin qubit control [29]. For example, such 3D patterning could be used to produce arrays of nanomagnets with identical 2D footprints, but differing in height profile. Such arrays would be of use in scaling up e.g. spin qubit devices in a modular approach, where variations in the nanomagnet height profile can be used to locally vary the spin qubit Zeeman energy and/or magnetic field gradients, allowing for individual qubit addressability as well as variations in driving and dephasing strengths across the arrays. Another potential advantage of FEBID to pattern nanomagnets lies in its direct-write nature. This allows for in-situ fine-tuning of the shape and magnetic properties, such as coercivity and magnetic anisotropy, of the deposits. Furthermore, FEBID does not generate impurities in the form of residual resist, although C and O are typically deposited along with Co. FEBID of Co has been demostrated as a reliable technique for growing magnetic nanostructures, reaching Co content of up to ~96 atomic percent of bulk values [69, 71]. FEBID also allows for patterning with lateral resolution in the nm range, approaching the intrinsic limit of the process imposed by the electron beam diameter. For Co nanostructures, lateral resolutions of below 30 nm have thus far been achieved [30].
To grow the nanomagnets, we used a commercial Thermo Fisher FEI Helios NanoLab 650 (see 3.3.1), equipped with a $Co_2(CO)_8$ gas injection system. We select the rectangular pattern before the deposition with X = 200 nm, Y = 14 µm, Z = 250 nm. To achieve high Co content and high lateral resolution, we used the following FEBID parameters: an acceleration voltage V_{acc} = 10 kV, a beam current I_{beam} = 3.2 nA, dwell time t_{dwell} = 1 µs, and a precursor flux corresponding to a vacuum chamber pressure $P_{flux} = 4 \times 10^{-6}$ mbar.

After the deposition (Fig.4.1(a)), we proceed and characterize the height of the nanomagnet using AFM, and the width and length with SEM. The geometry of the final structure as shown on 4.1(b) with dimensions: 230 nm width, Y = 14.4 µm length, and Z = 130 nm height. To facilitate a sample for further investigation using a transmission electron microscope and its capabilities for high resolution STEM in combination with energy dispersive x-ray spectroscopy (EDX) we utilized focused-beam-induced deposition. Before lamella preparation the sample was covered with a layer of Pt grown through FEBID and FIBID, to protect the cobalt deposits while milling the lamella. Thinning and polishing of the lamella was done with an ion acceleration voltage of 30 kV, and currents of 0.24 A and 83 pA respectively, resulting in a lamella thickness of ~ 65 nm. The reader might be interested in why we haven't

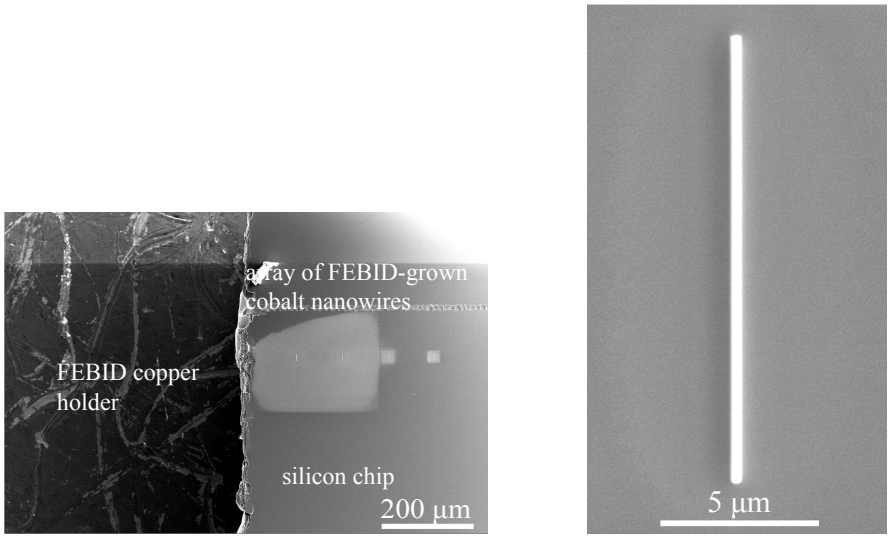

Figure 4.1 — Fabrication of Co nanowires with FEBID.
(a) FEBID deposition of an array of cobalt nanowires, with significant residual cobalt from initial depositions visible. (b) A single cobalt nanowire, perfectly shaped with pattern parameters: rectangular pattern dimensions of $X = 200\,\text{nm}$, $Y = 14\,\mu\text{m}$, and $Z = 250\,\text{nm}$, demonstrating the precision achievable with FEBID.

chosen to use Focused-Ion-Beam (FIB) milling for fabricating magnets, such as for shaping the deposit into a desirable geometry or removing the halo region from the intended deposit. The reason is that with the FIB we introduce an excess amount of Ga ions into the deposit and on the chip surface, which may increase the noise and change the magnetic properties of the magnet. Hence, we use it only for lamella preparation, however, further options can be considered when employing FEBID at cryogenic temperatures [72].

We further investigated the lateral resolution of cobalt nanowires as a function of acceleration voltage during the FEBID process. For this study, nanowires with identical geometries were deposited while varying the acceleration voltage (see Fig.4.2(a) and Fig.4.2(b)). Consistent with previous research [44], we observed an improvement in lateral resolution with increasing acceleration voltage, demonstrating that higher voltages increase the lateral resolution and minimize electron scattering, which contributes to sharper, more defined nanostructures. By fabricating circlular patterns with varying diameters on a silicon cantilever (see Fig.4.2(c)-(e)), we demonstrate a lateral resolution of below 50 nm. The deposition conditions were set at a chamber pressure of 3×10^{-6} mbar, beam current of 100 pA, and an acceleration voltage of 10 kV.

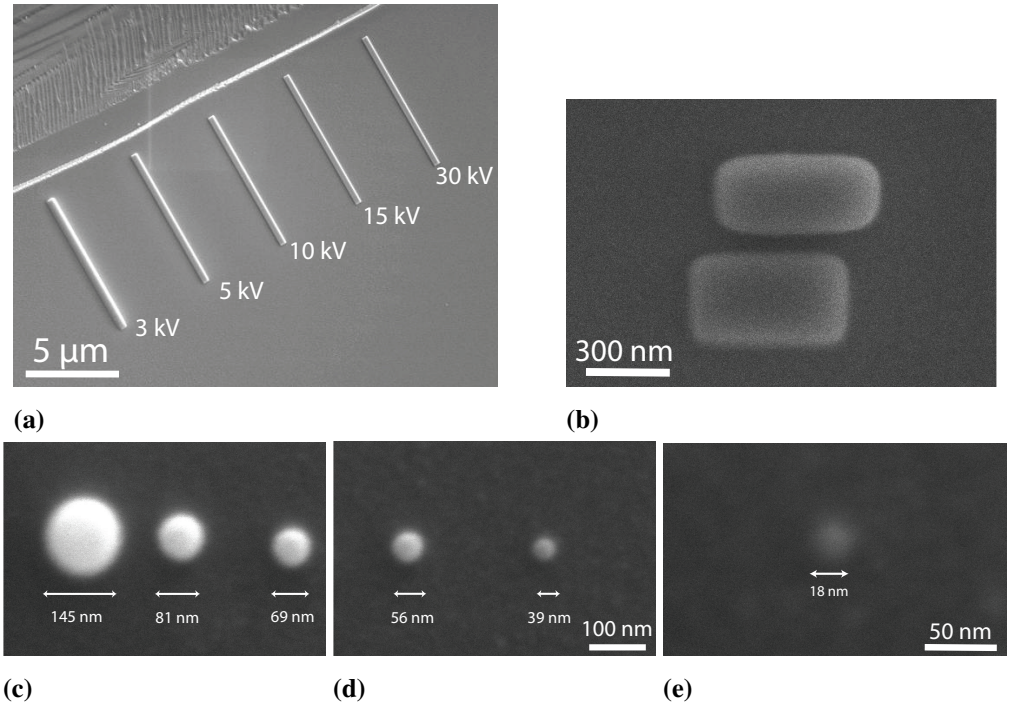

FIGURE 4.2 — FEBID resolution and shape tests.
(a) Nanowires with identical dimensions deposited under varying acceleration voltages (V_{acc}) show improved lateral resolution with increasing V_{acc}. (b) Rectangular shapes exhibit sharper edges at higher V_{acc}, with widths in the hundreds of nm. (c)-(e) Tests on circular shapes with diameters $d = [100, 80, 60, 40, 20, 10]$ nm demonstrate excess material due to electron scattering during deposition. The deposition conditions were set at a chamber pressure of 3×10^{-6} mbar, beam current of 100 pA, and an acceleration voltage of 10 kV.

4.2 Fabrication of 100 nm circular magnets on high-Q silicon nitride membrane

4.2.1 Motivation

Along with the implementation of quantum logic with spin based qubits, nanomagnets with precisely defined geometries are of interest in a variety of other applications, including magnetic resonance microscopy [73, 74], magnetic memories [75], nanomagnet logic [44], and, as mediating elements between spins and mechanical degrees of freedom [76, 77, 78, 79]. More recently, there has been a significant effort towards realizing nuclear MRI [80, 81]. Nuclear MRI is particularly fascinating because of its potential for non-invasive imaging with atomic-scale spatial resolution and the ability to probe nuclear spins in materials. However, despite its potential, achieving this capability remains a challenge, as it is still limited by the geometry of the setup, the sensitivity and the measurement protocols [82]. The *Quantum Optomechanics* group from the Niels Bohr Institute in Copenhagen [83] has demonstrated the ability to fabricate SiN phononic membranes with state-of-the-art quality factors, offering unique advantages for optomechanical experiments [84]. In this project, we successfully fabricated FEBID Co-nanomagnets on these phononic membranes, paving the way for coupling the membrane with the NV qubit in the next phase of the study.

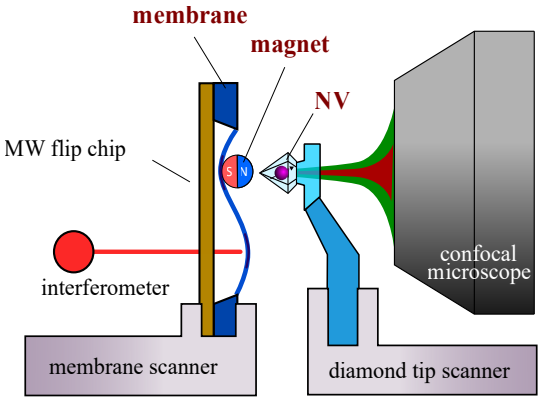

FIGURE 4.3 — Schematic of the experimental setup for demonstrating the coupling between the phononic membrane and the NV qubit.
The setup includes the FEBID-fabricated Co nanomagnet positioned on the SiN phononic membrane, with interferometer and MW flip chip used for controlling the NV qubit. The experimental design allows for real-time monitoring of the interaction between the mechanical motion of the membrane and the quantum states of the NV qubit, providing insights into their coupling dynamics.

We observe the experimental setup on Fig.4.3. It consists of a membrane 3-axis coarse and fine scanner, a diamond tip 3-axis scanner, confocal microscope with a

xy scanning mirror, diamond tip containing a NV center, SiN membrane with a Co nanomagnet glued to a MW flip chip, and an interferometer to detect the mechanical motion of the membrane. Active coupling is induced by driving either the NVs spin with according MW sequences or the membranes motion with a modulated auxiliary beam colinear with the interferometer. The confocal microscope is used to position the tip above the magnet. The flip chip on the back side contains a microwave antenna which delivers the microwave signal for the spin control.

In this section, we turn our attention to the mechanical components of the system that underpin high sensitivity in spin detection: high-quality (high-Q) phononic membranes. The fabrication process of the nanomagnets involved the utilization of various generations of silicon nitride (SiN) membranes. Notably, we employed the *Dahlia* and *Lotus* membranes. These high-Q phononic membranes have been demonstrated to enhance the sensitivity of spin detection by minimizing thermal noise and maximizing mechanical quality factors, crucial for advanced quantum applications [84, 85]. The selection of these specific membrane types is integral to achieving the performance required for effective spin manipulation and measurement.

The membranes are soft-clamped and incorporate a phononic crystal design, which enables the presence of localized bandgap modes. We characterize the membranes by their quality factor Q and the thermal force noise spectrum, described by the following equation:

$$S_{F_{th}}^2 = 4mw_m k_B \cdot \frac{T}{Q} \tag{4.1}$$

A typical value for the thermal force noise $S_{F_{th}}$ is approximately 280 $aN\sqrt{Hz}$ [86]. The resonance frequencies of the membranes are found to lie within the range of f_0 = 1 MHz to 1.4 MHz. These characteristics underscore the suitability of these membranes for applications in high-sensitivity spin detection and quantum mechanics experiments, as evidenced by previous studies [84, 85].

4.2.2 Deposition on phononic SiN membranes

As mentioned in the previous chapter, a wide variety of techniques are used for the development of high-quality magnetic films. With FEBID, we are able to grow Co nanomagnets on Si, and, as will be shown in the following, on SiN membranes. The substrate plays a role when choosing the fabrication technique for deposition of magnetic material, e.g. with e-beam evaporation the high beam voltage can destroy

thin substrates, and multi-step procedures in the clean room increases the chance to damage delicate properties of very thin silicon nitride membranes.

Silicon nitride (Si_3N_4) is an excellent insulating material characterized by high thermal stability and mechanical strength. It is often used in applications requiring electrical insulation, such as semiconductor devices, where it serves as a protective layer or a dielectric spacer. Its high resistance to electrical current makes it an effective insulator for diverse electronic and industrial applications. In the field of optomechanics, silicon nitride is often used for fabrication of high-Q resonators because of its low mechanical dissipation properties. It exhibits low intrinsic mechanical losses, which allows to maintain a high Q factor even at room temperature [87]. In addition, silicon nitride can be fabricated under high tensile stress, which further reduces bending and stretching of the membrane, and further reduces the energy losses during oscillations. Its high elastic modulus ensures the membranes are stiff, and more immune to external vibrations which decreases the noise influence from the environment during very precise optomechanics experiments. Its optical properties are transparency at specific wavelengths in visible and infrared bands, and low optical absorption, both relevant for optomechanics experiments where interaction of light and the membrane is involved.

The main challenge of using FEBID on insulators such as silicon nitride is in charge accumulation that occurs due to the insulating nature of the material. Secondly, this accumulated charge creates an electric field which can deflect the beam, causing instabilities in the beam precision and focus. This makes it difficult to precisely control the deposition process, which leads to poor resolution and deposition of distorted structures. The charge build-up can also alter the chemical reactions at the deposition site. This can influence the decomposition process of the precursor molecule used for the deposition, resulting in altered purity and composition of the deposited structure. Further, the local electric field of the accumulated charge can cause further complications and the beam can retract from the deposition point, causing complications when depositing structures on specific regions of the sample, which is often the case in most applications. To overcome these issues, various strategies can be employed, such as placing a conductive tape near the deposition area, or, if possible, fully coating the substrate with a conductive film, or even using ESEM (Environmental Scanning Electron Microscope) in humid environment, that allows improved surface conductivity. All of these solutions come with their own drawbacks and potential complexities. It is also beneficial to use low beam voltages, which decreases the amount of charge deposited on the substrate, however, it comes

with the trade-off in the lateral resolution of the deposited structure.

Next to the insulating properties of silicon nitride, the membrane is very thin - i.e. 50 nm. The thickness of the substrate is a parameter to consider when choosing the fabrication technique for the deposition of magnetic structures, since most common fabrication techniques work with very high acceleration voltages, e.g. e-beam evaporated cobalt films are deposited with 10 kV to 15 kV or 5 kV to 10 kV, depending on the system. Under such high beam voltage, the membrane is prone to break or lose its advantageous properties. Moreover, the multi-step process in the clean-room increases the chance for introducing impurities and lowering the quality factor of the membrane. On the other hand, FEBID allows deposition under lower acceleration voltages and can deposit structures locally on a specific position, without modifying significantly the rest of the sample area. Nevertheless, there are some points to consider when using FEBID on thin substrates. Thin substrates are more prone to substrate heating, due to the lower thermal mass and poorer thermal dissipation, making them more sensitive to local heating, which may cause deformations or even breakage of the substrate. The other potential issues are charge effects and electron backscattering. For the same reasons as in the insulating samples with thicker substrates, the thinner substrate of an insulating material has even lower conductivity, making it even more prone to charging. There is also a possibility of electron backscattering, if the electrons of the beam penetrate the substrate and reflect from the stage holder back to the membrane, thereby creating an unintended deposit. Possible way to overcome this issue, if the application permits, is to deposit a film of a highly conductive material on top of a thin substrate. As seen in previous work, FEBID deposition has been proven effective in deposition of nanodots on carbon substrates of only 4 nm thickness [26]. However, in the case of high-Q resonators for single-spin mechanics experiment, depositing an additional layer of conductive material would irreversibly change its optomechanical properties.

By performing simulations we've identified that the ideal magnetic geometry would be a disk with diameter in the order of 100 nm. Circular shape has shown optimum magnetic coupling and uniform magnetic field in the region of interest which is crucial for precise control of single-spin dynamics. The nanoscale size of the magnet ensures that the magnetic influence is localized, which is essential for isolating and manipulating single spins.

During initial tests with FEBID and by selecting the circular pattern of the raster beam, we have observed charging effects and beam deflection. The resulting magnetic deposit had a distorted shape and poor resolution. However, when using a rectangular

pattern of the raster beam, an interesting result occurred - exactly the desired circular shape of the magnet was formed.

In a circular pattern of the raster beam shown on Fig.4.4(b), the beam moves in concentric circles or spirals. Consequently, the heat distribution is more concentrated towards the center, where the beam spends more time, because of the shorter path length of the inner circles. This leads to a hotter central region, causing localised thermal effects such as diffusion and the change of material properties, while less heat is accumulated towards the outer edges.

In a rectangular pattern shown on Fig.4.4(a), the beam typically moves in straight horizontal or vertical lines, covering the area in a grid-like form. This can lead to a more uniform coverage across the scanned area, as each line receives a similar amount of beam exposure. On the other hand, the corners of the rectangular shape receive less beam interaction, that cause less consistent material distribution. Another difference is the precursor replenishment, which is more uniform in the rectangular pattern of the raster beam.

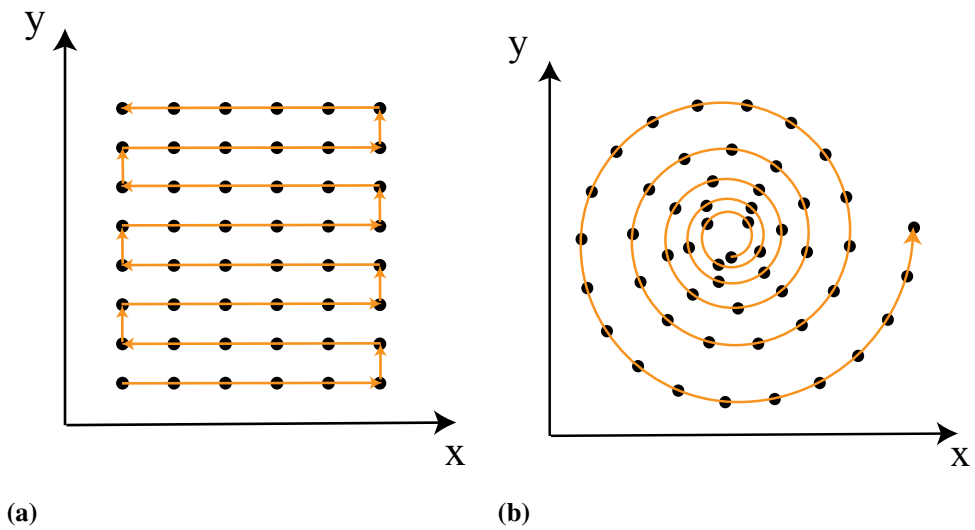

FIGURE 4.4 — Comparison of raster beam patterns used in FEBID on SiN phononic membranes.
(a) Rectangular pattern, allowing for uniform material deposition across the scanned area, but exhibiting reduced interaction at corners, leading to potential inconsistencies. (b) Circular pattern, resulting in a concentrated heat distribution towards the center, causing localized thermal effects and distortion in the magnetic deposit shape.

We successfully fabricated arrays of Co nanomagnets on silicon chips using a circular raster beam pattern (Fig. 4.5(a)), alongside a single Co nanomagnet created with a rectangular pattern on a 50 nm silicon nitride (SiN) phononic membrane (Fig.

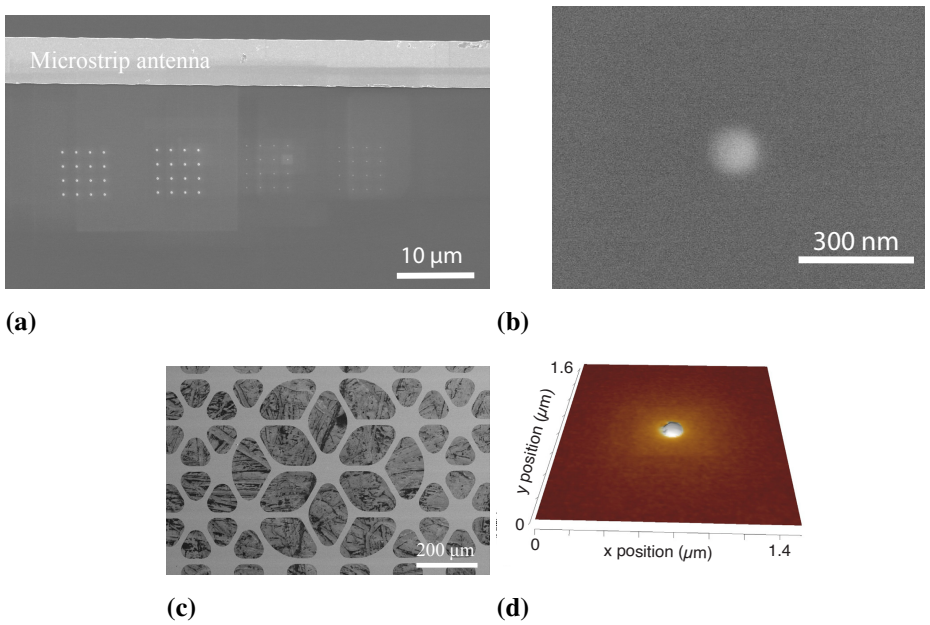

FIGURE 4.5 — Fabrication of FEBID dots for SiN high-Q membranes. (a) Arrays of Co dots on Si chip, (b) Co nanodot deposited on a high-Q SiN membrane, (c) SEM image of the phononic membrane in top-view (d) AFM image of a Co nanodot on SiN membrane, exposing the hemispherical shape height of the nanodot with measured height = 100 nm.

4.5(b)). The atomic force microscopy (AFM) analysis of the Co nanomagnet on the SiN membrane, illustrated in Fig. 4.5(d), revealed a measured height of 105 nm (Fig. 4.5(e)), which closely corresponds to the SEM - measured diameter of 110 nm. These results highlight the effectiveness of different raster patterns in controlling the shape and dimensions of nanomagnetic deposits.

4.3 Outlook

In this chapter, we have presented the successful fabrication of cobalt nanomagnets on both silicon chips and thin silicon nitride phononic membranes. We achieve a remarkable lateral resolution of down to 18 nm on silicon chips. Counterintuitively, our results demonstrate that utilizing a rectangular raster pattern, rather than a circular one, successfully enables the deposition of hemispherical nanomagnets on thin silicon nitride membranes, mitigating the charging issues that would otherwise prevent this deposition.

The successful fabrication of cobalt nanomagnets on silicon chips lays the groundwork for future advancements in developing magnets for spin qubit control, which are elaborated in Chapter 5.

Our aim is to employ the fabricated hemispherical nanomagnets on silicon nitride membranes for spin-mechanics experiments, where their magnetic field gradients $\frac{\partial B}{\partial z}$ can be measured using lifted-mode scanning NV magnetometry. We propose using a magnet capable of applying an out-of-plane (OOP) magnetic field to magnetize the cobalt nanomagnet, while performing SNVM measurements with an (111) diamond tip [88], with the saturation field also applied OOP. Magnetic saturation can be determined using Dynamic Torque Magnetometry. [89]. To facilitate this measurement, the frequency of one or several suitable mechanical modes of the silicon membrane is measured as a function of an externally applied magnetic field. The membrane acts as a transducer for the magnetic torque $\tau = m \times B$ exerted by the nanomagnet. This induces a shift in the resonance frequency of the membrane, which approaches a horizontal asymptote for high enough applied fields. The value of the asymptote depends on the saturation magnetization M_s. The SNVM measurements will yield a characterization of the magnetic field strength at various distances from the NV center.

Moreover, we will consider optimizing the magnetic properties, such as through annealing the magnets (refer to A). The subsequent step involves calculating the cooperativity by incorporating the field gradient derived from SNVM, which is defined by the following formula:

$$C_{SM} = \frac{g_{SM}^2 T_2}{\gamma_M}, \tag{4.2}$$

where $g_{SM} = g_e x_{zpf} \frac{\partial B}{\partial z}$. Our objective is to achieve quantum cooperativity $C_{SM} > 1$ to enable coherent spin-phonon interactions. Furthermore, it is essential to measure the quality factor Q of the silicon nitride membrane post-deposition, as it may deviate from the ideal values measured immediately after fabrication in vacuum. Based on the outcomes of these measurements, we will optimize various components of the system to attain the desired operational regime.

5 Magnetic gradients for electron spin qubit control

Results presented in this chapter have been published as: Scanning NV magnetometry of focused-electron-beam-deposited cobalt nanomagnets, ACS Applied Nano Materials 7, 3854-3860 (2024)

This chapter presents a detailed study on the characterization of Co nanomagnets for electron spin qubits using FEBID. Funded by NCCR SPIN and conducted in collaboration with EPFL and IBM Zürich, this research explores FEBID as a novel technique for 3D integration in quantum computing devices.

We begin with an introduction to fundamental concepts of Electric Dipole Spin Resonance (EDSR), including individual addressability and dephasing, which are critical sources of noise in electron spin qubit devices. In Section 5.2, we characterize these Co nanowires through a combination of magneto-transport measurements, magnetic imaging with NV centers in diamond (SNVM), transmission electron microscopy (TEM), and electron diffraction X-ray spectroscopy (HAADF-STEM) to assess their magnetization saturation and crystallinity.

To better understand the complex results of our fabrication process, simulations of an ideal Co bar are discussed in Section 5.3. Comparing SNVM, TEM and AFM (Section 5.4) measurements, significant nanoparticles surrounding the deposit are revealed, which may impact qubit performance by introducing magnetic noise and unwanted qubit rotations. We propose adding a charge noise term and a decoherence term in the EDSR driving model to quantify these effects. The estimated impact of charge noise and decoherence, as a function of spatial coordinates, is analyzed in Section 5.5. Section 5.6 provides an outlook on future research directions. Overall, this chapter outlines the process of characterizing Co nanomagnets for electron spin qubits fabricated with FEBID, focusing on enhancing magnetic gradients for EDSR, minimizing charge noise, and exploring scalability and 3D integration in quantum devices.

5.1 Motivation

There is a variety of applications today which could benefit from nanomagnets grown by the FEBID technique. In particular, within this thesis, we will explore the application of using them for achieving spin rotation in spin qubit devices. In order to understand the requirements for the geometry of such a nanomagnet, we will need to

consider the constraining physics in a typical spin qubit device that will impact our fabrication parameters.

5.1.1 Spin rotation

Fast and coherent manipulation of a single spin state is the objective we aim to reach when designing a system based on electron qubits.

The quality factor of the system needs to be high enough to allow for Rabi oscillations to occur until the system loses coherence, which translates to gate errors below the error correction threshold [90]. Implementing a robust hardware setup for qubit gates is essential to ensure they remain effective despite minor deviations during the fabrication process and can scale to accommodate numerous qubits. Electron spin resonance (ESR) is a manipulation technique that involves alternating magnetic fields, typically generated by a stripline positioned above the sample. However, addressing a single spin qubit in a multi-qubit device with striplines is challenging because it requires precisely localized magnetic fields. This requires the use of high currents to manipulate magnetic field, which results in increased power consumption. One solution to this problem is utilizing the Stark shift to individually tune spin resonances. This approach requires the application of large electric field gradients and the integration of additional electric gates. Alternatively, EDSR has demonstrated the ability to universally control spin qubits. EDSR utilizes alternating electric fields, which are conveniently generated by existing electrostatic gates and can couple to the electron spin through mechanisms such as spin-orbit coupling, nuclear hyperfine interaction, or the stray field from a micromagnet across the quantum dot. The stray field from a micromagnet can cause shifts in the Zeeman energy, thus enabling the individual addressing of spin qubits [23].

For host materials like silicon and carbon, which exibit low spin-orbit and hyperfine coupling, only the third coupling mechanism (the stray field from a micromagnet) will achieve a MHz Rabi frequency [91, 92]. Silicon- and carbon-based systems are advantageous because nuclear spins can be eliminated through isotopic purification, which significantly extends spin relaxation time and dephasing time. This leads to lower gate errors compared to III/V semiconductors [23, 93].

Various magnet designs have been proposed and realized for spin qubit manipulation in silicon-based quantum dots, including single or split micromagnets fabricated on top of or adjacent to the metallic depletion gates that electrostatically define the quantum dots, single and split nanomagnets integrated into the depletion gate pattern

[94]. More recently, research on micromagnet designs advanced in making improved micromagnets for linear chain arrays with modified geometry [95, 96].

We note from the work of other authors ([94]), that the distance of the micromagnet to the quantum dot plane is important for choosing the right fabrication parameters for the micromagnet. One can imagine the stray field of the micromagnet emanating toward the critical plane, where the double quantum dot lies. Therefore, when we speak of magnetic gradients in a qubit device, we start from determining the Cartesian system coordinates in which the DQD lies. As an example of this calculation, we will refer to the previous work of other authors [94] and use it as our guideline in magnet design. On Fig. 5.1(a), the DQD is aligned along the x axis. Secondly, we look at the direction of the external field applied to drive the spin qubit experiment, in this case the authors described the electron spin dipole resonance (ESDR), and the field applied was in z direction. For complete driving, one needs also microwave excitation which is typically applied via the metal gates. As illustrated in Fig. 5.1(b) the driving will cause the electrons to move in z direction (similar operation is described in [97]).

Now we can define our magnetic gradient: we know the gradient is a derivation of the magnetic field in the spatial coordinates of the qubit system we observe - it is a tensor of x,y and z coordinates in the Cartesian system. Since the electrons move in z direction, following the gradient of the magnet in y and x direction (perpendicular to the external field), it would allow the electron to move along the Bloch sphere. Therefore, the gradient we want to control, is the one perpendicular to the direction of the externally applied field. Knowing the magnitude of the total gradient at a certain point in the Cartesian system, defined by vector **r**(x,y,z) is the square-root of the sum of squares of the derivates of the magnetic field in x and y direction per z:

$$G^{tot}(\mathbf{r}) = \sqrt{\left(\frac{\partial B_x(\mathbf{r})}{\partial z}\right)^2 + \left(\frac{\partial B_y(\mathbf{r})}{\partial z}\right)^2} \tag{5.1}$$

The Rabi frequency f_R is proportional to the total gradient through (from [94]):

$$f_R = \frac{g\mu_B z_0}{2h} \times \int \left|\psi(x,z)\right|^2 G^{tot}(\mathbf{r}) dx dz, \tag{5.2}$$

where g is the electron g-factor, μ_B the Bohr magneton, h Planck's constant, and z_0 the amplitude of the dot displacement in the z direction. We can conclude based on eq.5.2 that the spin rotation is driven by the ac components of a magnetic field, and that they are perpendicular to the total magnetic field experienced by a spin qubit. We also note that the total magnetic field gradient, G^{tot}, is averaged over the electron's

probability density function, $\left|\psi(x,z)\right|^2$. This is modeled using a Gaussian distribution, assuming the electron is in its ground state within a harmonic potential.

According to electrostatic simulations from Kawakami et al.[91], the dot displacement is dependent on the microwave amplitude. The electrons also get displaced along the x-direction, but this contribution to the Rabi frequency is small because the stray field gradient along x is small. Therefore, the magnetic field dependence is mainly determined by the perpendicular gradient, G^{tot}

$$\overrightarrow{B_{tot}} = \overrightarrow{B_{ext}} + \overrightarrow{B_{mm}} \tag{5.3}$$

where $\overrightarrow{B_{mm}}$ is the magnetic field at the spin qubit generated by the micromagnet. In a typical EDSR experiment, $\left|\overrightarrow{B_{ext}}\right|$ is chosen to be rather large (few 100 mT to 1 T), and $\overrightarrow{B_{tot}}$ points approximately along $\left|\overrightarrow{B_{ext}}\right|$. In the example above, the external field is aligned with the z-axis, therefore the spin rotation will be driven by $B_x(t)$ and $B_y(t)$ field components.

The externally applied magnetic field causes a splitting of the energy levels of the electron into two states: spin-up and spin-down, and this difference is known as the Zeeman splitting. The frequency that corresponds to this energy difference is the Larmor frequency:

$$f_L = g\mu_B\left|\overrightarrow{B_{tot}}\right| \tag{5.4}$$

In order to drive a transition between the two levels an oscillating electromagnetic fields needs to be applied, like a microwave field, that has an energy equal to the Zeeman splitting. This occurs when the oscillation frequency of the field is equal to the Larmor frequency.

The shaking can be achieved by applying an ac voltage to one of the gates, and the direction of the shaking will determine which derivative of the magnetic field can drive the spin rotation (see Fig.5.1)(b). The derivatives involved in the rotation for the device shown in Fig.5.1(a) are $\frac{\partial B_x}{\partial x}, \frac{\partial B_x}{\partial y}, \frac{\partial B_x}{\partial z}$ and $\frac{\partial B_y}{\partial x}, \frac{\partial B_y}{\partial y}, \frac{\partial B_y}{\partial z}$.

On Fig.5.1(a), the microwave voltage is applied to the lower gate as indicated by the blue arrow, the left quantum dot will oscillate back and forth in the x direction (Fig.5.1(b)), so the driving of the spin rotation will be executed by the $\frac{\partial B_x}{x}$ and $\frac{\partial B_y}{x}$ derivatives. In the context of electron spin resonance (ESR) experiments, the oscillation of the quantum dot is most effectively achieved along directions where the confinement potential is weakest. This is because weaker confinement means the potential barriers confining the electron are lower, allowing the electron to move

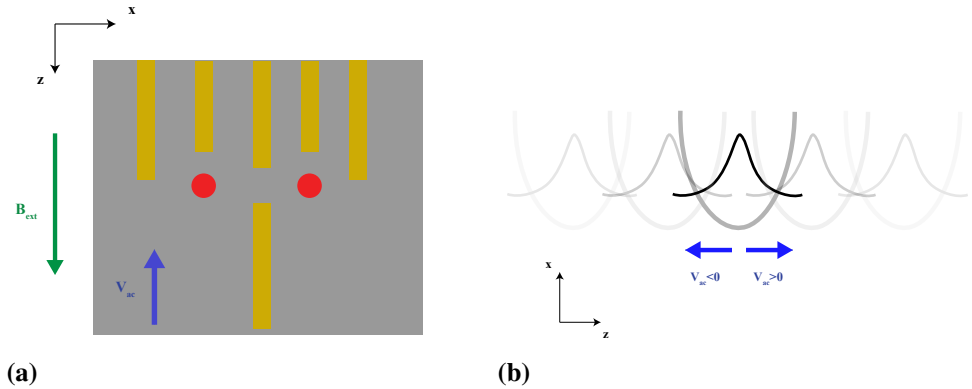

FIGURE 5.1 — Top view and shaking mechanism of the QD in the Si/SiGe heterostructure.
(a) Top view of the Si/SiGe heterostructure, illustrating the position of quantum dots within the two-dimensional electron gas (2DEG) plane. (b) Schematic representation of the shaking mechanism, highlighting the interaction of the electric field with the spin states in the quantum dots.

more freely. Consequently, in these directions, it is easier to manipulate the electron's spin states with external magnetic fields and microwaves. Therefore, when designing ESR experiments or analyzing spin dynamics, focusing on these directions can lead to more effective control and measurement of the electron spin transitions.

In quasi-1D semiconducting devices, such as Si nanowires and FD-SOI, the electrons are confined in two dimensions and they move freely along the third dimension (the principal double dot axis). This is because the weaker confinement in that direction requires less energy to achieve the oscillations needed for EDSR, making the conditions for spin manipulation more favorable.

5.1.2 Individual addressability

Device in Fig.5.1(a) confines a double quantum dot, which can be used to make a spin qubit. In this subchapter we briefly consider the constraints posed by the nearness of two quantum dots, which can be extended also to an array of quantum dots. Two cases are commonly considered: 1) the electron spin is manipulated by a single electrostatic gate, or 2) it is controlled by two gates that are separated. In the latter case, the electrons move independent one of the other, and in the first case their positions are coupled due to single-gate manipulation [94]. In the case when the electron spin is manipulated by a single electrostatic gate (1), which affects the electrons in both quantum dots, it is necessary that the local magnetic field has a sufficiently large gradient, such that, the difference of the Zeeman splitting at the two quantum dot locations is larger than the linewidths of the individual spin qubit

resonances. We can calculate the linewidth from the inhomogeneous dephasing time and power broadening due to the spin resonance $\Delta f_L \sim \frac{1}{T_2^*} + f_{Rabi}$. In the case 2), this is not a requirement, however, it is an advantage for decreasing the electrostatic cross-coupling effects [98]. The aformentioned condition can be written as:

$$\Delta B_z(\mathbf{r}_1, \mathbf{r}_2) = \left| B_z(\mathbf{r}_1) - B_z(\mathbf{r}_2) \right|, \tag{5.5}$$

where $\mathbf{r}_1$ and $\mathbf{r}_2$ are the positions of dot 1 and dot 2. In the regime where we would like to operate our device, the dephasing is slow comparatively to the Rabi oscillations which are fast (and thus a wide spectral line), the frequency difference between the two dots is still resolvable $\Delta B_z > 2 f_{Rabi}/(g\mu_B)$.

5.1.3 Dephasing

To describe the spin qubit logical state, we often use the terminology of a Bloch sphere. On Fig.5.3 is its illustration, where the z axis shows the $|0\rangle$ state at the top, and the $|1\rangle$ state at the bottom.

The fabrication process imperfections and the environment in which we drive the spin qubit are sources of noise, that manifest in dephasing rates on the Bloch sphere. We distinguish two different rates: there is a phase delay in xy plane (depicted in red) Γ_ϕ, or a disturbance in the z direction Γ_1. This disturbance is caused by noise of the equipment that applied the external field (coil noise, oscillator noise of the waveform generator, etc.), often referred to as microwave driving noise. On the other hand, the material used to confine a spin qubit (Si/SiGe) has charge noise, that can also cause dephasing.

We discuss here the case of dephasing when it is caused by the fluctuation of the magnetic field along $\overrightarrow{B_{tot}}$ (total magnetic field). Considering device geometry from Fig.5.1(a) the charge noise and the microwave driving noise may cause dephasing through $\frac{\partial B_z}{\partial x}, \frac{\partial B_z}{\partial y}, \frac{\partial B_z}{\partial z}$. During the nanomagnet design, we will aim to minimize these derivatives, while ensuring that $\frac{\partial B_z}{\partial x}$ is sufficiently large to guarantee individual addressability.

5.2 Characterization of magnetic properties

We aim to characterize the magnetic properties of the deposit to be able to benchmark our nanomagnet among other nanomagnet options produced by e-beam evaporation or MOCVD. This step in the fabrication process is critical to evaluate the quality of fabrication, and to further optimize the fabrication recipe. The second reason is that we

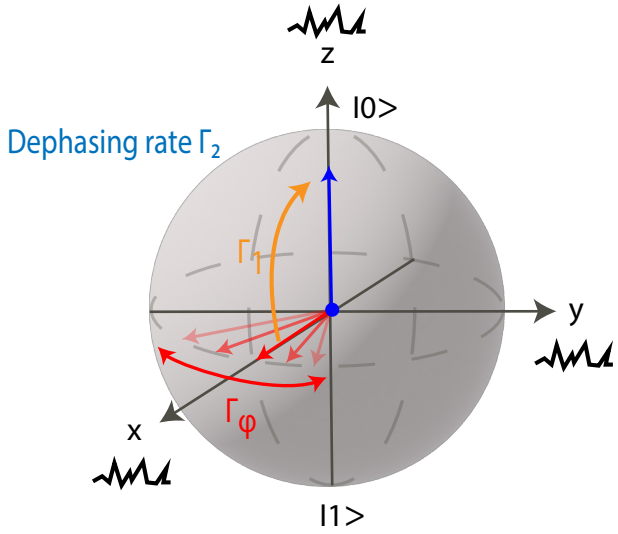

FIGURE 5.2 — Dephasing time definition on a Bloch sphere.
The Bloch sphere representation illustrates the two dephasing rates: Γ_1, which indicates the disturbance in the z-direction, and Γ_ϕ, which denotes the dephasing in the xy-plane. The ac field is applied in the z-direction.[25] The curve on the axis symbolises the noise effect on the spin qubit system.

may want to compare our fabrication method with other available methods, and estimate the quality versus cost, especially when considering large-scale fabrication. We chose to estimate the electrical properties of the nanomagnet via magneto-transport measurements which we discuss in 5.2.1. Further, we use SNVM to image the magnetic stray field emanating from our nanomagnet in 5.2.2 and perform HAAF-STEM in 5.2.3.

5.2.1 Hall-effect in FEBID Co nanowires

Magneto-transport measurements are experimental techniques used to characterize new materials by studying their electrical properties, typically by measuring their magnetoresistance. In magnetic materials where there are predominantly electron or hole carriers, we can exploit the Hall effect to facilitate a measurement of the material's magnetoresistance. The working principle is as follows; a current I is applied in the plane of the thin film, and a magnetic field, $\mathbf{B}$ is applied perpendicularly to the thin film and the current plane. As a consequence of the Lorentz force, there is a build-up of electrons on one side of the contacts, where a Hall voltage is measured. The measurement is depicted on Fig.5.3(a). In the steady state, the built-up Hall voltage V_H is in the y direction and it is compensated by the Lorentz force on an electron,

acting as well in the y direction. The Lorentz force acting on an electron moving in the x direction can be defined as [99]:

$$\mathbf{F}_y = -e(v \times \mathbf{B})_y - eE_y = ev_x B - eE_y = 0 \tag{5.6}$$

Here $E_y = \frac{V_H}{w}$ is often referred to as the Hall field. Assuming that the current is carried predominantly by electrons, as expected for metals, the current density in x direction is [99]:

$$j_x = \frac{I}{wt} = -nev_x \tag{5.7}$$

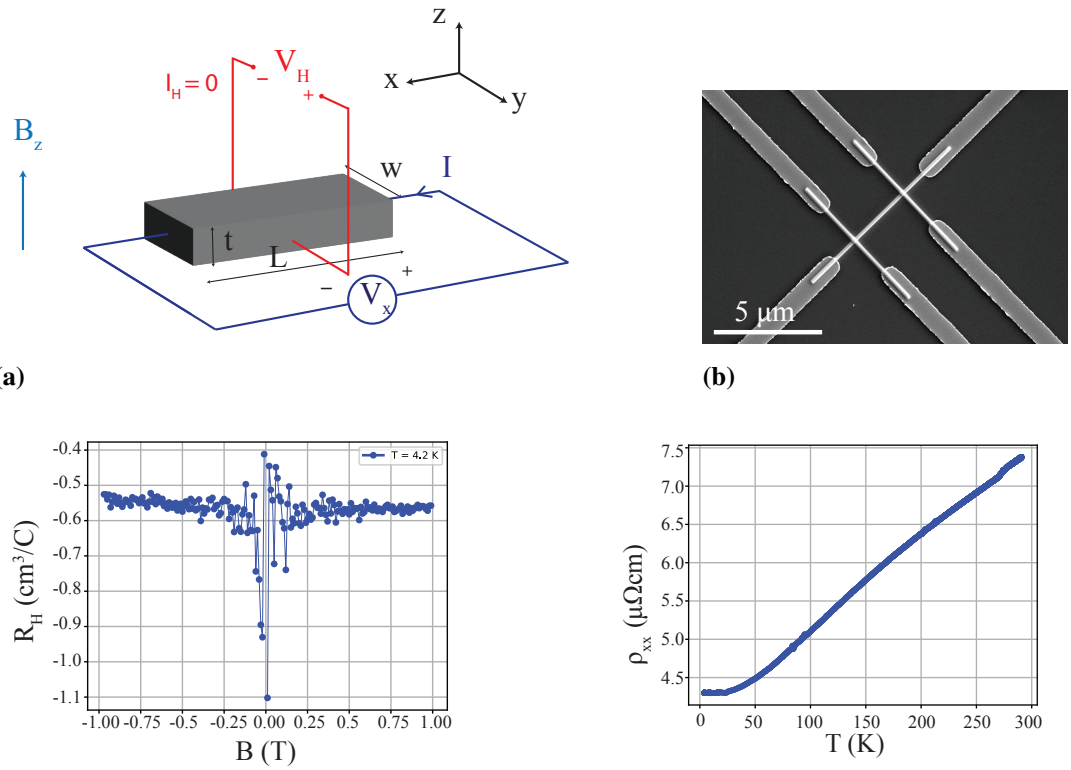

Figure 5.3 — Hall-effect in FEBID Co nanowires.
(a) Schematic of the basic principle of a typical Hall effect measurement. (b) FEBID Co nanowires deposited in a 6-contact geometry. The wire thickness t is 275 nm and the width w is 300 nm. (c) Hall coefficient R_H vs. magnetic field. Note the significant increase in noise near 0 mT resulting from the poor signal-to-noise ratio when the Hall voltage is smallest, amplifying the effect of uncompensated DC offsets.(f) Longitudinal resistance ρ_{xx} vs. temperature confirms metallic behavior.

and thus it follows:

$$E_y = \frac{V_H}{w} = -\frac{1}{ne} j_x B = -\frac{1}{ne}\frac{IB}{wt} \tag{5.8}$$

The prefactor $-\frac{1}{ne}$ is called the Hall constant and denoted as R_H. We can directly access the R_H from the measurement of the Hall voltage V_H, current I and B from:

$$V_H = R_H \frac{IB}{t} \tag{5.9}$$

We prepare a 6-contact Hall bar geometry, grown by e-beam evaporation 5/50 nm Ti/Pd, and, deposit cobalt nanowires with FEBID (see Fig.5.3(b)). We bond our device with Al wires and measure it inside the dilution refrigerator with capability of measuring at 1 K, and we sweep the external field perpendicularly to the sample, from −1 T to 1 T with steps of 1 mT.

We calculate the Hall resistivity $\rho_{xy} = \frac{V_{xy}}{I} \cdot \frac{w \cdot t}{L} = 0.128\,\mu\Omega\,\text{cm}$, the longitudinal resistivity $\rho_{xx} = \frac{V_{xx}}{I} \cdot \frac{w \cdot t}{L} = 25.378\,\mu\Omega\,\text{cm}$ and the Hall coefficient R_H (see Fig.5.3(c)).To conclude, by comparing these values to the literature [28, 100], the resistivities of our FEBID Co thin films are comparable to the literature FEBID Co films, indicating a high quality of the material. Further, we acknowledge that we cannot draw conclusions about the switching field from these measurements as the data gets very noisy from −20 mT to 20 mT. To provide a reference, in previous work [100], in nanowires with similar properties the switching fields reportedly occurred at 15 mT.

The Hall coefficient of bulk cobalt at 4.2 K is $-5.3 \times 10^{-5}\,\text{cm}^3/\text{C}$ [101], we compare it with the Hall coefficient of $-5.2 \times 10^{-3}\,\text{cm}^3/\text{C}$ in FEBID Co sample at 4.2 K. After substituting R_H and elementary charge e in equations 5.8 and 5.9, we calculate the charge carrier density to be $n \approx 1.21 \times 10^{21}\,\text{cm}^{-3}$. Considering charge carrier density of $9.1 \times 10^{22}\,\text{cm}^{-3}$ in bulk, we can calculate $\frac{n_{bulk}}{n_{FEBID}} \approx \frac{9.1 \times 10^{22}\,\text{cm}^{-3}}{1.21 \times 10^{21}\,\text{cm}^{-3}} \approx 76$. So, the concentration of carriers is around 76 times smaller in FEBID Co than in bulk Co at 4.2 K. The concentration of carriers in the FEBID Co thin film is generally lower than in bulk, as calculated from the Hall coefficient (R_H), possibly due to a higher concentration of defects, impurities, or the polycrystalline structure of the FEBID Co [102].

Subsequently, we perform a R-T measurement, thereby confirming fully metallic behavior of the nanowires as shown in Fig.5.3(d), perfectly agreeing with findings from the literature [100].

5.2.2 Scanning NV magnetometry

Scanning NV magnetometry was the technique of choice due to its remarkable spatial resolution on the nanometre scale, close to the size of the electron wavefunction in a typical electron spin qubit device from 10 nm to 100 nm. Further, the technique

operates well on the range of magnetic fields we expect for stray field profile of FEBID-grown Co nanomagnets, which is up to 5 mT. We operate the experiments in a commercial ProteusQ system at room temperature as described in Section 3.3.2, equipped with a permanent magnet positioned below the sample. The magnet can be operated through a user interface where we select the desired field value we want to apply to the sample in plane and in the horizontal direction (corresponding to x-axis in the Fig.5.6). We acquire the magnetic signal through the ODMR of the NV center in the diamond tip positioned on the tip of the quantilever. During the experiment, a green laser was optically exciting the electronic states of the NV center and a microwave antenna was delivering power on the frequencies corresponding to the diamond bandgap. Hence, by enabling the proper operation, the emitted photons were collected via an APD camera inside the optical objective. The magnetic field was computed through the Qudi software [103], where the NV physics is implemented for computational operations. The AFM settings were set to scan line-by-line starting from the lower left corner in horizontal direction. For our experiments, we use a [100] tip, in which the quantization axis is positioned in-plane. We proceed the characterization by performing a quantitative Full-B measurement on the Co Hall bar device as shown in Fig.5.4. The applied field is changed with the external magnet, where the field direction corresponds to the anisotropy of the horizontal wire of the Hall bar structure. We apply a magnetic field externally, and immediately after we aquire the magnetic image. We start with an image acquired at an external field of -6.6 mT, then we apply 196 mT, and go back to a low field of 0 mT. We observe drastic changes in the magnetic picture, and we find that the horizontal wire is fully saturated for the field close to 200 mT as shown in Fig.5.4. By applying a field of -280 mT and aquiring the magnetic image, we observe the saturation of the wire again, only with spins pointing in the -x direction (see Fig.5.4). On the magnetic field values close to 0 mT, we observed a disordered magnetic signal that can be explained by the presence of multi-domains in the cobalt material grown by FEBID. Further, there is clearly a non-negligible contribution of magnetic signal from the nanoparticles surrounding the magnetic structure. We observe a strong dependence of the state of the system on its history, and for values above 200 mT we observe a fully saturated state of the horizontal nanowire. Due to strong quenching of magnetic field perpendicular to the quantization axis of the tip (in-plane), we observe spurious data points in the location where the vertical wire is positioned.

The external field values should be choosen such that at the chosen external magnetic field values there are no anti-crossings of the NV energy levels, which can be checked *a priori* by running an ODMR measurement for a full sweep of the magnetic range of the

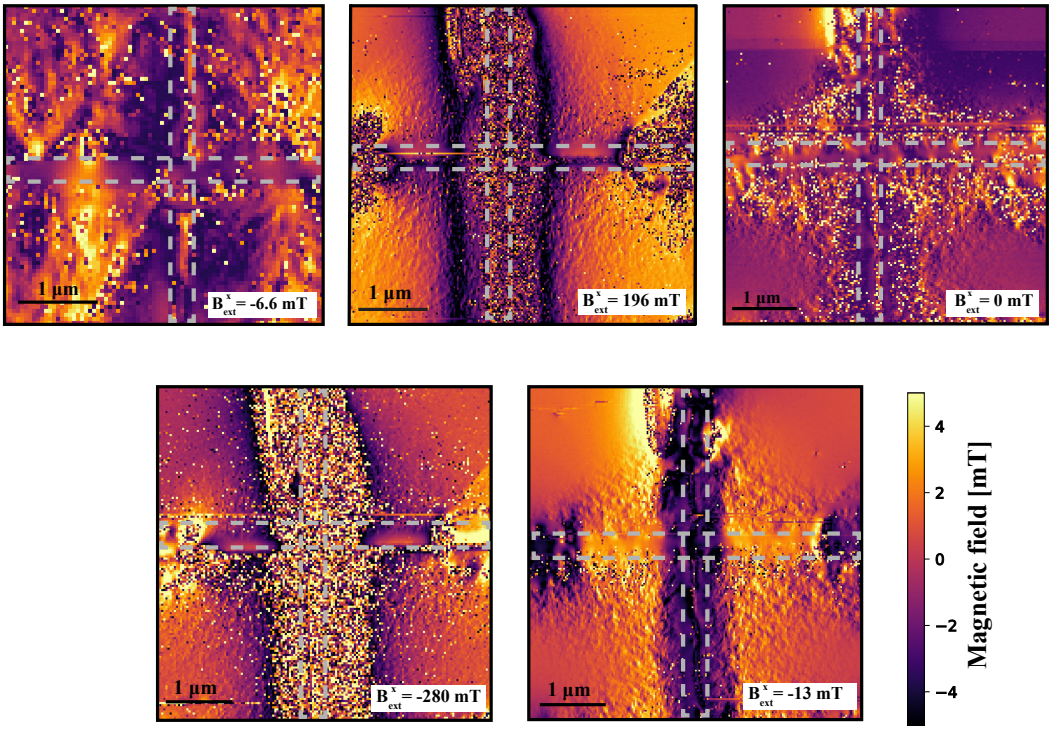

FIGURE 5.4 — Hysteresis imaged by SNVM of a cross-section of FEBID-grown Co NWs in a 6-contact Hall configuration.
Upper row (from left to right): (1) Horizontal field applied: -6.6 mT, (2) 196 mT, (3) 0 mT. Lower row: (1) -280 mT, (2) -13 mT.

external magnet. Then an automatized script can be set to perform the measurements sequentially. The measurement time depends on the scanning area, the number of pixels, and the integration time per pixel. A single quantitative magnetic image with scanning area of 10 µm × 10 µm, 200 pixels by 200 pixels, and an integration time of 100 ms takes 13 h and 43 min. One magnetic field value is associated to a pixel with the size of 50 nm.

In the second experiment, we simplify the magnetic geometry to a single wire, grown by FEBID and with the geometry as shown in Section 5.2.1. We choose the length of the nanowire to be much larger than its width and height in order to force the anisotropy in that direction, such that a full saturation can be achieved by applying an external field in the same direction. We applied a field close to the one found to fully saturate the horizontal bar, in this case $B_{ext,x}$ = 202.5 mT. We chose the AFM scan direction to be vertical, starting from the lower left edge. The experiment is depicted in figure 5.6(a). The image 5.6(b) shows the magnetic field, it is clearly visible the wire is fully polarised at this field, and we clearly see the field exiting and entering the wire at the edges, e.g. we see the magnetic monopoloes at the wire

edge. The wire is slightly tilted, therefore there is a slight asymmetry in the size of the monopoles. At the very edge of the wire, we expect the field to be perpendicular to the in-plane direction corresponding to the sensitive axis of the diamond tip, which explains the spurious data points at these positions. From this image we can calculate the magnetization saturation, as will be shown in Section 5.3. The image was taken on an area of 18 µm×6 µm with pixel number in x equal to 150 and pixel number in y equal to 50, giving a pixel size of 120 nm. The tip was showing intrinsically low contrast in the ODMR experiment of 8% which limits the magnetic sensitivity of the measurement, as shown in 5.6(c). The loss of contrast is the strongest at the wire edges, due to quenching, and at the very end of the scan (right side of the image), which we suspect comes from the tip degradation with time. On the image showing fluorescence, e.g. counts/second, we can see clearly the topography effects of the wire, e.g. higher number of counts at the edges of the wire, from where we also confirm our hypothesis that the loss of magnetic signal at the end of the wire comes from the perpendicular magnetic field component. Image 5.6(e) shows the AFM height in nanometers. The last image in the left panel 5.6(f) shows the tuning fork magnitude in arbitrary units.

With these two experiments, we have acquired quantitative magnetic field of our FEBID-grown nanomagnets. By tailoring the shape of the magnet in a clever way, we were able to fully exploit the system capabilities to quantify their magnetization saturation as will be shown in 5.3. In addition, we have become aware of the strong magnetic field contribution from the nanoparticles surrounding the structure, whose effect on spin qubit operation we will further analyze in **??**.

5.2.3 High-angle annular dark-field scanning transmission electron microscopy (HAADF-STEM)

High-angle annular dark-field scanning transmission electron microscopy (HAADF-STEM) is a STEM method which forms images by collecting scattered electrons with an annular dark-field detector. The annular dark field detector, collects electrons from a ring around the beam, sampling far more scattered electrons than can pass through an objective aperture. The annular dark field image is formed by incoherently scattered electrons (scattered from the nucleus of the atoms via Rutherford scattering) - instead of Bragg scattered electrons. The technique is highly sensitive to variations in the atomic number of atoms in the sample, e.g. the image is based on the contrast dependent on the atomic number Z. It is typically used for characterization of nanoparticles, thin films, and nanostructured materials. In

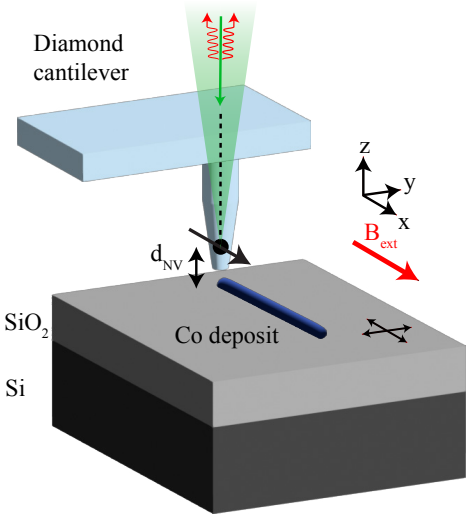

FIGURE 5.5 — Schematic of the experiment on a single Co NW.

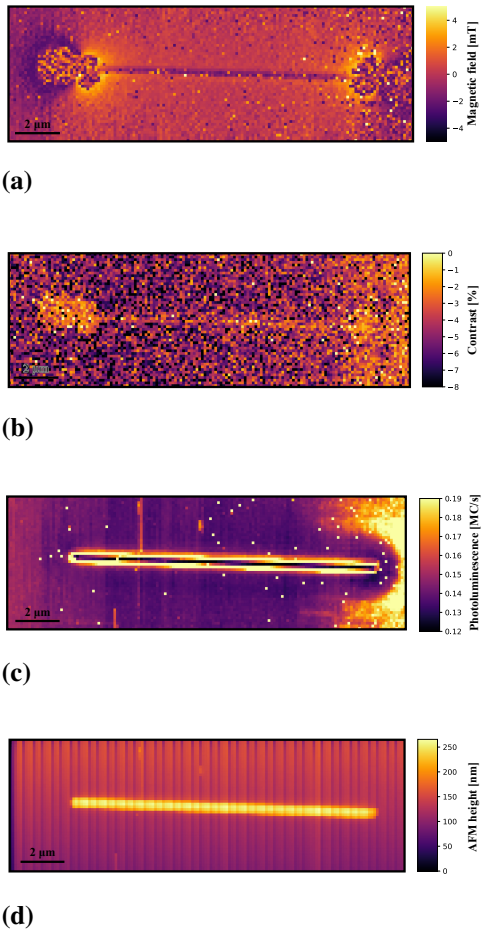

FIGURE 5.6 — Scanning NV Magnetometry of a single FEBID Co nanowire at room T. (a) Magnetic field map of the nanowire. (b) Magnetic contrast image shown in negative to highlight photoluminescence variations. The contrast gets degraded at the edge of the scan. (c) Photoluminescence signal from the nanowire region. (d) Atomic Force Microscopy (AFM) height map showing the topography of the nanowire.

elements with a higher atomic number Z, more electrons are scattered at higher angles due to greater electrostatic interactions between the nucleus and the electron beam. Owing to this reason, the HAADF detector senses a greater signal from atoms with a higher Z, leading them to appear brighter in the final image.

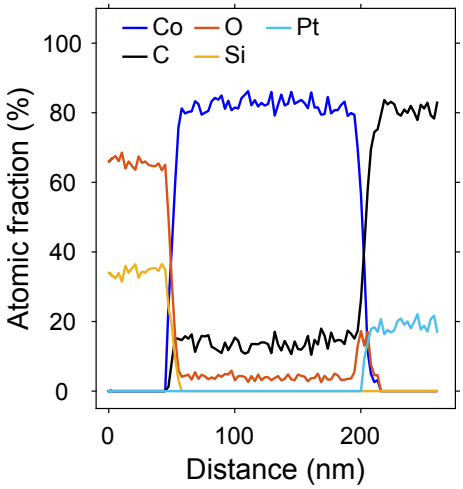

FIGURE 5.7 — EDS analysis along the line cut shown in 5.8(a)

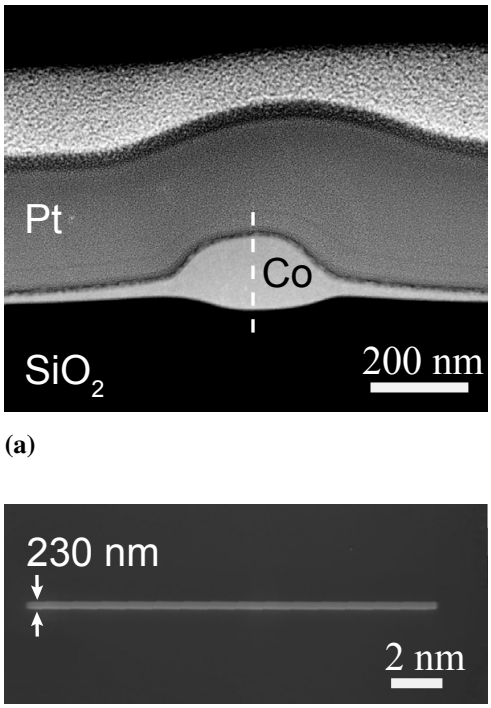

FIGURE 5.8 — (a) High-angle annular dark-field scanning transmission electron microscopy (HAADF-STEM) image showing a cross-sectional view of a cobalt (Co) nanowire (NW) nanomagnet, similar to those investigated in this study. (b) Scanning electron microscopy (SEM) image of the Co nanomagnet examined in this work.

For our experiment, we used the system available at the Swiss Nanoscience Institute - STEM JEOL JEM-F200 cFEG. The system is equipped with a cold field emission gun, with acceleration voltages from 20 to 200 kV, it is characterized with a spatial resolution of 0.14 nm in STEM-HAADF mode, and it allows imaging of sample sizes of 3×3 mm. In figure 5.8 (a), an SEM top-view image of a Co NW deposit is shown, with the same dimensions as mentioned in 4.2.1, and figure 5.8 (b) shows a HAADF-STEM image of a cross-sectional lamella of such a deposit. Before lamella preparation, the sample was covered with a layer of Pt grown through FEBID, to protect the Co deposits while milling the lamella. Thinning and polishing of the lamella was done with an ion acceleration voltage of 30 kV and currents of 0.24 A and

83 pA, resulting in a lamella thickness of ~65 nm. In figure 5.8 (b), the rounded cross-section of the Co NW can be discerened, as well as "halo" side-deposits extending laterally for several microns. The "halo" deposit in figure 5.8(b) has a thickness of roughly 30 nm directly next to the NW, which gradually tapers off away from the NW. A selective area electron diffraction (SAED) measurement of the cross-section shown in figure 5.8(c) indicates that the deposited Co is polycrystalline (figure 5.10).

Although hard to distinguish in the cross-sectional TEM image, the Co deposit indeed shows a granular composition, with grain sizes of roughly 2-10 nm. Such grain sizes are consistent with values found in previous works for as-deposited (non-annealed) Co FEBID structures. The entire deposit is covered by an oxidized shell of roughly 8 nm thickness. Also the oxide layer has a granular composition, with lateral grain sizes of roughly 10-20 nm, corresponding well to previous findings for similar deposition parameters. EDS mapping along the linecut indicated in figure 5.8 (b) reveals a composition consisting mostly of Co (82 ± 2.5 at.%), with additional smaller amounts of C (14 ± 2.5 at. %) and O (4 ± 2.5 at. %). We find that this composition is rather uniform throughout the deposit below the surface oxide layer, including similar proportion in the "halo" side deposits (see figure 5.9). On the image 5.10 we performed SAED on the Co NW cross-section. The first diffraction ring itself indicates polycristallinity, with grains larger than can be imaged here with SAED. As mentioned, analysis of the HRTEM image of figure 5.8 (b) indicates Co grain sizes of roughly 2-10 nm.

5.3 Simulation of magnetic bars

In this subsection, we will present the simulation results we obtained in MuMax3. Micromagnetic simulations are computational tools often used to predict a behaviour of a magnetic system. We model the geometry of our system, assign the system properties of the material, and we can predict the evolution of the system when applying an external field.

In this work, we simulated a bar similar to the fabricated Co NW grown by FEBID. The selected geometry was cuboid, with 250 nm width, 130 nm height and 14.4 µm length. The grid size was selected to match a cell size of 5 nm. The exchange stiffness of Co is $A_{ex} = 14 \times 10^{-12}$ J/m and the damping coefficient $\alpha = 1$. The simulation runs under an applied field in the x direction of the wire (the long axis) from 4 T to −4 T in steps of 25 mT. We compare the magnetic picture of our experiment where a magnetic field of $B_{ext,x} = 202.5$ mT is applied along the long axis of the Co NW deposit with the simulated field at $B_{ext,x} = 200$ mT. We select a line in the x direction and a line in the

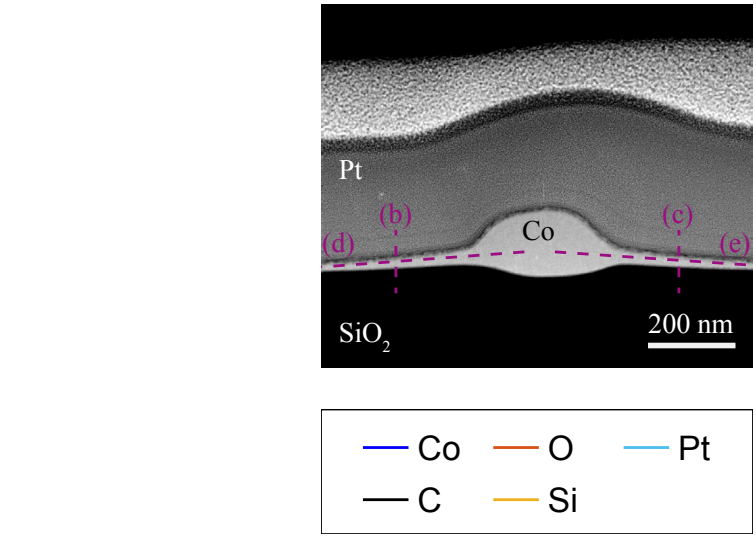

(a)

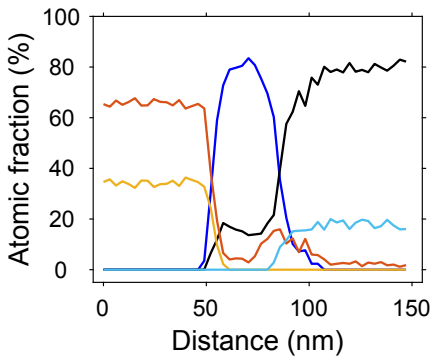

(b)

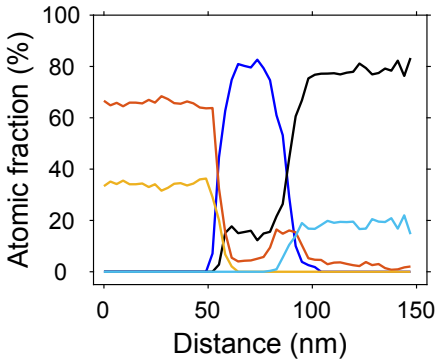

(c)

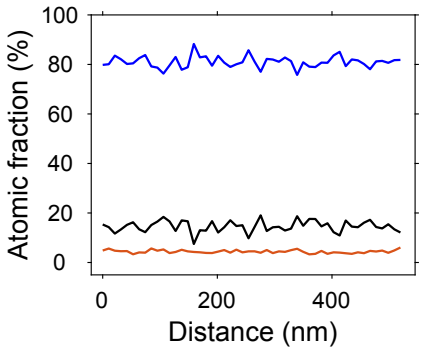

(d)

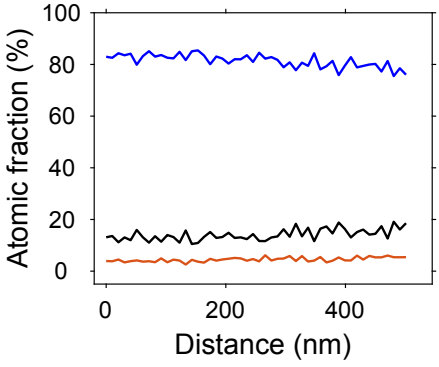

(e)

FIGURE 5.9 — Structural and compositional analysis of a cobalt nanowire.
(a) Top panel: HAADF-STEM image of a cross-sectional slice of a Co nanowire, with dashed lines indicating the positions of the line profiles shown in (b)–(e). Middle and lower panel: Color key corresponding to the elements analyzed. (b)–(e) EDS elemental composition profiles along the indicated linecuts in (a).

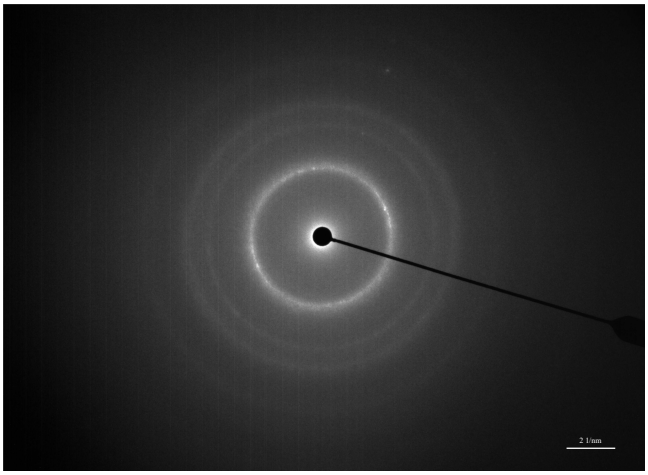

FIGURE 5.10 — Selective area electron diffraction of cobalt nanowire cross-section. SAED image of the Co NW cross-section shown in 5.8 (b).

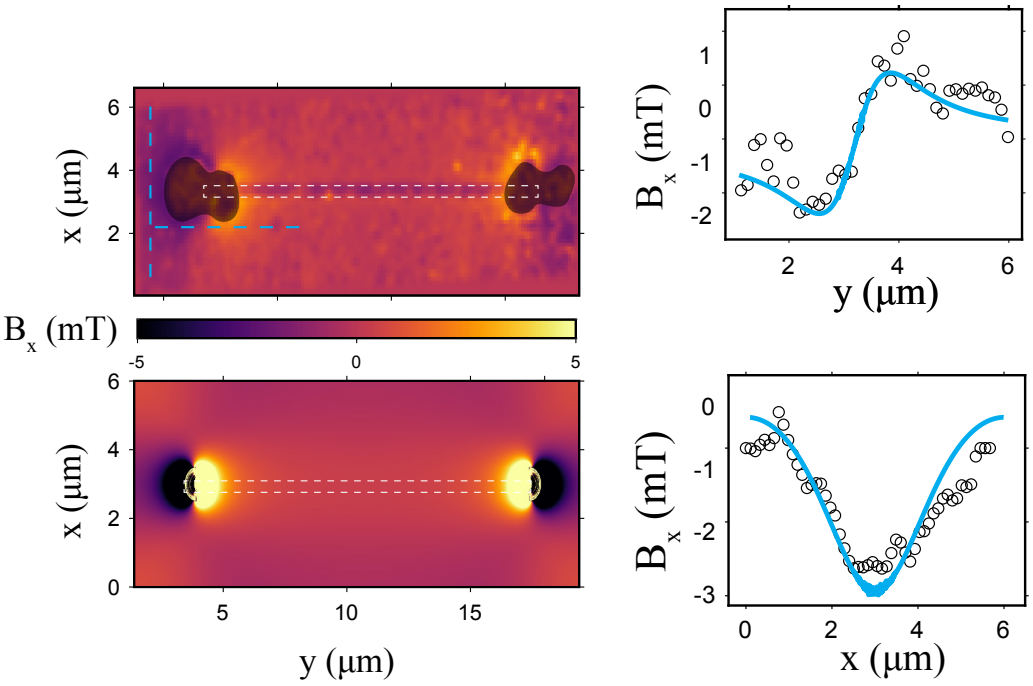

(a) **(b)**

FIGURE 5.11 — Experimental and simulated analysis of cobalt nanowire deposits. (a) Upper panel: Experimental image of the Co NW deposit with the regions of the spurious signal blacked out. Lower panel: Simulation in MuMax3 of a bar filled with cobalt material with $M_{sat} = 1.2 \times 10^6$ A/m. (b) Linecut in the y-direction (upper panel) and x-direction (lower panel) comparing the simulation and experimental results.

FIGURE 5.12 — Simulation of cobalt nanowire geometry including a thin sheet of "halo" in finite difference solver MuMax3.
One side of the NW geometry used for the finite-element simulation. We extrude the Co rich part of the cross-sectional TEM image of Fig. 1c of the main text to the NW length of 14.4 µm and add a rotation of this cross-section to both ends of the NW.

y direction at the same position in the experiment and the simulation, and we plot the linescans as shown in 5.11(b). We find the simulation matches the experiment very well when the magnetization saturation M_{sat} is set to 1.2×10^6 A/m. As a reference, magnetization saturation of bulk Co at room temperature is $M_{sat} = 1.4 \times 10^6$ A/m, which gives in our experiment $M_{sat,Co_{FEBID}}/M_{sat,Co_{bulk}}[\%] = 85$. This result is in agreement with the magnetic content we found through HAAF-STEM.

5.4 Characterization of topography

5.4.1 Atomic Force Microscopy (AFM)

Atomic Force Microscopy (AFM) creates images by scanning a small cantilever over a sample surface. The cantilever has a sharp tip, that touches the surface, causing it to bend and altering the amount of laser light reflected into a photodiode. To maintain a consistent response signal, the cantilever height is adjusted accordingly, allowing mapping of the surface topography through the measured height. We utilized the Bruker/JPK NanoWizard4 AFM system along with the 160AC-NA AFM probe. We have fabricated 42 structures with sizes ranging from 100 nm to 5 nm in both the X and Z dimensions (see figure 5.13). These measurements revealed that the smallest deposit has a height of 15 nm (see Fig.5.14)d, corresponding to the selected X and Z dimensions of 5 nm and 100 nm, respectively, in the patterning software. They also indicate that the actual height slightly deviates from the height specified in the software. This should be considered when choosing parameters for the intended geometric design.

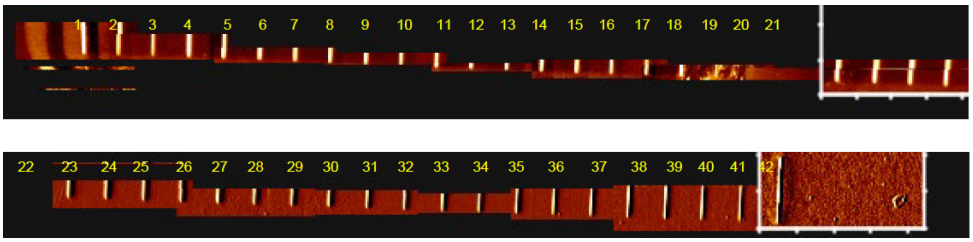

FIGURE 5.13 — Cobalt NW deposits for AFM measurements.
42 Co NW deposits grown by Focused-Electron-Beam-Deposition as selected for AFM measurements.

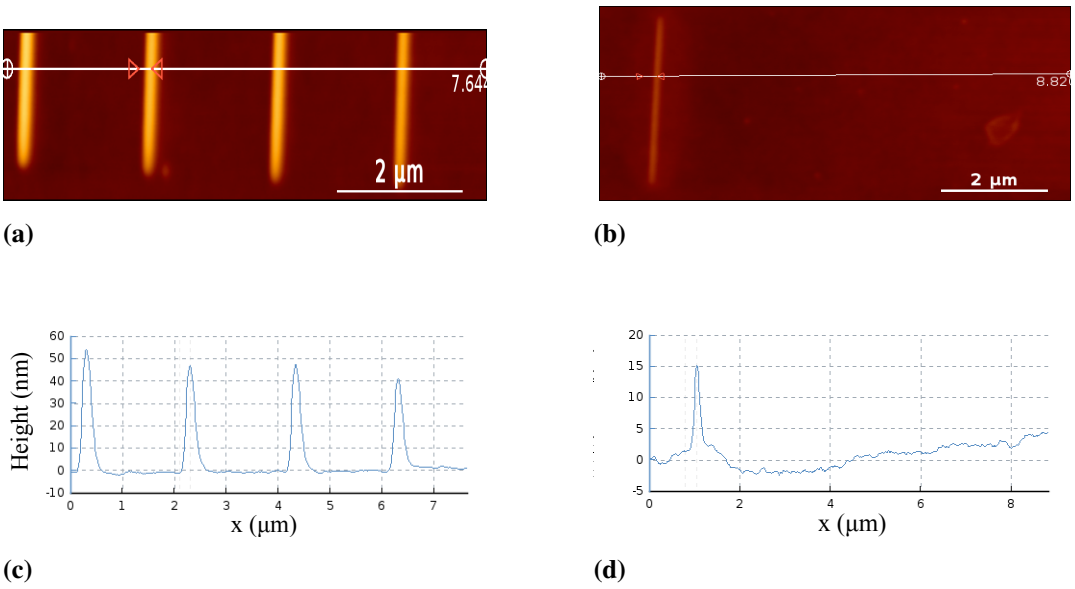

(a) **(b)**

(c) **(d)**

FIGURE 5.14 — AFM characterization of cobalt nanowires: effects of width and height variations.
(a) and (b) AFM height measurements of Co nanowires with equal length, grown with different width and height (X and Z parameters in FIB Helios Patterning Software) where the width is varied and the height is kept constant. We observe that the patterned height decreases as the wires get thinner. In total, we grew 42 structures; 21 structures where Z parameter was varied from 100 to 5 nm while X = 100 nm, and 21 structures where X parameter was varied from 100 to 5 nm while Z = 100 nm. The distance between the wires is 2 µm. The wires were grown under the same conditions: pressure 3.90×10^{-6} mbar to 4.03×10^{-6} mbar, acceleration voltage of 10 kV, beam current 3.2 nA, and dwell time of 1 µs. AFM measurements were taken with a Bruker NanoWizard4 and probe type 160AC-NA. (c) and (d) Linecuts through (a) and (b), respectively, at positions indicated by white lines.

5.5 Spin qubit displacement inside the "halo" stray field

The optical image of a Co Hall bar structure patterned via FEBID (Fig.5.16(a)) reveals a significant "halo" side-deposit [40]. This "halo" appears as a dark, irregularly shaped area in the optical microscopy image. In this subsection of the thesis, we will estimate the impact of the "halo" on the operation of spin qubits. For this purpose, we employ SNVM to examine the "halo"side-deposits in greater detail. We will consider spin qubit dephasing in the scenario when dephasing is caused by charge noise. In this scenario, the typical oscillatory displacement amplitudes of the quantum dot (QD) in electron spin qubits ranges from 1 pm - 1 nm [94, 91].
The SNVM image (Fig.5.16d) of the same area further reveals that the "halo" exhibits a magnetic stray field with a grainy composition. This grainy pattern follows the shape of the dark area visible in the optical image, surrounding the deposit and becoming smoother as it extends away from the deposit.

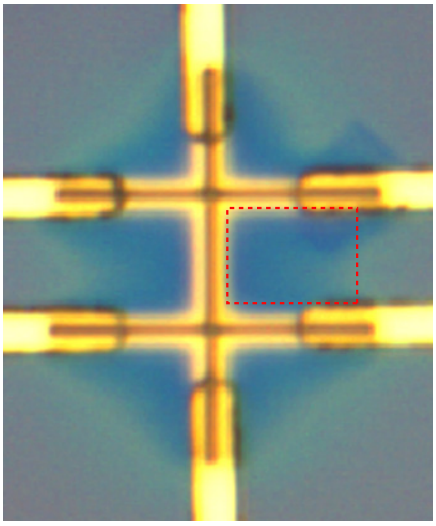

FIGURE 5.15 — Optical micrograph of the device with pronounced "halo".

We investigate the size distribution of the grainy structures, using segmentation analysis (Gwyddion) on a subset of the data as shown in Fig.5.16(b). We find that the typical equivalent square side length, a_{eq}, is approximately 100 nm, which is larger than the scan's pixel size of 50×50 nm. Additionally, we observe associated fluctuations in the stray field of up to 3 mT.

5.5.1 Estimated spin qubit decay times due to charge noise

Next, we estimate the impact of these magnetic stray field fluctuations on the dephasing of electron spin qubits when they are placed within the stray field. Specifically, we

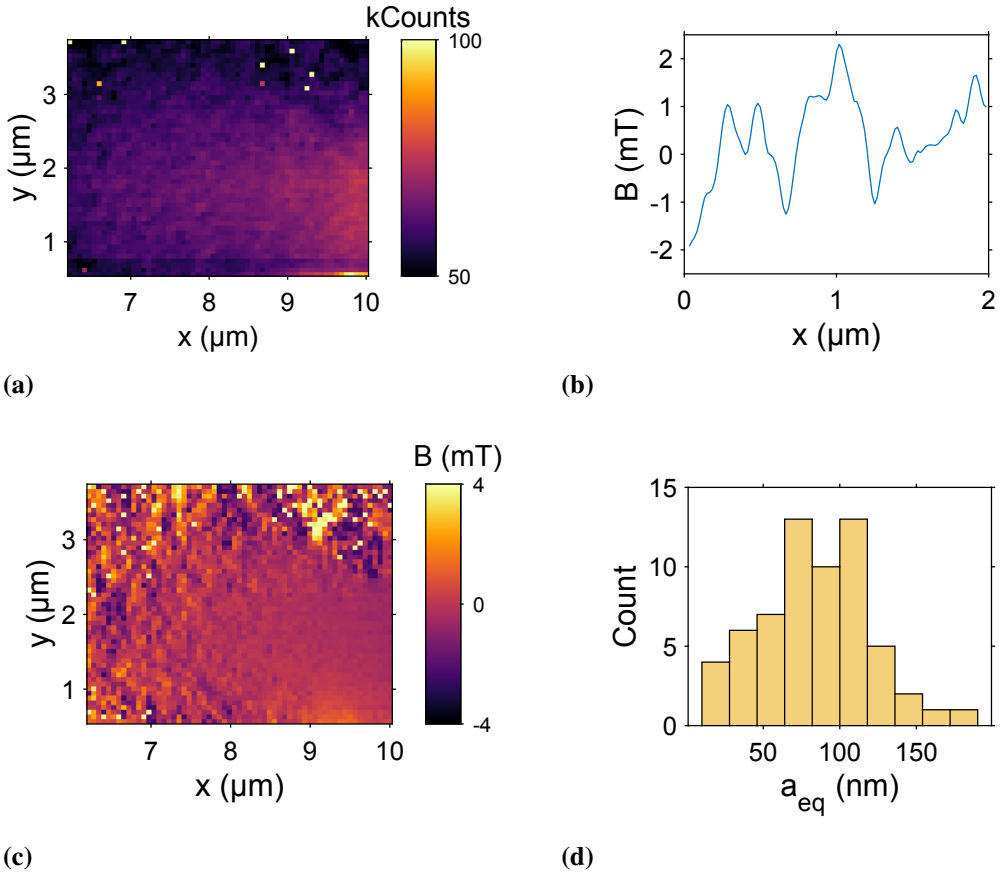

FIGURE 5.16 — Characterization of magnetic properties and grain size distribution. (a) Distribution of grain sizes within the marked region, illustrating changes in material composition at the upper left and right edges. (b) Variations in the magnetic field measured across several micrometers. (c) Magnetic image of the "halo", revealing granular composition. (d) Histogram depicting the distribution of grain sizes.

examine dephasing caused by spin qubit displacements within the "halo" stray field due to charge noise. In this context, typical root-mean-square (rms) displacement amplitudes of quantum dot (QD) electron spin qubits range from 1 to 10 pm along the x and y axes [94, 104]. Out-of-plane displacements are usually negligible for quantum well or metal-oxide-semiconductor (MOS) quantum dots, given the significantly larger confinement potential in this direction compared to the xy-plane. Given that the displacements are orders of magnitude smaller than the grain size of the "halo" stray field, we can limit our analysis to the first derivative at each point and disregard higher-order derivatives of the stray field. Taking the spin qubit quantization axis to be parallel to x, the stray field derivatives that are relevant for dephasing are therefore $\frac{dB_x}{dx}$ and $\frac{dB_x}{dy}$. Differentiating the scan in Fig.5.16(d) with respect to x and y, we observe that $\frac{dB_x}{dx}$ and $\frac{dB_x}{dy}$ are largest near the intended Co Hall bar deposit (top left and right corners, and slightly above the bottom left and right corners of Fig.5.16(d). However, at no point in the scan do these derivatives exceed 425 µT/nm. Using these derivatives of the stray field, we can estimate the inhomogeneous dephasing time T_2^* for a spin qubit located within the grainy stray field induced by the "halo". For each point (x,y) in the scan shown in Fig.5.16(d), we calculate T_2^* using:

$$T_2^* = \sum_i (2\pi\sqrt{2} \cdot \frac{\mu_B}{\hbar} \cdot \frac{dB_x}{di} \cdot \Delta i)^{-1}, \qquad i \in x, y \tag{5.10}$$

Here we use $\Delta x = \Delta y$ =10 pm, an electron spin Landé g-factor of 2, and we assume a quasi-static 1/f-like spectral density of charge noise[105]. Fig 5.17(b) shows the corresponding map of $T_2^*(x, y)$. We find that $T_2^*(x, y)$ decreases from >100 µs in the top corners of the scan, where almost no "halo" is present, to roughly 5 µs in the immediate proximity of the Co deposit, where the "halo" is most intense. Furthermore, we find that T_2^* exceeds 1 µs at every point in the scan. Note that the contours in the plot of Fig.5.17(b) have been obtained by smoothing the data. While these contours indicate the trend of decreasing T_2^* when approaching the Co deposit, the frainy pattern visible in the colorplot 5.17(b) originates from the disordered "halo" stray field, and hence, should not be ignored.

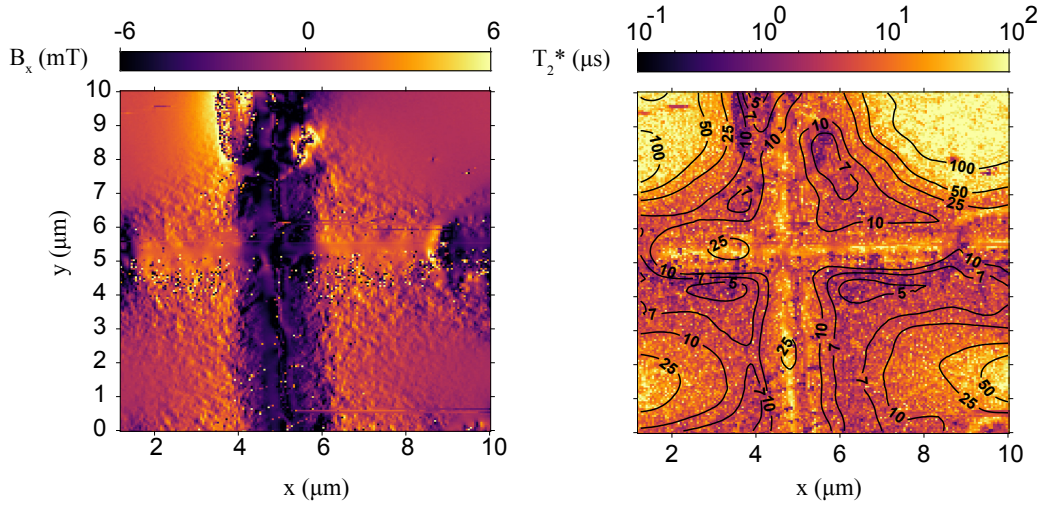

FIGURE 5.17 — Estimation of coherence maps for electron spin qubits near a magnet. (a) A contour map of the magnetic field component B_x. The plot reveals a complex magnetic landscape consisting of a central, saturated magnetic wire and a surrounding "halo" region. This halo is characterized by a locally varying magnetic field, which suggests the presence of magnetic nanoparticles. (b) A corresponding contour map of the electron spin qubit's T_2^* time, estimated using the magnetic field data from panel (a) and eq.5.10. The contours clearly show how the magnetic configuration impacts qubit coherence. The low T_2^* values in the high-field region and within the noisy halo indicate significant dephasing, while the higher T_2^* values in the outer regions point to a more uniform and quieter magnetic environment, highlighting the optimal "sweet spots" for qubit operation.

5.6 Outlook

5.6.1 Optimized geometry for a spin qubit device

Here we propose FEBID as an innovative fabrication technique of nanomagnets in a single-step, enabling high magnetic gradients. We emphasize that we have studied and estimated the effects of the magnetic noise on the spin qubit operation during the fabrication process, which increases the reliability of these magnets. Further, more advanced 3D geometries can be developed by employing FEBID to individually tune the resonance frequencies of each qubit.

5.6.2 Cryo - FEBID

Future research could leverage cryo-FEBID to pattern magnetic nanostructures on sensitive spin qubit devices. This technique, operating at cryogenic temperatures, offers advantages such as high growth rates and low electron charge doses, making it ideal for delicate applications.

The growth in FEBID is influenced by temperature-dependent processes like adsorption, desorption, diffusion, and dissociation of precursor molecules. Under cryogenic conditions, the precursor condenses into a nanometer-thick layer, and exposure to an electron beam followed by mild heating reveals the structure. Low temperatures improve precursor residence time and reduce charge damage.

Key advantages of cryo-FEBID include:

- Growth rates that are 100-1000 times faster than at room temperature.
- Significantly lower electron doses (approximately 10^4 times less) than required for room-temperature deposition, minimizing sample damage.

This makes Cryo-FEBID comparable to resist-based electron-beam lithography in terms of electron irradiation effects, with the added benefit of enhanced deposition speed.

5.6.3 3D nanoprinting with FEBID

As mentioned in the beginning, the ability to fabricate 3D magnetic nanostructures able to individually tune the resonance frequencies of spin qubits is an interesting feature we suggest to explore in future projects.

However, 3D nanoprinting holds potential beyond spin qubit applications. In the last decade there has been a significant effort made on the topic of three-dimensional printing of nano-objects using focused-electron-beam-deposition. Severals studies [106,

70, 107] have shown successful advancement of the FEBID 3D patterning software and confirmed its reliability in specific applications such as magnonics, spintronics, scanning probe microscopy, nanowire networks and curvilinear nanomagnetism. Some advantages of 3D nanoprinting is its ability to pattern three-dimensional magnetic nanostructures at resolutions comparable to the characteristic magnetic length scales. Thus, making 3D FEBID an appealing fabrication method for fundamental studies of complex 3D geometries, as well as opening a new field of study of nanomagnetizm in 3D. One of the applications where its usefulness has been particularly pronounced is in investigation of nanoscale double helixes, proven to host highly coupled textures [108, 109, 110]. They created magnetic double helices similar to double helix of DNA, that twist around one another, combining curvature, chirality and strong magnetic field interactions between the helices. Using X-ray imaging techniques, they discovered that the 3D structure of these magnetic helixes exhibits a different magnetization texture compared to the 2D structure. They found that pairs of walls between magnetic domains in neighboring helices were highly coupled, causing deformations that result in the rotating structure. These deformations create locally locked strong bonds, similar to base pairs in DNA. Recently, the software for 3D patterning has become publicly available [111], enabling its use in every laboratory equipped with a FEBID system.

These factors make this technique a promising candidate for constructing high-density 3D nanomagnets for quantum information processing and beyond.

6 Correlation of magnetic noise and stability of magnetic states in permalloy dome-shaped nanodots

The results in this chapter will be described in Žaper et al, Resolving the intrinsic magnetic texture of soft nanodots via scanning NV magnetometry, pre-print.

Magnetic force microscopy (MFM) previously revealed a remanent half-hedgehog state in permalloy nanodots [112]. To exclude that the stray field of the magnetic tip stabilized this magnetic configuration, we compare the MFM [113, 114], Kerr microscopy, and scanning nitrogen-vacancy magnetometry (SNVM) studies to resolve the magnetic state, where SNVM provides a crucial non-invasive measurement. MFM constitutes one of the most powerful magnetic imaging techniques at the nanoscale. Despite its remarkable lateral resolution and sensitivity, its working principle relying on the probe-sample interaction constitutes one of its main drawbacks when it comes to revealing magnetization textures of soft magnetic materials, as they are often affected by the stray field of the MFM probe. In this work, we add SNVM to determine the magnetization configuration present in such nanostructures in the absence of any probe stray fields acting on the sample. Imaging via SNVM reveals a remanent single-domain configuration of the nanodots, providing strong evidence that MFM probe stray fields nucleate the half-hedgehog configuration. In addition, we perform SNVM T_1 spin relaxation measurements to probe magnetic noise originating from the studied magnetic configurations. From our findings, we draw a direct correlation between the magnetic noise and their proximity to the phase boundary in the phase diagram, thereby indicating a new approach in studying spin texture stability in permalloy nanodots.

6.1 Motivation

In spintronics and neuromorphic computing applications, understanding the mechanisms that govern magnetism at the nanoscale is essential due to the large number of magnetic elements needed to efficiently transfer spins that encode information or form a memory block [115, 116, 117]. For example, in traditional memory technology, such as DRAM or flash, the size of a memory cell ranges from a few tens of nanometers to hundreds of nanometers. In spin-transfer torque memory (STT-RAM) or magnetoresistive RAM (MRAM), each memory cell contains a magnetic tunnel junction (MTJ) with the size of a few tens of nanometers [118, 119, 120]. As

technology continues to scale down to smaller dimensions, the search for magnetic materials confined to the nanometer range remains crucial. A type of material which has captured the attention of the research world in particular, are materials containing skyrmionic magnetic phases [121, 122]. Skyrmions are topologically protected magnetic structures, which means they are resilient to external perturbations. In addition to their robustness, they require minimal currents for manipulation, retain their state when power is removed, and can be operated at high speeds. The fact that they exist in nanometre-sized islands further enhances their potential for scaling in advanced memory aplications [123, 124]. Moreover, skyrmions have been observed in a diverse range of materials, including chiral magnets [125], thin films [126], and multilayers [123]. One can explore a parameter landscape where a combination of magnetostatic energy and exchange interaction is analyzed with the purpose of finding stable skyrmionic states. In addition, one must consider the effect of the confinement of the skyrmion which is related to magnetostatic energy and its anisotropy. Simulations have shown that a skyrmionic magnetic configuration could be stable in range of soft Py cylindrical and dome-shaped nanodots [127], thereby motivating further experimental research of these states. The MFM measurements have revealed the presence of skyrmionic states in sub-100 nm Py dots and suggest the existence of skyrmions in structures of the same diameter or larger. In this work, we further investigate 120 nm Py dots with SNVM. The measurements indicate absence of the half-skyrmion structure, revealing the stray field of the MFM tip may have interferred with the experimental observation in previous work. Instead, an in-plane state is observed, and further magnetic noise measurements suggest instability of the spin state for similar aspect ratio nanodots.

6.1.1 Magnetization configurations

Magnetization configurations describe the arrangement and direction of magnetic moments (individual spins), which are influenced by material geometry and boundary conditions. The spins in the nanomagnet align such that the total magnetic energy is minimized, resulting in a distinct magnetization pattern for the given internal and external conditions. Depending on the initial conditions, a variety of metastable states can be found in soft permalloy cylindrical and dome-shaped nanodots. In this subsection we describe the spin texture observed in the in-plane, vortex, half-hedgehog and quasi-skyrmion states. The in-plane state is characterized by a largely uniform distribution of magnetization, typically achieved by applying an external magnetic field along the plane of the permalloy nanodome. The spins start to deviate

from the in-plane distribution on the edges of the curvature of the nanodome, due to the influence of demagnetization fields or surface edge effects. This state minimizes the magnetostatic energy and the exchange energy without changing the core spin alignments as in the vortex state.

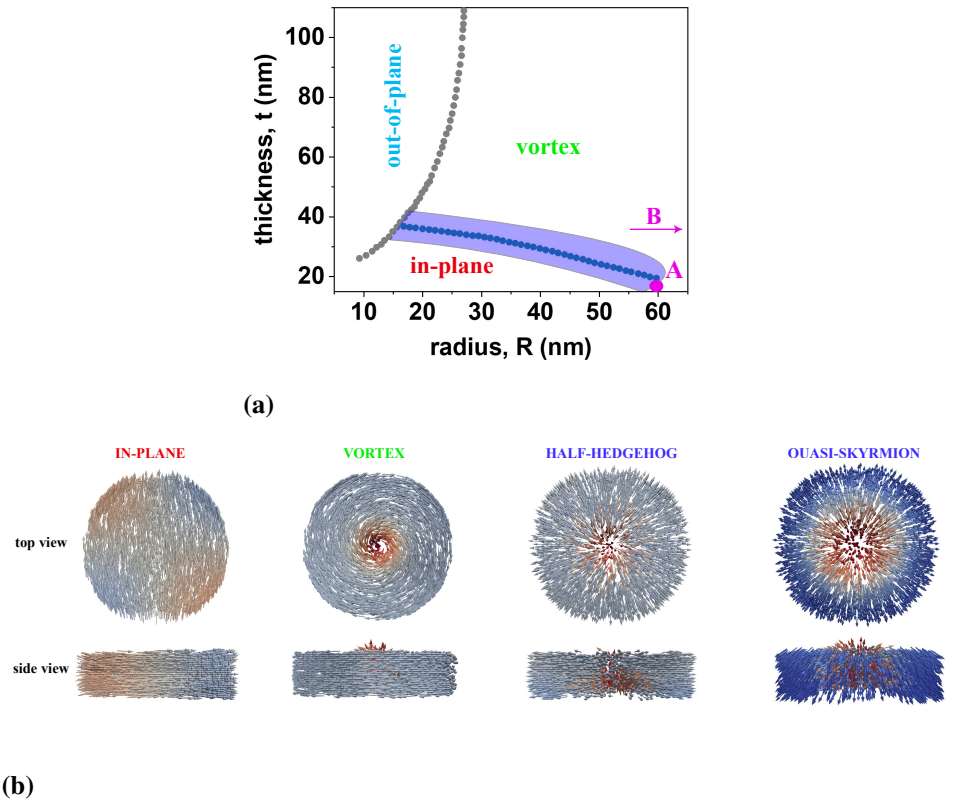

FIGURE 6.1 — Phase diagram of permalloy nanodisks. (a) Zero-field phase diagram of cylindrical permalloy nanodisks, with the areas corresponding to the expected magnetization configurations: in-plane, out-of-plane and vortex. The violet-shaded region indicates the transition zone between in-plane and vortex states, where various skyrmionic magnetization configurations are theoretically predicted to occur [127], though the precise boundaries of this region remain undefined. Sample A is located close to the lower boundary, while Sample B is within the region that corresponds to vortex configuration. (b) Predicted magnetization textures near the lower boundary as reported in the literature.[127], with each texture image highlighted by the corresponding color from the phase diagram.

In the vortex state, the spins are arranged in a circular or spiral fashion, confined to the basal plane of the nanodome structure as in Fig.6.1(b). This arrangement minimizes the magnetostatic energy, and thereby forms the magnetic ground state. In its center, one spin is pointing up or down, because of the minimization of the exchange energy at this point. Further away from the core, the magnetization lies predominantly in-plane. Spins can follow a counter-clockwise, or a clock-wise trend, depending on

the history and the nucleation of the vortex. This effect is commonly referred to as chirality of the state. Half-hedgehog state has a texture which appears as the spins are diverging from the center of the core. Similarly to the spines of a hedgehog, only in this case we are observing half of the sphere. In the center of the hedgehog, the magnetization is pointing out-of-plane, and closer to the edges, it changes the direction to in-plane. In the transition regions between, the magnetization changes radially, following the curvature of the nanodome.

The quasi-skyrmion has a magnetization texture that is pointing mostly out-of-plane, only at the edges the magnetization turns in-plane, while the transition region is larger compared to the half-hedgehog. Similarly to the half-hedgehog state, the spins are diverging from the center of the core.

6.1.2 Phase diagram

Within this work we study two samples: sample A with 120 nm diameter and 15 nm height, and sample B with 400 nm diameter and 20 nm height as shown in Appendix G. The magnetic phase diagram in Fig.6.1(a) shows that depending on the aspect ratio of the dots, we can observe the in-plane magnetization type for dots with small radius and there is a point where the magnetization transitions to the vortex and the quasi-skyrmion. The exact position of this point is not precisely defined, so research is needed to explore these grey areas. For dots with lower aspect ratio, they are likely found in the in-plane configuration, while for dots with larger thickness and an aspect ratio close to 1, they are typically found in the vortex configuration. Here we are investigating the Sample A, whose aspect ratio is in the in-plane region according to the phase diagram. Sample B is positioned inside the vortex region, and therefore can be used as a reference sample. We are interested in knowing the exact magnetization texture in Sample A because we could potentially leverage it for building nanostructures for spintronics. Moreover, the research on the permalloy dome-shaped nanodots has shown interesting analytical predictions confirmed by simulations, that near the boundary of the phase diagram, a quasi-skyrmion state can be found. Recently, a similar texture, half-hedgehog, was observed in the work of Berganza et al.[127] in dots with d = 70 nm. These states are found at the transition points of the phase diagram and they are particularly useful because of their topological charge equal to the vortex state (around 1/2), but these states occurs in smaller diameter dots. However, they require stabilization and reliability in repetition of the fabrication process in order to be fully leveraged as building blocks for spintronic devices. These states were first observed in an experimental study conducted using

MFM [112]. The observation motivated an in-depth analytical study and simulations of Py nanodiscs with 10 nm to 60 nm and with aspect ratios of 0.1 to 1, which confirmed their existence under specific stabilization conditions. Looking only at the phase diagram, we expect to find these dots either in the in-plane or the vortex state. However, one can stabilize them by using an external field, from where a half-skyrmion state is found. The study in this thesis suggests that this is the case, and the MFM technique has indeed interacted with the state such that it nucleated it.

Sample	Radius (nm)	Thickness (nm)
A	60	15
B	200	22

TABLE 6.1 — Dimensions of samples under investigation.

In summary, the magnetic phase diagram provides crucial insight into the magnetization configurations of permalloy nanodots as a function of their aspect ratio. Identifying the boundary states is especially valuable due to the unique properties they exhibit, and ongoing research continues to expand our understanding of the less-defined transitional regions. This knowledge is highly beneficial for material scientists and device engineers, enabling them to make informed design choices when utilizing permalloy in various technological applications.

6.2 MFM imaging: Vortex and Half-hedgehog configurations

The two distinct permalloy nanodot samples used in this study (Sample A and Sample B), prepared by e-beam lithography, were selected to investigate different magnetic regimes (dimensions detailed in a separate table, e.g., 6.1). According to typical phase diagrams for permalloy disks, *Sample A* is located close to the lower phase boundary, delimiting the in-plane and vortex magnetic configurations (Fig.6.1(a)). *Sample B*, having a larger diameter, is expected to exhibit a stable vortex configuration.

Preliminary characterization was performed using Magnetic Force Microscopy (MFM) imaging. Topographic and magnetic images (see 6.2(a)), together with their profiles (see Fig.6.2(b)), revealed two distinct behaviors. Sample A displayed a magnetic contrast (bright in the center and dark around the nanodisk), which is consistent with the half-hedgehog configuration reported in a previous publication by Berganza et al.[112]. This configuration was found to be reliably stabilized by the stray field of the MFM probe, regardless of the sample's magnetic history. Sample

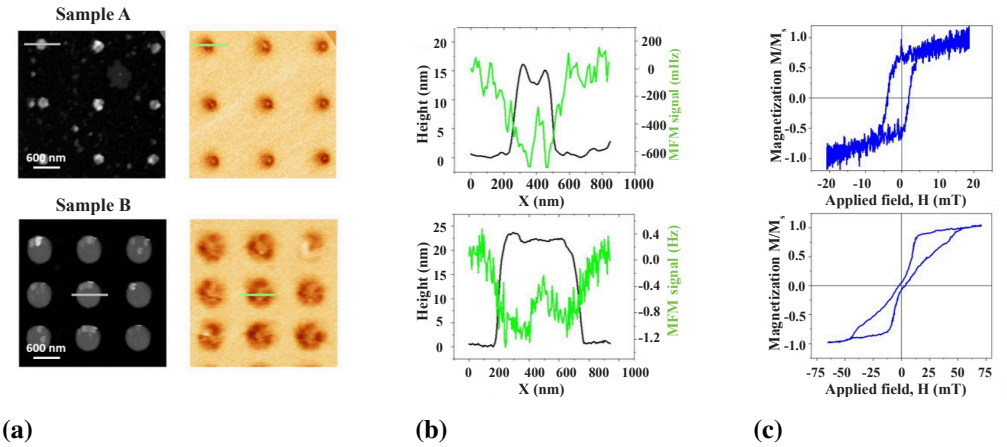

FIGURE 6.2 — MFM and MOKE measurements of Samples A and B.
(a) Topographic (left column) and magnetic signals from MFM measurements (right column) (b) Line profiles taken at locations indicated in (a). Green corresponds to MFM signal, black to topography. (c) Average hysteresis loops measured with Kerr-effect microscope. The field was applied in-plane.

B, instead, showed bright cores in most cases, although some radial contrast was present. Additionally, the magnetic configuration of Sample B was observed to be susceptible to modifications induced by the probe as the sample was scanned to a larger extent (evidenced by the sudden change of MFM contrast in the lower left nanodisk [128]). Kerr effect magnetometry was subsequently employed to elucidate the overall magnetization configurations and compare the reversal processes of both samples (see Fig.6.2(c)). The averaged hysteresis loops of several tens of nanodots provide indirect insight into the magnetic state. The squared-shaped loop obtained for Sample A, showing a magnetization reversal mediated by a single Barkhausen jump, is typically indicative of a single-domain configuration. While such curves often suggest coherent rotation or domain-wall propagation, the mild smoothness of the curve means the half-hedgehog configuration cannot be entirely discarded based on this measurement alone. For Sample B, the curve possessed the characteristic shape of a vortex configuration reversal, with zero remanence, two lobes, and a well-defined annihilation field value, as expected for these larger sizes [128].

6.3 Non-invasive imaging with NV magnetometry

6.3.1 Static Magnetic Field Maps

Revealing the remanent magnetic configuration of the studied magnetic nanodots can be challenging, as it requires truly non-invasive imaging. Unlike MFM, where the

tip's stray field can alter the sample's magnetic remanent configuration, SNVM enables optical detection of magnetic resonance without applying local magnetic fields, preserving the sample's native state even in soft magnetic nanostructures. Towards this aim, magnetic imaging experiments were conducted using a commercial SNVM (the room temperature ProteusQ setup from Qnami AG). It features a specialized diamond probe with a single NV center positioned at its apex (Qnami Quantilever MX), mounted on a quartz tuning fork-based atomic force microscope (AFM) operating in frequency modulation mode (FM-AFM). The NV-equipped probe is scanned across the surface of the nanodot arrays to acquire data, with the effective distance d_{NV} between the sample surface and the NV center (see Fig. 6.4(a)). The specific nanodots measured (Sample A and Sample B) have the dimensions detailed in Table 6.1 and were fabricated as described in Appendix G.

Fluorescence maps provide a 2D spatial image of the light intensity emitted by the NV centers, containing information related to both the NV centers and the local magnetic field distribution of the sample. Conversely, magnetic field maps—generated by sweeping the microwave frequency at each pixel—offer quantitative information about the magnetic stray field by detecting resonance shifts at each location caused by the Zeeman effect. We used a 200×200 pixel grid where one pixel size was 9.5 nm for Sample B and 26 nm for Sample A.

Prior to the measurements, a saturating 400 mT magnetic field in the out-of-plane direction was applied to both samples to leave them in the same magnetic state as during MFM characterization.

SNVM Characterization of Sample B We begin by measuring the reference Sample B. The fluorescence map shown in Fig. 6.3(a) exhibits rings around the structure, which may come from the convolution of the tip with the sample edge. The magnetic stray field image (Fig. 6.3(b)) is quite intriguing, as it captures emanating spins from the center of the nanodot in a geometry different than the previously measured textures with MFM on perfectly circular dots. Rather, it shows dark and bright contours, similar to the MFM observations in the study of elliptical Py dots by Okuno et al.[129]. Despite its complexity, Sample B shows spin configurations pointing outward from the center of the nanodot in a radial fashion, consistent with the MFM imaging results. In this remanent state, the cores of magnetic vortices are all oriented in the same direction, exhibiting a bright contrast (Fig. 3c in the original publication, or refer to Fig. 6.3(c)). From both techniques, the resulting magnetic maps are similar to results obtained in previous studies on soft nanodots with slightly

asymmetrical shape, where circulating magnetization arranges into in-plane domains generating charges that are detectable by MFM [129] [130, 131].

SNVM Characterization of Sample A We continue with the measurements of Sample A. The fluorescence signal variation of Sample A (Fig. Fig.6.4(b)) is partly related to topographic effects, showing stronger reduction at the lower edge, while the signal reduction in the central region is related to the magnetic field-induced quenching of the photoluminescence signal. In the magnetic field image (Fig.6.4(b)), we observe a consistent qualitative behavior of the magnetization across the Py nanodot array. The general behavior of the dots matches the outcomes of the micromagnetic simulations of an in-plane state, which is further discussed and explained in Appendix D and E. Further control measurements of the remanent field of Sample A are reported in the Appendix F.

In-Situ Field Sweep A measurement routine with in-situ magnetic fields is often employed not only to probe configurations along magnetization reversal curves, but also to gain insight into the full reversal process, which often reveals complex magnetization states [129, 130]. Before starting the measurements, the nanodots were subjected to a $-250\,\mathrm{mT}$ field in the in-plane direction. Subsequently, the nanodots were primarily magnetized in-plane along the x-direction. Sequential measurements on Sample A while in-situ sweeping the in-plane magnetic field strength were performed (Fig. 4). As seen in the contrast-reversal of the stray field map, the polarity of the permalloy magnets switches between $-3\,\mathrm{mT}$ and $2\,\mathrm{mT}$, reaffirming the switching field observed in the hysteresis measurement with Kerr magnetometry from Fig. 2c. Small bias fields cause their magnetization direction to switch along their easy axis, which confirms the dot's magnetic state and its bistable behavior. Magnetic fluctuations in the GHz range, which are known to reduce fluorescent signals, are discussed in detail later in the manuscript in Section 6.4.

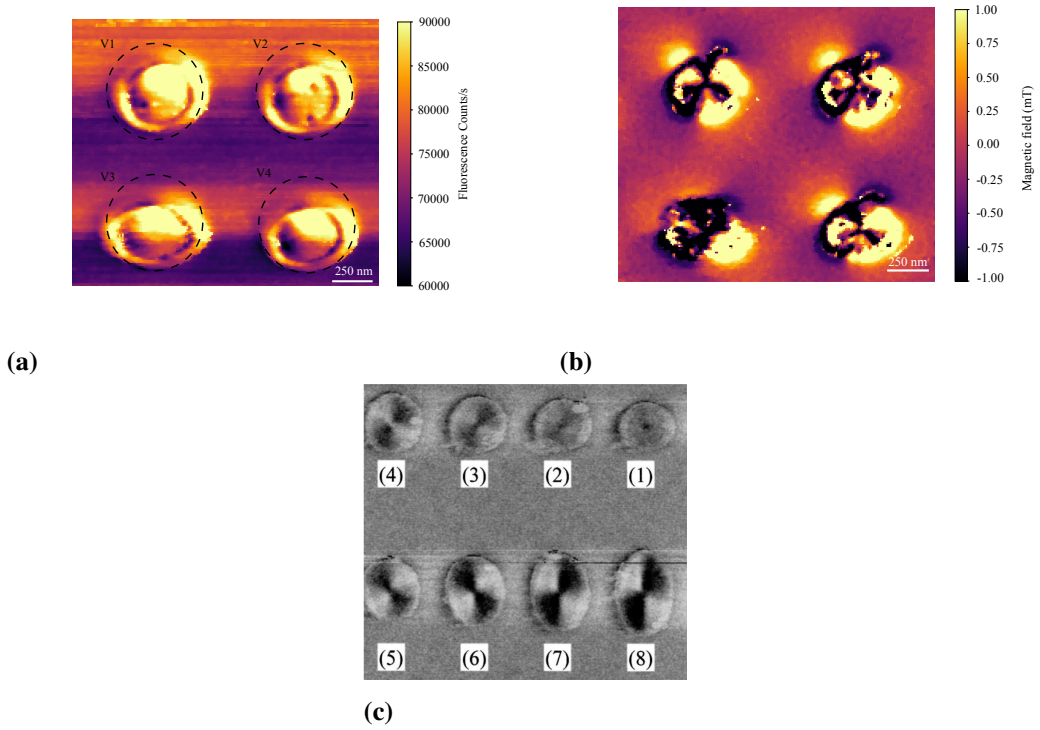

FIGURE 6.3 — SNVM measurements of Sample B. (a) Fluorescence map of Sample B. (b) Magnetic field map. Pixel size = 9.5 nm. Note: A median filter with a window of 3×3 was used. (c) Adapted from a MFM study of elliptical Py dots (different sample) where the width along the long-axis is increased. [129]. Similar pattern is observed using force sensing with nanowires [130, 131].

6.4 Spin Relaxometry: Probing Magnetic Configuration Stability

To investigate the intrinsic magnetic properties of the nanodots, we employed the SNVM technique to detect magnetic noise on the surface of Sample A and Sample B. T_1 relaxometry, which is the method exploited in this subsection, is based on the fact that the T_1 time of the NV center is sensitive to magnetic noise, with a typical spectral range in the GHz regime, specifically close to 2.87 GHz fluctuations. This approach relies on monitoring changes in the NV center's spin relaxation rate ($1/T_1$). Although relaxometry has been previously used to study non-collinear antiferromagnetic textures such as domain walls, spirals, and skyrmions [55], its application to permalloy disks provides new insights into soft magnetic materials. The perturbation measured here is limited to the magnetic noise on the sample surface, and the details of the measurements are described in Sections 3.2.6 and 3.2.7.

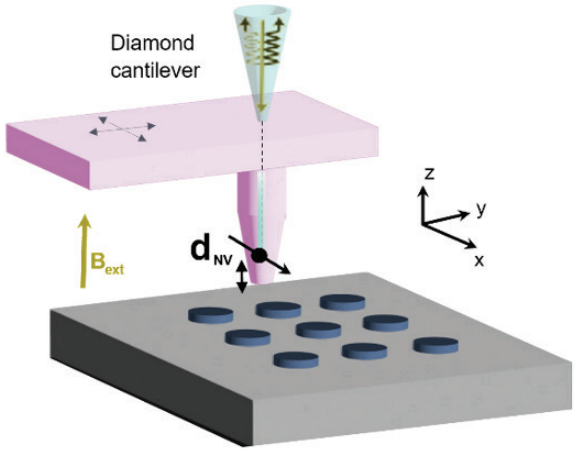

(a)

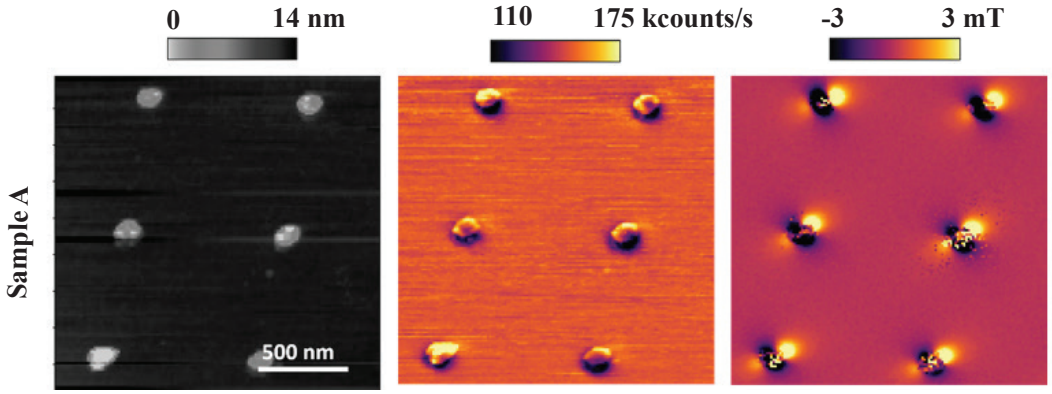

(b)

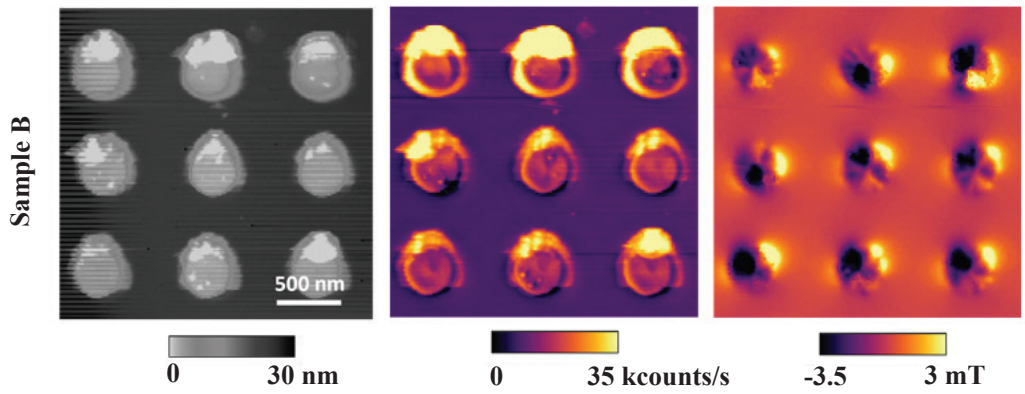

(c)

FIGURE 6.4 — SNVM measurement of Sample A and B. (a) Schematic of the measurement. (b) Fluorescence map of Sample A. (c) Magnetic field map. Pixel size: 26 nm. Note: A median filter with a window of 3×3 was used.

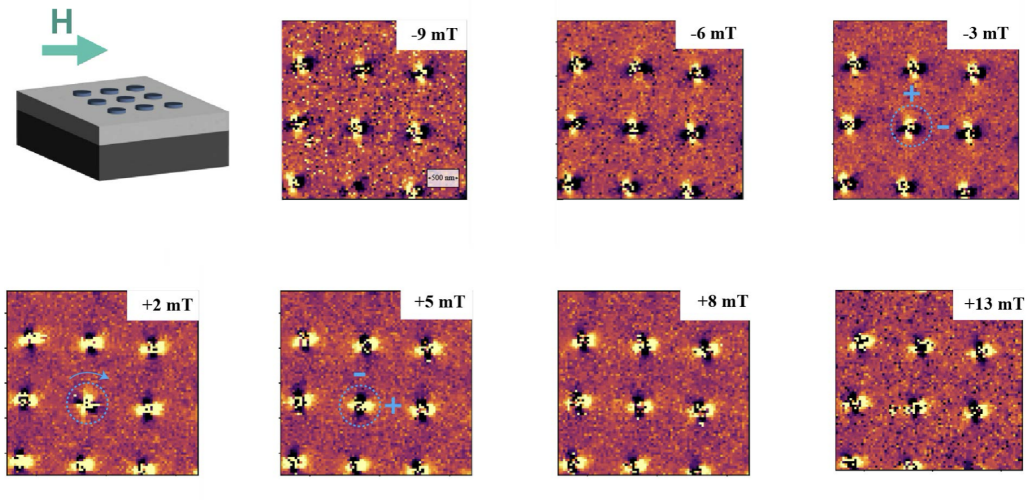

FIGURE 6.5 — Sequential measurements on Sample A, while in-situ sweeping the in-plane magnetic field strength. The field was applied in plane at -9 mT, -6 mT, -3 mT, 2 mT, 5 mT, 8 mT and 13mT. As seen in the contrast-reversal of the stray field map, he polarity of the permalloy magnets switches between -3 mT and 2 mT, reaffirming the switching field observed in the hysteresis measurement with MFM from Fig.2c.

6.4.1 T_1 Relaxation Mechanism and Measurement Protocol

Under continuous green laser illumination, the photoluminescence (PL) intensity of the NV center reflects the steady-state populations of the spin states, determined by the competition between the natural spin relaxation rate, $\Gamma_1 = 1/(2T_1)$, and the optical spin pumping rate, Γ_p, which depends on the laser power [55, 132]. Under typical conditions where $\Gamma_1 \ll \Gamma_p$, NV spins are efficiently polarized into the bright $m_s = 0$ state, producing a strong PL signal. When magnetic noise increases Γ_1 such that it approaches Γ_p, the polarization is reduced, and the PL signal decreases. Therefore, variations in PL provide a direct optical readout of local magnetic noise, as illustrated in the schematic diagram in Fig.6.6(a).

To quantify the magnetic noise on the sample surface, we employed the iso-T_1 measurement protocol (described in 3.2.7). This involves using a laser pulse sequence with a set evolution time, typically 1 µs, to calculate the T_1 time. The resulting iso-T_1 maps represent spatially dependent T_1 relaxation times acquired across the sample surface. By dividing each point's T_1 time by the maximum T_1 time in the scan, this measurement provides spatial and quantitative information of the magnetic noise, normalized by the intrinsic T_1 time of the tip.

Distance-dependent T_1 measurements were also performed to confirm the noise origin. We lifted the cantilever from a starting distance of 10 nm up to 100 nm, measuring

the T_1 time of the NV center at heights spaced by 10 nm. As shown in Fig.6.6(c), we observe a clear increase in the T_1 time with height, confirming that the noise originates from the intrinsic magnetic state and demonstrating the presence of a magnetic perturbation in the GHz range whose influence strengthens the closer we are to the sample surface.

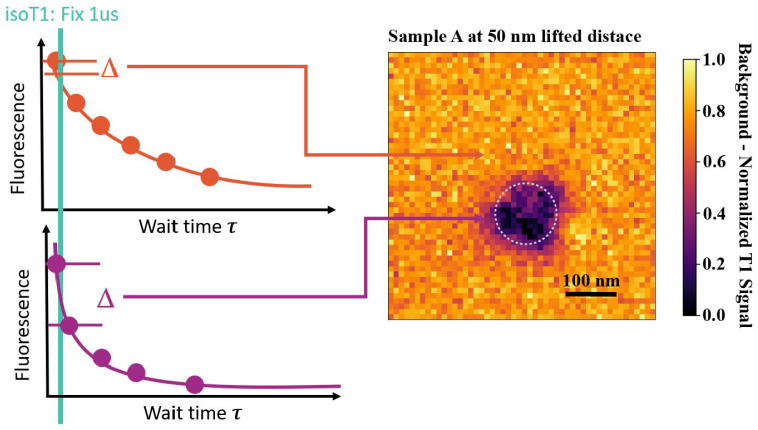

(a)

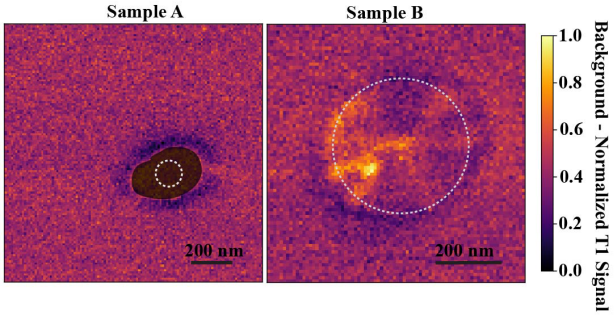

(b)

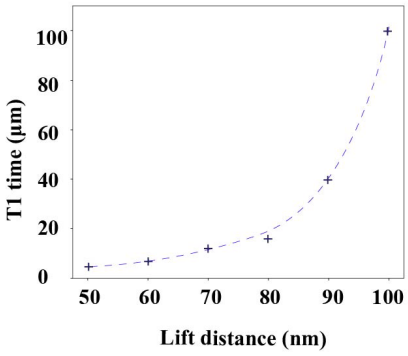

(c)

FIGURE 6.6 — T1 relaxometry. (a) Schematic diagram of T1 relaxation imaging (left), Sample A imaged at lifted distance of 50 nm with iso-T_1 technique. Data taken at 0 T. (b) iso-T_1 measurements of Samples A and B. Comparison of iso-T_1 maps for Samples A and Sample B, measured at a fixed evolution time of 1 µs (See Supporting Information 4) with the same diamond tip. The red dashed line represents the physical sample boundaries. Data taken at 0 T. (c) T1 time dependence with probe-sample lift distance showing an exponential trend (dashed line) in Sample A.

6.4.2 Comparison of iso-T_1 Maps and Interpretation

Fig.6.6(b) presents the iso-T_1 maps for Samples A and B. The two maps appear distinctly different. Sample A, which is situated near the phase boundary between uniform (in-plane) and vortex states, exhibits significantly elevated magnetic noise, particularly near its edges. The map shows very strong noise in this area where the NV center cannot be initialized properly. The bright spots observed indicate extremely strong local GHz fluctuations, which hinder the initial optical polarization and thereby prevent a reliable T_1 measurement, similar to effects seen in the work by Finco et al.[55].

Conversely, the more stable vortex configuration of Sample B exhibits less magnetic noise overall, with only minor areas of enhanced T_1 relaxation rates. The observed magnetic noise in Sample B includes contributions from GHz-range vortex precession, thermally-driven dynamics, and defect-related magnetic fluctuations [133, 134, 135, 136, 137]. We suspect the localized spots of enhanced noise are related to the vortex state cores, which attain spins that precess in the GHz regime in a circularly symmetric way (similar in [138]), interacting with the NV tip.

The observed difference confirms that proximity to the phase boundary amplifies these instabilities. Sample A, situated near the transition between uniform and vortex states, exhibits more magnetic noise compared to the vortex state Sample B. This increased noise is a direct consequence of the phase transition near the boundary, which destabilizes the magnetic state, leading to greater instability and higher levels of GHz magnetic noise.

6.5 Conclusion and Outlook

Magnetic imaging of soft magnetic nanostructures, relevant for advanced technological applications like spintronics and neuromorphic computing, presents substantial challenges. While advanced imaging techniques, such as X-ray circular dichroism or Electron Holography, still struggle to resolve sub-100 nm spin textures, Magnetic Force Microscopy (MFM) offers sufficient lateral resolution and the capability to measure with in-situ applied fields up to 2 T, enabled by highly coercive MFM tips specifically designed for high-field measurements. However, MFM relies on the interaction between a magnetic probe and the sample, which complicates the observation of pristine magnetic configurations in soft magnetic materials. Conversely, Scanning Nitrogen-Vacancy Magnetometry (SNVM) relies on optically detected magnetic resonance (ODMR) of nitrogen-vacancy centers in diamond, enabling magnetic field

sensing through spin-dependent fluorescence without physical interaction with the sample, thereby ensuring a non-invasive measurement approach.

In this study, we compared the outcomes of these distinct imaging techniques—MFM and SNVM—to measure the magnetic configurations of soft permalloy nanodots that pose the above-mentioned challenges. Our findings highlight the significant influence of the MFM probe's stray field on the observed remanent magnetic textures in $\sim$ 100 nm diameter nanodots, where the MFM nucleates a half-hedgehog spin texture (a half-skyrmion state). In contrast, SNVM measurements (supported by micromagnetic simulations) reveal a pristine single-domain in-plane configuration. This discrepancy is not observed in nanodots of bigger diameter, where a vortex state is suggested by Kerr effect measurements and confirmed by SNVM imaging. Further spin relaxometry characterization, which probes the magnetic noise on the sample surface, suggested a greater instability of the magnetic configuration for the sample geometry closer to the phase boundary between the magnetic vortex and in-plane states, confirming the high likelihood of magnetic state interference by the MFM tip.

In conclusion, SNVM proved to be a powerful and essential tool for accurately determining the intrinsic magnetic configurations within soft magnetic nanostructures, particularly those that present imaging difficulties. The study's findings have important implications for the development of spintronic devices, where precise control of spin textures is crucial, and strongly suggest the need for non-invasive techniques when investigating magnetic states close to phase boundaries.

6.5.1 Future Work

Looking ahead, we suggest a systematical approach for further exploration. The 70 nm diameter nanodot, which showed the presence of a half-skyrmion state with the MFM tip, could be measured with the SNVM after removing the MFM tip to confirm its pristine state. Further, we suggest fabricating nanodots with varying diameters close to the boundary in the phase diagram and subsequently performing a Full-B measurement combined with T_1 relaxometry. Such an approach, which could be performed efficiently on a single array-based chip, will allow for a comprehensive understanding of the behavior of soft permalloy dome-shaped nanodots close to the phase boundary, where there is a strong likelihood of finding skyrmionic states. This exploration will shed light on the exact fabrication parameters which lead to these states, which could be potentially leveraged for building next-generation spintronic or neuromorphic devices.

7 Conclusion

This thesis investigates the fabrication, characterization and application of nanomagnets for quantum computing and data storage in the context of growing number of datasets and the needs of modern technologies. Specifically, it aims to investigate how innovative techniques can be used to design and characterize nanomagnets for spin qubit control, thereby paving the way for enhanced performance in quantum computing. Additionally, this research investigates how nanomagnets can be incorporated into phononic membranes for studying the fundamental physics of spin-mechanical interactions. It seeks to unveil promising magnetization textures in nanostructured materials that could lead to advancements in memory storage, spintronics, and the development of neuromorphic systems.

We successfully applied Focused Electron Beam Induced Deposition (FEBID) in our laboratory to develop nanomagnets, laying a solid foundation for future research in this area. We achieved a cobalt (Co) content of nearly 90%, which resulted in high magnetic gradients created through a direct nano-patterning technique in a single step. Furthermore, we explored the physics of focused electron beam interactions by utilizing a rectangular pattern on a thin silicon nitride membrane. This approach allowed us to deposit a circular magnetic dot on a phononic membrane, establishing the groundwork for potential magnetic coupling between the membrane and the NV qubit. Additionally, we clearly unveiled the actual state of a permalloy nanodot using Scanning NV Magnetometry (SNVM), providing valuable insights into its magnetic properties. These findings not only contribute to the understanding of spin-mechanical interactions but also pave the way for future developments in quantum computing, memory storage, spintronics, and the integration of neuromorphic systems.

The work on nanomagnets for spin qubit control adds a valuable perspective to the existing research, offering an innovative fabrication solution. This implies the possibility of leveraging FEBID as a direct single-step technique for building arrays of nanomagnets on the surface of a spin qubit chip with the ability of individual tuning of the resonance frequencies. The fabrication of nanometric magnetic dots on phononic membranes deposited at the defect position, expand the possibilities for envisioning future experiments for spin-mechanics. Further, the employment of SNVM to uncover in-plane state of the permalloy magnetic dots, testifies to its relevance for imaging magnetic textures on the nanomatre scale, thereby opening the possibility for future studies of magnetic textures that could be particularly useful in many emerging applications.

We acknowledge that Focused Electron Beam Induced Deposition (FEBID) can introduce a significant level of impurity incorporation. We believe this is due to vacuum levels in our system that could be improved. Additionally, electron-beam lithography currently yields comparably high Co and FeCo concentrations and effectively integrates into the spin qubit fabrication process. It remains uncertain whether FEBID will prove to be a more suitable option for future applications, and this question warrants further investigation in actual spin qubit devices. Notably, we have not yet conducted Electron Dipole Spin Resonance (EDSR) experiments on real qubit devices, which is an essential step for validating the efficacy of FEBID in this context. The fabrication of cobalt nanodots on silicon nitride membranes could significantly affect the quality factor of the membranes. Therefore, it is crucial to verify whether any resulting decrease in the Q factor remains low enough to facilitate spin-mechanics experiments.

For future research, we recommend exploring the potential of 3D nanopatterning using FEBID, with a focus on deposition at lower temperatures. This approach would offer an additional degree of freedom for optimizing magnetic gradients at the nanoscale. Moreover, low-temperature deposition could reduce the accumulation of charge during the process and significantly minimize the presence of unwanted material around the deposited structures, thereby improving the overall precision and quality of the nanomagnets.

While we may not yet have full control over atoms one by one, we are steadily approaching this goal, marking a significant step forward in nanoscience.

Appendix A

A Annealing

Following the introduction to the post-growth techniques from Section 3.1.7, we also conducted an annealing study to explore its effects on the final properties of the structures. Further details regarding the annealing study can be found here.

TABLE A.1 — Statistical description of a Co FEBID nanowire before and after annealing at 600 °C and 100 min.

Dep. Param.	Annealed	Co-content [at %]	C-content [at %]	O-content [at %]
5 kV 100 pA	no	87.04 ± 1.7	10.2 ± 1.6	1.2 ± 0.3
5 kV 100 pA	yes	90.43 ± 1.2	7.63 ± 1.2	0.7 ± 0.2
10 kV 3.2 nA	no	88.44 ± 1.1	9.83 ± 1.1	0.61 ± 0.2
10 kV 3.2 nA	yes	89.38 ± 1.6	7.85 ± 1.3	1.02 ± 0.2

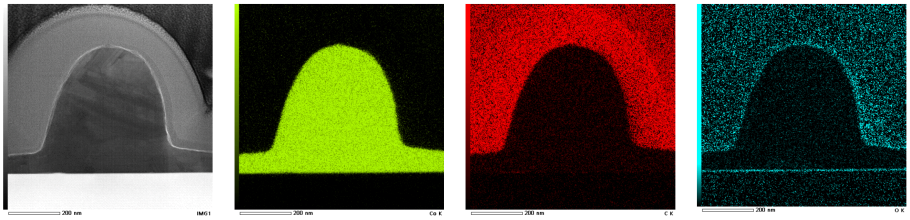

(a)

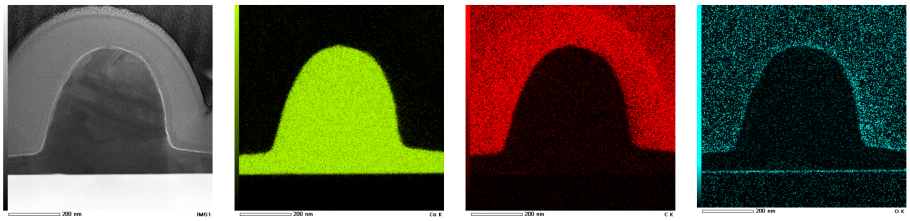

(b)

FIGURE A.1 — (a) Reference sample grown at 10 kV and 3.2 nA. (b) Annealed sample grown at 10 kV and 3.2 nA.

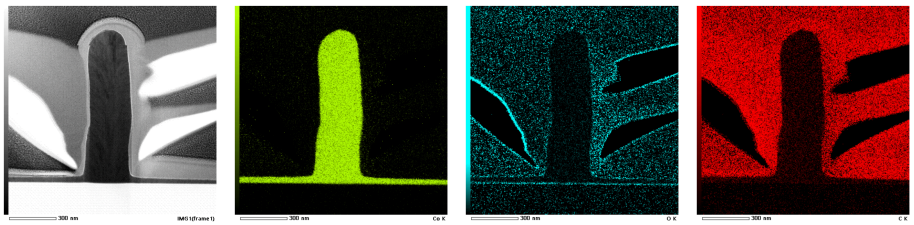

(a)

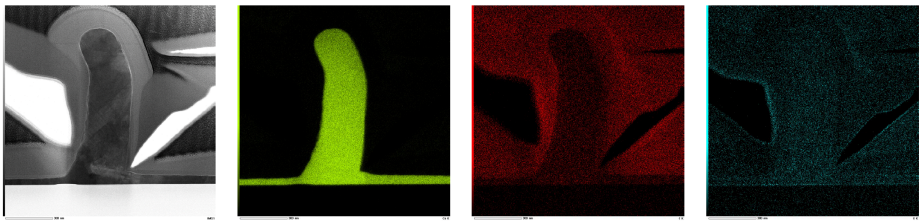

(b)

FIGURE A.2 — (a) Reference sample grown at 10 kV and 3.2 nA. (b) Annealed sample grown at 5 kV and 100 pA.

Appendix B

B Argon milling

As demonstrated in [139], substantial reduction of residual ”halo” can be removed by means of Ar+ milling.

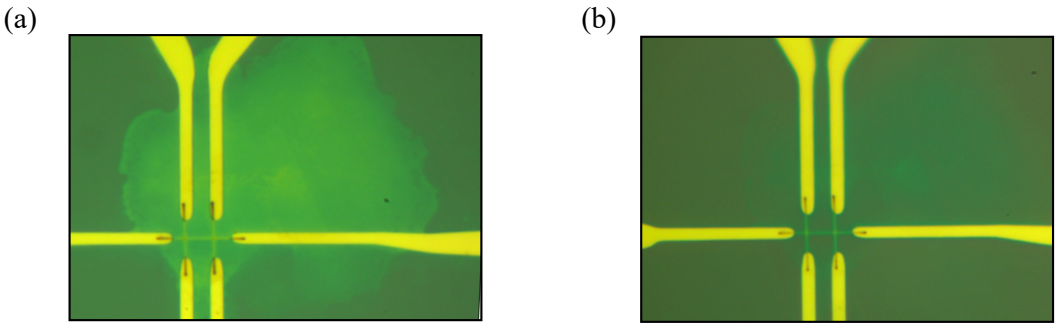

Figure B.1 — Argont milling of FEBID Hall bars. (a) Optical micrograph of Co Hall bar structure fabricated through FEBID. A large halo effect is visible as a cloudy stain surrounding the structure. The Co Hall bar is contacted by Ti/Pd contacts. (b) Optical micrograph after Ar ion milling, indicating a significant reduction of the halo.

Appendix C

C Reconstruction NV tip

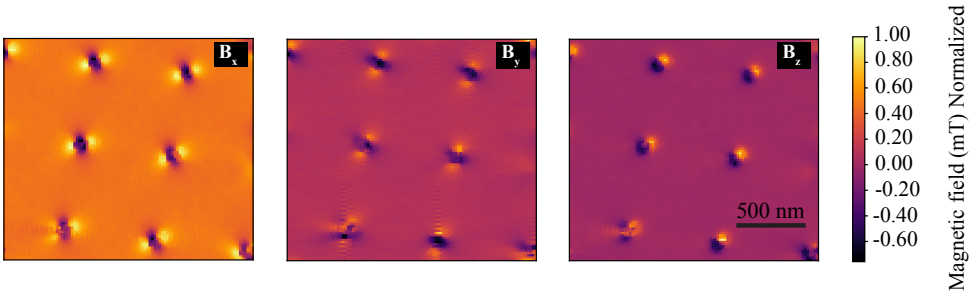

Figure C.1 — Reconstruction of the B_{NV} field into its B_x, B_y, and B_z components. This figure presents the reconstructed magnetic field, illustrating its decomposition into the individual components B_x, B_y, and B_z. The reconstruction algorithm was inspired by [51].

Appendix D

D Comparison experimental data and simulated Bnv field of in-plane and vortex state initial magnetization

The magnetization configurations and the resulting stray field of the cylindrical permalloy nanodots (nanodiscs) were modeled using the micromagnetics software Mumax3. Typical parameters for permalloy were chosen: exchange stiffness A_{ex} = 11 pJ/m and saturation magnetization M_{sat} of 800 kA/m. A mesh discretization (cell size) of 1 nm^3 was used. The nanodiscs were modeled in cylindrical geometry with a height corresponding to the measured AFM height of 15 nm and a diameter of 120 nm (radius r = 60 nm). The damping constant was set to $\alpha = 0.01$.

The simulation parameters were chosen to facilitate a fair comparison with the experimental Scanning Nitrogen-Vacancy Magnetometry (SNVM) data of Sample A (Fig. S2a), which showed a dipole with its magnetization axis pointing at a 45° tilt in the xy plane. We set the simulation under an external magnetic field B_{ext} = 200 mT to match the experimental conditions. The field components were calculated using the standard definition of spherical coordinates, with a polar angle $\theta = 90°$ and an azimuthal angle $\phi = 45°$. This specific angular selection was chosen to correspond to the applied field direction in the magnetic images from Section 5.4. The Cartesian components of the external magnetic field are defined as:

$$h_x = \cos\left(\frac{\phi \cdot \pi}{180}\right) \cdot \sin\left(\frac{\theta \cdot \pi}{180}\right) \tag{D.1}$$

$$h_y = \sin\left(\frac{\phi \cdot \pi}{180}\right) \cdot \sin\left(\frac{\theta \cdot \pi}{180}\right) \tag{D.2}$$

$$h_z = \cos\left(\frac{\theta \cdot \pi}{180}\right) \tag{D.3}$$

The revealed magnetization texture , which corresponds to the in-plane state, explains the experimental observation in Section 5.4.1. The best match between the simulation and the experimental data was achieved for an NV height of 50 nm, a polar angle of 54.7° and an azimuthal angle of 45° under the applied field of 200 mT, as detailed in the caption of Fig. S2b. Repeating the simulation for both initialized vortex and

in-plane magnetization yielded a similar dipole state (Fig. S2b), consistent with the experimental data.

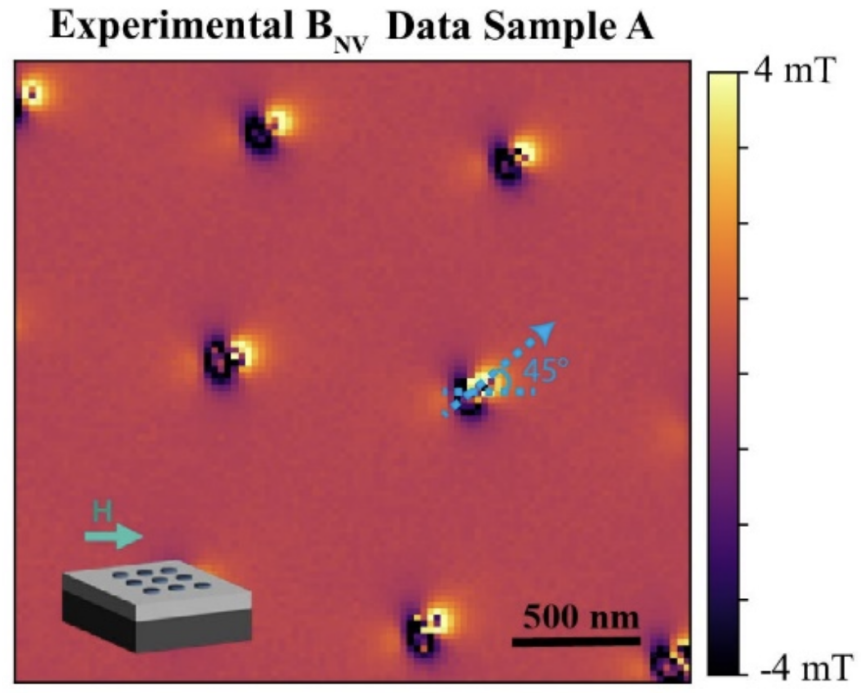

(a)

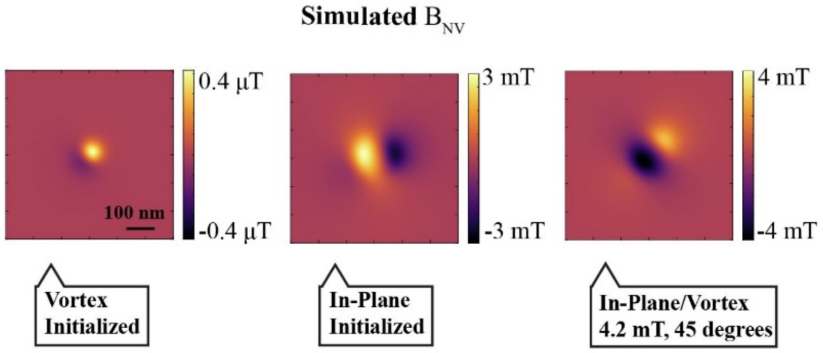

(b)

FIGURE D.1 — Comparison experimental data and simulations of magnetic field. (a) Experimental data of the measured B_{NV} field of Sample A. (b) Micromagnetic simulations showing: LEFT - the B_{NV} of a vortex state; MIDDLE - in-plane dot initialized by a -200 mT field; RIGHT - both in-plane and vortex states showing the same magnetization at simulated 4.2 mT and a 45° tilted field. In all simulated panels, we used an NV height of 50 nm, an azimuthal angle (ϕ) of 54.7°, and a polar angle (θ) of 45°.

Appendix E

E Possible magnetic configurations and corresponding stray field components

Other spin textures potentially hosted by magnetic nanodots are considered and their corresponding stray field components at a representative SNVM sensing distance, 40nm from the nanodot surface, are calculated to aid in the interpretation of the experimental results. The calculated stray fields for the considered configurations: half hedgehog and vortex—do not align with the experimental results, supporting the hypothesis that the magnetic configuration is single domain.

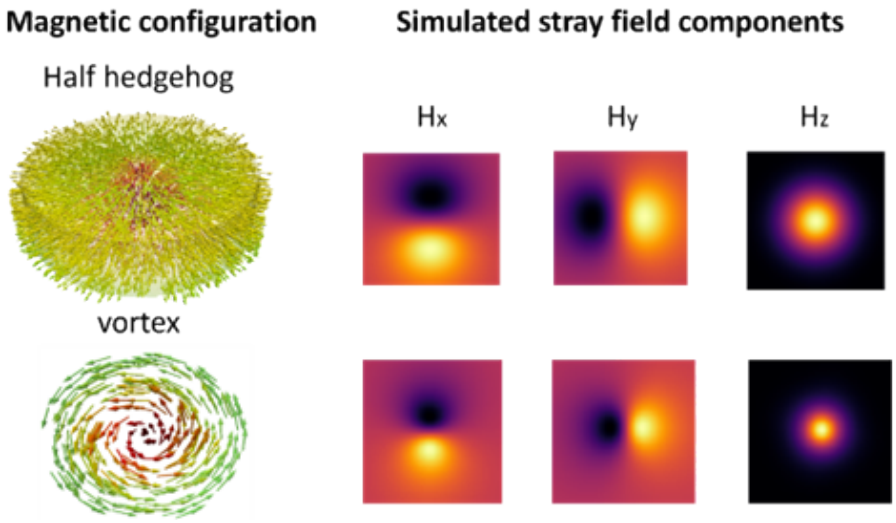

FIGURE E.1 — Half hedgehog vs vortex. Magnetic configurations are shown on the left and their corresponding calculated stray field components on the right.

Appendix F

F SNVM measurements of remanent fields

To verify the remanent magnetization without any bias field in the setup, we apply a large out-of-plane field of a hand magnet and measure the nanodots assuring there is no field. Since the nanodots are magnetically very soft we expect to observe the magnetization pointing randomly across the array under this condition. We note the random direction is notable, however, not consistent along the array, revealing multiple dots show a common magnetization direction. The reason for this is the fact that while using a hand magnet, any lateral movement may give rise to small in-plane fields, sufficient to produce such a magnetization pattern.

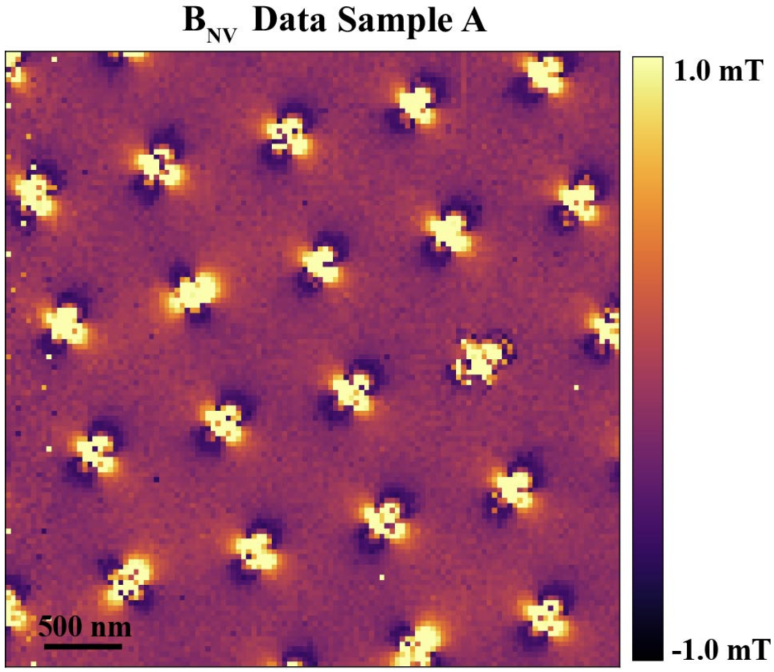

FIGURE F.1 — Remanent state of an array of nanodots. Bnv of nanodots arrays after out-of-plane field was applied, measured in their remanent state.

Appendix G

G Sample fabrication

For the study presented in Chapter 6, two distinct samples were prepared by e-beam lithography as detailed in the following. The samples were fabricated using e-beam lithography in a JEOL JBX-5500ZD system working at 50 keV of energy and 100 pA of current. Initially, a double-layer photoresist was spin-coated on a Silicon substrate at 2000 rpm and then cured in a hot-plate for 2 minutes at 150 ºC temperature. For the lithographic process, the samples were exposed with 200 μC/cm^2 dose. The photoresist was developed by 2 minutes immersion in MIBK:IPA solution. Permalloy $Ni_{80}Fe_{20}$ was subsequently evaporated at a 0.55 Å/s rate at 1e-6 mbar of pressure and the remaining PMMA layer was lifted-off by sonication in acetone for 15 minutes.

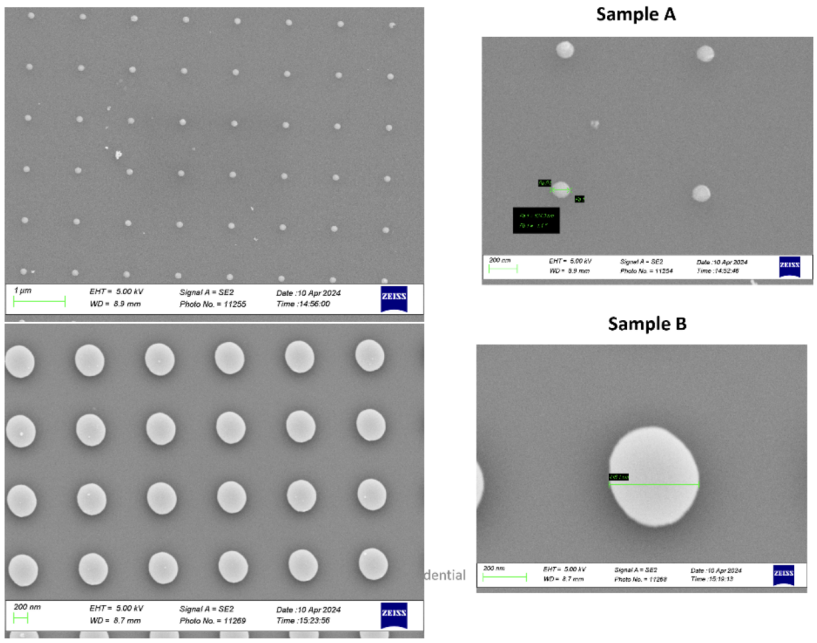

Figure G.1 — SEM images of Sample A and B.

Bibliography

[1] R. Feynman. "There's plenty of room at the bottom." In: *Resonance: Journal of Science Education* 16.9 (2011). URL: http://calteches.library.caltech.edu/47/2/1960Bottom.pdf.

[2] C. Toumey. "Reading Feynman Into Nanotechnology: A Text for a New Science." In: *Techne: Research in Philosophy & Technology* 12.3 (2008). URL: http://litsciarts.org/slsa08/slsa08-650.pdf.

[3] A.P. Guimarães. *Principles of nanomagnetism*. Vol. 7. Springer, 2009. DOI: https://doi.org/10.1007/978-3-319-59409-5. URL: https://link.springer.com/book/10.1007/978-3-319-59409-5.

[4] G.M. Whitesides. "The'right'size in nanobiotechnology." In: *Nature biotechnology* 21.10 (2003). DOI: https://doi.org/10.1038/nbt872.

[5] Y. Taur and T.H. Ning. *Fundamentals of modern VLSI devices*. Cambridge university press, 2021. DOI: https://doi.org/10.1017/9781108847087.

[6] F. Jazaeri et al. "A review on quantum computing: From qubits to front-end electronics and cryogenic MOSFET physics." In: *2019 MIXDES-26th International Conference" Mixed Design of Integrated Circuits and Systems"*. IEEE. 2019. URL: https://ieeexplore.ieee.org/document/8787164.

[7] I. L. Medintz et al. "Quantum dot bioconjugates for imaging, labelling and sensing." In: *Nature Materials* 4.4 (2005). DOI: https://doi.org/10.1038/nmat1390.

[8] F.T. Duvan et al. "Graphene-based microelectrodes with bidirectional functionality for next-generation retinal electronic interfaces." In: *Nanoscale Horizons* (2024). DOI: https://pubs.rsc.org/en/content/articlehtml/2024/nh/d4nh00282b.

[9] C. Eckel et al. "Nanoscopic electrolyte-gated vertical organic transistors with low operation voltage and five orders of magnitude switching range for neuromorphic systems." In: *Nano Letters* 22.3 (2022). DOI: https://doi.org/10.1021/acs.nanolett.1c03832.

[10] E. Berganza. "A study of complex magnetic configurations using magnetic force microscopy." In: (2018). URL: https://research.science.eus/documentos/614a9ce37035e612ed62ebb7?lang=en.

[11] J. M. D. Coey. *Magnetism and Magnetic Materials*. Cambridge University Press, 2010. DOI: https://doi.org/10.1017/CBO9780511845000.

[12] T. Ihn. *Semiconductor Nanostructures: Quantum states and electronic transport*. OUP Oxford, 2009. URL: https://global.oup.com/academic/product/semiconductor-nanostructures-9780199534425?cc=us&lang=en&.

[13] RP Cowburn. "Magnetic nanodots for device applications." In: *Journal of magnetism and magnetic materials* 242 (2002). DOI: https://doi.org/10.1016/S0304-8853(01)01086-1.

[14] H. Vigo-Cotrina et al. "Magnetic interactions in vortex-state nanodisk arrays characterized by gradient magnetic vortex echo." In: *Journal of Applied Physics* 135.8 (2024). DOI: https://doi.org/10.1063/5.0194332.

[15] J. Rial and M.P. Proenca. "A novel design of a 3D racetrack memory based on functional segments in cylindrical nanowire arrays." In: *Nanomaterials* 10.12 (2020). DOI: https://doi.org/10.3390/nano10122403.

[16] V.J. Borràs, R. Carpenter, and L. Žaper et al. "A quantum sensing metrology for magnetic memories." In: *npj Spintronics* 2.1 (2024). DOI: https://doi.org/10.1038/s44306-024-00016-5.

[17] M.V. Puydinger dos Santos et al. "Annealed cobalt–carbon nanocomposites for room-temperature spintronic applications." In: *ACS Applied Nano Materials* 3.7 (2020). DOI: https://doi.org/10.1021/acsanm.0c01497.

[18] TEDx Talks. *Green computing using next-generation nanotechnology — Amalio Fernández-Pacheco*. 2017. URL: https://www.youtube.com/watch?v=bMWMFcDBUu4.

[19] A. Weitzer et al. "Expanding FEBID-Based 3D-Nanoprinting toward Closed High-Fidelity Nanoarchitectures." In: *ACS Applied Electronic Materials* 4.2 (2022). DOI: https://doi.org/10.1021/acsaelm.1c01133.

[20] A. Salvador-Porroche et al. "Highly-efficient growth of cobalt nanostructures using focused ion beam induced deposition under cryogenic conditions: application to electrical contacts on graphene, magnetism and hard masking." In: *Nanoscale Advances* 3.19 (2021). URL: https://pubs.rsc.org/en/content/articlehtml/2021/na/d1na00580d.

[21] J.A. Fernández-Roldán. "Micromagnetism of cylindrical nanowires with compositional and geometric modulations." In: (2019). URL: http://hdl.handle.net/10486/689233.

[22] W.F. Brown Jr. "Micromagnetics, domains, and resonance." In: *Journal of Applied Physics* 30.4 (1959). DOI: https://doi.org/10.1063/1.2185970.

[23] R. Hanson et al. "Spins in few-electron quantum dots." In: *Reviews of Modern Physics* 79.4 (2007). DOI: https://doi.org/10.1103/RevModPhys.79.1217.

[24] QuTech Academy. *Electron Spin Qubits*. YouTube Video. Accessed: October 17, 2025. Aug. 2021. URL: https://www.youtube.com/watch?v=Re4l22ycc-k.

[25] D. Loss and D.P. DiVincenzo. "Quantum computation with quantum dots." In: *Physical Review A* 57.1 (1998). DOI: https://doi.org/10.1103/PhysRevA.57.120.

[26] W.F. van Dorp et al. "Focused electron beam induced processing and the effect of substrate thickness revisited." In: *Nanotechnology* 24.34 (2013). DOI: https://iopscience.iop.org/article/10.1088/0957-4484/24/34/345301.

[27] S. Moshkalev I. Utke and P. Russell. *Nanofabrication Using Focused Ion and Electron Beams: Principles and Applications*. Oxford University Press, 2012. URL: https://scholar.google.com/scholar_lookup?hl=en&publication_year=2012&author=I.+Utke&author=S.+Moshkalev&author=P.+Russell&title=Nanofabrication+Using+Focused+Ion+and+Electron+Beams%3A+Principles+and+Applications.

[28] J. M. Teresa et al. "Review of magnetic nanostructures grown by focused electron beam induced deposition (FEBID)." In: *Journal of Physics D: Applied Physics* 49.24 (2016). DOI: https://iopscience.iop.org/article/10.1088/0022-3727/49/24/243003.

[29] L. Žaper et al. "Scanning Nitrogen-Vacancy Magnetometry of Focused-Electron-Beam-Deposited Cobalt Nanomagnets." In: *ACS Applied Nano Materials* 7.4 (2024). DOI: https://doi.org/10.1021/acsanm.3c05470.

[30] L. Serrano-Ramón et al. "Ultrasmall Functional Ferromagnetic Nanostructures Grown by Focused Electron-Beam-Induced Deposition." In: *ACS Nano* 5.10 (2011). DOI: https://doi.org/10.1021/nn201517r.

[31] Z. Chen et al. "Electron ptychography achieves atomic-resolution limits set by lattice vibrations." In: *Science* 372.6544 (2021). DOI: https://doi.org/10.1126/science.abg2533.

[32] Nano Imaging Lab. *REM FEI Helios Nano Lab 650*. 2024. URL: https://nanoscience.unibas.ch/en/services/nano-imaging-lab/technologien/rem-und-kryo-rem/rem-fei-helios-nano-lab-650/.

[33] W.F. van Dorp and C.W. Hagen. "A critical literature review of focused electron beam induced deposition." In: *Journal of Applied Physics* 104.8 (2008). DOI: https://doi.org/10.1063/1.2977587.

[34] F. Cicoira. "Electron Beam Induced Deposition of Rhodium Nanostructures (thesis)(2002)." PhD thesis. EPFL Lausanne, Switzerland, 2002. DOI: https://infoscience.epfl.ch/handle/20.500.14299/211497.

[35] T. Koshikawa and R. Shimizu. "A Monte Carlo calculation of low-energy secondary electron emission from metals." In: *Journal of Physics D: Applied Physics* 7.9 (1974). DOI: https://doi.org/10.1093/oso/9780195088748.001.0001.

[36] M. Kotera. "A Monte Carlo simulation of primary and secondary electron trajectories in a specimen." In: *Journal of applied physics* 65.10 (1989). DOI: https://doi.org/10.1063/1.343341.

[37] D.C. Joy. *Monte Carlo modeling for electron microscopy and microanalysis*. Vol. 9. Oxford University Press, 1995. DOI: https://doi.org/10.1093/oso/9780195088748.001.0001.

[38] N. Silvis-Cividjian C.W. Hagen and P. Kruit. "Resolution limit for Electron-Beam-Induced-Deposition on thick substrates." In: *Scanning: the journal of scanning microscopies* 27.2 (2005). DOI: https://doi.org/10.1002/sca.4950280402.

[39] H. Koops V. Scheuer and T. Tschudi. "Electron beam decomposition of carbonyls on silicon." In: *Microelectronic Engineering* 5.1-4 (1986).

[40] S. Hari et al. "Sidewall angle tuning in focused electron beam-induced processing." In: *Beilstein Journal of Nanotechnology* 15 (2024). URL: https://doi.org/10.3762/bjnano.15.40.

[41] J.W. Hinum-Wagner et al. "The Influence of Substrate Temperature during Focused Electron Beam Induced Deposition (FEBID)." In: *Workshop Handbook: Program and Abstract*. 2019. URL: https://pure.tugraz.at/ws/portalfiles/portal/23129800/2019_ASEM.pdf.

[42] E. Mutunga et al. "Impact of electron-beam heating during 3D nanoprinting." In: *ACS nano* 13.5 (2019). DOI: https://doi.org/10.1021/acsnano.8b09341.

[43] M. Bresin et al. "Direct-write 3D nanolithography at cryogenic temperatures." In: *Nanotechnology* 24.3 (2013). URL: https://iopscience.iop.org/article/10.1088/0957-4484/24/3/035301.

[44] M. Gavagnin et al. "Synthesis of individually tuned nanomagnets for nanomagnet logic by direct write focused electron beam induced deposition." In: *ACS nano* 7.1 (2013). DOI: https://doi.org/10.1021/nn305079a.

[45] M.V. Puydinger dos Santos et al. "Annealing-based electrical tuning of cobalt–carbon deposits grown by focused-electron-beam-induced deposition." In: *ACS applied materials & interfaces* 8.47 (2016). DOI: https://doi.org/10.1021/acsami.6b12192.

[46] C. Magén J. Pablo-Navarro and J.M. De Teresa. "Purified and crystalline three-dimensional electron-beam-induced deposits: the successful case of cobalt for high-performance magnetic nanowires." In: *ACS Applied Nano Materials* 1.1 (2017). DOI: https://doi.org/10.1021/acsanm.7b00016.

[47] S. Hong et al. "Nanoscale magnetometry with NV centers in diamond." In: *MRS bulletin* 38.2 (2013). DOI: https://doi.org/10.1557/mrs.2013.23.

[48] L. Rondin et al. "Magnetometry with nitrogen-vacancy defects in diamond." In: *Reports on Progress in Physics* 77.5 (2014). DOI: http://iopscience.iop.org/0034-4885/77/5/056503.

[49] E. Marchiori et al. "Nanoscale magnetic field imaging for 2D materials." In: *Nature Reviews Physics* (2021). DOI: https://doi.org/10.1038/s42254-021-00380-9.

[50] M.W. Doherty et al. "The nitrogen-vacancy colour centre in diamond." In: *Physics Reports* 528.1 (2013). DOI: https://doi.org/10.1016/j.physrep.2013.02.001.

[51] Qnami. *The NV center*. 2020. URL: https://qnami.ch/wp-content/uploads/2020/12/2020-12-07-Qnami-TN1-The-NV-center-1.pdf.

[52] K. Bian et al. "Nanoscale electric-field imaging based on a quantum sensor and its charge-state control under ambient condition." In: *Nature Communications* 12.1 (2021). DOI: https://doi.org/10.1038/s41467-021-22709-9.

[53] H.P. Paudel et al. "Sensing at the Nanoscale Using Nitrogen-Vacancy Centers in Diamond: A Model for a Quantum Pressure Sensor." In: *Nanomaterials* 14.8 (2024). DOI: https://doi.org/10.3390/nano14080675.

[54] D. Wu et al. "High-sensitivity temperature sensing on an ensemble of nitrogen-vacancy centers in diamond." In: *Japanese Journal of Applied Physics* 61.8 (2022). URL: https://iopscience.iop.org/article/10.35848/1347-4065/ac7a7b/meta?casa_token=TudWhCJH1YcAAAAA:

kWeU5JSGobk--SRgmuTaGFVvFdF291ls5cn2BKGYR6q1Lv6aoc2XnV7ZvDVzX2qL1pFLtJ37mm
mbqL-H_y-N.

[55] A. Finco et al. "Imaging non-collinear antiferromagnetic textures via single spin relaxometry." In: *Nature Communications* 12.1 (2021). DOI: https://doi.org/10.1038/s41467-021-20995-x.

[56] M. Cheng et al. "Practical medical applications of quantitative MR relaxometry." In: *Journal of Magnetic Resonance Imaging* 36.4 (2012). DOI: https://doi.org/10.1002/jmri.23718.

[57] S. Hari et al. "A study of the reproducibility of electron beam induced deposition for sub-20 nm lithography." In: *Micro and Nano Engineering* 4 (2019). DOI: https://doi.org/10.1016/j.mne.2019.04.003.

[58] S. Hari et al. "Combined focused electron beam-induced deposition and etching for the patterning of dense lines without interconnecting material." In: *Micromachines* 12.1 (2020), p. 8. DOI: https://doi.org/10.3390/mi12010008.

[59] S. Sangiao et al. "Magnetic properties of optimized cobalt nanospheres grown by focused electron beam induced deposition (FEBID) on cantilever tips." In: *Beilstein Journal of Nanotechnology* 8.1 (2017). DOI: https://doi.org/10.3762/bjnano.8.210.

[60] Royal Society of Chemistry. *Cobalt Properties and Applications*. 2024. URL: https://www.rsc.org/periodic-table/element/27/cobalt.

[61] SAMaterials. *What is Cobalt Used in Everyday Life*. 2024. URL: https://www.samaterials.com/content/what-is-cobalt-used-in-everyday-life.html.

[62] J. Baylis and J. Constantinides. *Cobalt Essential to High-Performance Magnetics*. 2012. URL: https://www.arnoldmagnetics.com/wp-content/uploads/2017/10/Cobalt-Essential-to-High-Performance-Magnetics-Baylis-and-Constantinides-Cobalt-Conference-2012.-psn-hi-res.pdf.

[63] M. Ayadi et al. "Face centered cubic cobalt layer on Au(111): a magneto-optical study." In: *Journal of Magnetism and Magnetic Materials* 247.2 (2002). DOI: https://doi.org/10.1016/S0304-8853(02)00183-X.

[64] J. Balcerski W. Koz lowski and W. Szmaja. "Study of nanocrystalline thin cobalt films with perpendicular magnetic anisotropy obtained by thermal evaporation." In: *Journal of Magnetism and Magnetic Materials* 423 (2017). DOI: https://doi.org/10.1016/j.jmmm.2016.09.111.

[65] M. Cerisier et al. "Structure and magnetic properties of electrodeposited Co films onto Si(100)." In: *Applied Surface Science* 166.1 (2000). DOI: https://doi.org/10.1016/S0169-4332(00)00398-6.

[66] Y.K. Ko et al. "Studies of cobalt thin films deposited by sputtering and MOCVD." In: *Materials Chemistry and Physics* 80.2 (2003). DOI: https://doi.org/10.1016/S0254-0584(03)00085-3.

[67] M. Hehn et al. "Nanoscale magnetic domain structures in epitaxial cobalt films." In: *Physical Review B* 54 (1996). DOI: https://doi.org/10.1103/PhysRevB.54.3428.

[68] J. Brandenburg et al. "Domain structure of epitaxial Co films with perpendicular anisotropy." In: *Physical Review B* 79 (2009). DOI: https://doi.org/10.1103/PhysRevB.79.054429.

[69] J. M. De Teresa et al. "Review of magnetic nanostructures grown by focused electron beam induced deposition (FEBID)." In: *Journal of Physics D: Applied Physics* 49.24 (2016). DOI: https://dx.doi.org/10.1088/0022-3727/49/24/243003.

[70] L. Skoric et al. "Layer-by-layer growth of complex-shaped three-dimensional nanostructures with focused electron beams." In: *Nano Letters* 20.1 (2019). DOI: https://pubs.acs.org/doi/10.1021/acs.nanolett.9b03565.

[71] C. Magén et al. "Focused-Electron-Beam Engineering of 3D Magnetic Nanowires." In: *Nanomaterials* 11.2 (2021). DOI: https://doi.org/10.3390/nano11020402.

[72] J.M. De Teresa et al. "Comparison between Focused Electron/Ion Beam-Induced Deposition at Room Temperature and under Cryogenic Conditions." In: *Micromachines* 10.12 (2019). DOI: https://doi.org/10.3390/mi10120799.

[73] J.A. Sidles et al. "Magnetic resonance force microscopy." In: *Reviews of Modern Physics* 67.1 (1995). DOI: https://doi.org/10.1103/RevModPhys.67.249.

[74] C. L. Degen et al. "Nanoscale magnetic resonance imaging." In: *Proceedings of the National Academv of Sciences of the United States of America* 106.5 (2009). DOI: https://doi.org/10.1073/pnas.081206810.

[75] J.C. Slonczewski. "Current-driven excitation of magnetic multilayers." In: *Journal of Magnetism and Magnetic Materials* 159.1-2 (1996). DOI: https://doi.org/10.1016/0304-8853(96)00062-5.

[76] P. Rabl et al. "A quantum spin transducer based on nanoelectromechanical resonator arrays." In: *Nature Physics* 6.8 (2010). DOI: https://doi.org/10.1038/nphys1679.

[77] J. Gieseler et al. "Single-spin magnetomechanics with levitated micromagnets." In: *Physical Review Letters* 124.16 (2020). DOI: https://doi.org/10.1103/PhysRevLett.124.163604.

[78] E. Rosenfeld et al. "Efficient entanglement of spin qubits mediated by a hot mechanical oscillator." In: *Physical Review Letters* 126.25 (2021). DOI: https://doi.org/10.1103/PhysRevLett.126.250505.

[79] X.F. Pan et al. "Enhanced spin-mechanical interaction with levitated micromagnets." In: *Physical Review A* 107.2 (2023). DOI: https://doi.org/10.1103/PhysRevA.107.023722.

[80] D. Visani et al. "Near-resonant nuclear spin detection with high-frequency mechanical resonators." In: *arXiv preprint arXiv:2311.16273* (2023). DOI: https://doi.org/10.48550/arXiv.2311.16273.

[81] D. Hälg et al. "Membrane-based scanning force microscopy." In: *Physical Review Applied* 15.2 (2021). DOI: https://doi.org/10.1103/PhysRevApplied.15.L021001.

[82] R. Budakian et al. "Roadmap on nanoscale magnetic resonance imaging." In: *Nanotechnology* (2024). URL: https://iopscience.iop.org/article/10.1088/1361-6528/ad4b23/meta.

[83] Niels Bohr Institute. *Quantum Optomechanics Group at NBI*. https://nbi.ku.dk/english/research/quantum-optics-and-photonics/quantum-optomechanics/. 2024.

[84] Y. Tsaturyan et al. "Ultracoherent nanomechanical resonators via soft clamping and dissipation dilution." In: *Nature Nanotechnology* 12.8 (2017). DOI: https://doi.org/10.1038/nnano.2017.101.

[85] A.D. O'Connell et al. "Quantum ground state and single-phonon control of a mechanical resonator." In: *Nature* 464.7289 (2010). DOI: https://doi.org/10.1038/nature08967.

[86] D. Hälg et al. "Strong parametric coupling between two ultracoherent membrane modes." In: *Physical Review Letters* 128.9 (2022). DOI: https://doi.org/10.1103/PhysRevLett.128.094301.

[87] A. Beccari N.J. Engelsen and T.J. Kippenberg. "Ultrahigh-quality-factor micro-and nanomechanical resonators using dissipation dilution." In: *Nature Nanotechnology* (2024). DOI: https://doi.org/10.1038/s41565-023-01597-8.

[88] D. Rohner et al. "(111)-oriented, single crystal diamond tips for nanoscale scanning probe imaging of out-of-plane magnetic fields." In: *Applied Physics Letters* 115.19 (2019). DOI: https://doi.org/10.1063/1.5127101.

[89] S. Philipp. "Magnetism of Nano-to Micrometer-Sized Anisotropic Materials." PhD thesis. University_of_Basel, 2022. URL: https://edoc.unibas.ch/89078/1/PhilippThesis_edoc.pdf.

[90] S. Bravyi et al. "High-threshold and low-overhead fault-tolerant quantum memory." In: *Nature* 627.8005 (2024). DOI: https://doi.org/10.1038/s41586-024-07107-7.

[91] E. Kawakami et al. "Electrical control of a long-lived spin qubit in a Si/SiGe quantum dot." In: *Nature Nanotechnology* 9.9 (2014). DOI: https://doi.org/10.1038/nnano.2014.153.

[92] P. Scarlino et al. "Dressed photon-orbital states in a quantum dot: Intervalley spin resonance." In: *Physical Review B* 95.16 (2017). DOI: https://doi.org/10.1103/PhysRevB.95.165429.

[93] O. Bulancea-Lindvall et al. "Isotope-Purification-Induced Reduction of Spin-Relaxation and Spin-Coherence Times in Semiconductors." In: *Physical Review Applied* 19.6 (2023). DOI: https://doi.org/10.1103/PhysRevApplied.19.064046.

[94] R. Neumann and L. R. Schreiber. "Simulation of micro-magnet stray-field dynamics for spin qubit manipulation." In: *Journal of Applied Physics* 117.19 (2015). DOI: https://doi.org/10.1063/1.4921291.

[95] H. Kiyama S. Nakamura and A. Oiwa. "Micromagnet design for addressable fast spin manipulations in a 2× 2 quantum dot array." In: *Journal of Applied Physics* 132.22 (2022). DOI: https://doi.org/10.1063/5.0088840.

[96] M. Aldeghi, R. Allenspach, and G.Salis. "Modular nanomagnet design for spin qubits confined in a linear chain." In: *Applied Physics Letters* 122.13 (2023). DOI: https://doi.org/10.1063/5.0139670.

[97] Y. Tokura et al. "Coherent single electron spin control in a slanting Zeeman field." In: *Physical Review Letters* 96.4 (2006). DOI: https://doi.org/10.1103/PhysRevLett.96.047202.

[98] R. Brunner et al. "Two-qubit gate of combined single-spin rotation and interdot spin exchange in a double quantum dot." In: *Physical Review Letters* 107.14 (2011). DOI: https://doi.org/10.1103/PhysRevLett.107.146801.

[99] H. Ibach and H. Lüth. *Solid-State Physics: An Introduction to Principles of Materials Science*. Springer Science & Business Media, 2013. DOI: https://doi.org/10.1007/978-3-642-88199-2.

[100] A. Fernández-Pacheco et al. "Magnetotransport properties of high-quality cobalt nanowires grown by focused-electron-beam-induced deposition." In: *J. Phys. D: Appl. Phys.* 42.5 (2009). DOI: https://doi.org/10.1088/0022-3727/42/5/055005.

[101] T. Farrel J.E.A. Alderson and C.M. Hurd. "Hall coefficients of Cu, Ag, and Au in the range 4.2-300 K." In: *Physical Review Journals Archive* 174.3 (1968). DOI: https://doi.org/10.1103/PhysRev.174.729.

[102] Y. Mokrousov E. Roman and I. Souza. "Orientation dependence of the intrinsic anomalous Hall effect in hcp cobalt." In: *Physical Review Letters* 103.9 (2009), p. 097203. DOI: https://doi.org/10.1103/PhysRevLett.103.097203.

[103] J. M. Binder et al. "Qudi: A modular python suite for experiment control and data processing." In: *SoftwareX* 6 (2017). DOI: https://doi.org/10.1016/j.softx.2017.02.001.

[104] J.R. Petta et al. "Coherent manipulation of coupled electron spins in semiconductor quantum dots." In: *Science* 309.5744 (2005). DOI: https://www.science.org/doi/10.1126/science.1116955.

[105] T. Nakajima et al. "Coherence of a Driven Electron Spin Qubit Actively Decoupled from Quasistatic Noise." In: *Physical Review X* 10.1 (2020). DOI: https://link.aps.org/doi/10.1103/PhysRevX.10.011060.

[106] A. Fernández-Pacheco et al. "Writing 3D Nanomagnets Using Focused Electron Beams." In: *Materials* 13.17 (2020). DOI: https://doi.org/10.3390/ma13173774.

[107] R. Winkler V. Reisecker and Harald Plank. "A Review on Direct-Write Nanoprinting of Functional 3D Structures with Focused Electron Beams." In: *Advanced Functional Materials* (2024). DOI: https://doi.org/10.1002/adfm.202407567.

[108] C. Donnelly et al. "Complex free-space magnetic field textures induced by three-dimensional magnetic nanostructures." In: *Nature Nanotechnology* 17.2 (2022). DOI: https://doi.org/10.1038/s41565-021-01027-7.

[109] D. Sanz-Hernández et al. "Artificial double-helix for geometrical control of magnetic chirality." In: *ACS nano* 14.7 (2020). DOI: https://doi.org/10.1021/acsnano.0c00720.

[110] L. Skoric et al. "Domain wall automotion in three-dimensional magnetic helical interconnectors." In: *ACS nano* 16.6 (2022). DOI: https://doi.org/10.1021/acsnano.1c10345.

[111] A. Kuprava and M. Huth. "Fast and Efficient Simulation of the FEBID Process with Thermal Effects." In: *Nanomaterials* 13.5 (2023). DOI: https://doi.org/10.3390/nano13050858.

[112] E. Berganza et al. "Half-hedgehog spin textures in sub-100 nm soft magnetic nanodots." In: *Nanoscale* 12.36 (2020). DOI: https://doi.org/10.1039/D0NR02173C.

[113] H.J. Mamin P. Grütter and D. Rugar. "Magnetic force microscopy (MFM)." In: *Scanning Tunneling Microscopy II: Further applications and related scanning techniques*. Springer, 1992. DOI: https://link.springer.com/chapter/10.1007/978-3-642-97363-5_5.

[114] H.J. Hug. "Mapping the magnetic field of skyrmions and spin spirals by scanning probe microscopy." In: *Magnetic Skyrmions and Their Applications* (2021). DOI: https://doi.org/10.1016/B978-0-12-820815-1.00016-X.

[115] C.H. Marrows et al. "Neuromorphic computing with spintronics." In: *npj Spintronics* 2.1 (2024). DOI: https://doi.org/10.1038/s44306-024-00019-2.

[116] J. Puebla et al. "Spintronic devices for energy-efficient data storage and energy harvesting." In: *Communications Materials* 1.1 (2020). DOI: https://doi.org/10.1038/s43246-020-0022-5.

[117] J. Grollier et al. "Neuromorphic spintronics." In: *Nature Electronics* 3.7 (2020). DOI: https://doi.org/10.1038/s41928-019-0360-9.

[118] J. Torrejon et al. "Neuromorphic computing with nanoscale spintronic oscillators." In: *Nature* 547.7664 (2017). DOI: https://doi.org/10.1038/nature23011.

[119] V.K. Khanna. *Integrated Nanoelectronics: Nanoscale CMOS, Post-CMOS and Allied Nanotechnologies*. Springer, 2016. DOI: https://doi.org/10.1007/978-81-322-3625-2.

[120] K. Cai et al. "Spin-based magnetic random-access memory for high-performance computing." In: *National Science Review* 11.3 (2024). DOI: https://doi.org/10.1093/nsr/nwad272.

[121] N. Reyren A. Fert and V. Cros. "Magnetic skyrmions: advances in physics and potential applications." In: *Nature Reviews Materials* 2.7 (2017). DOI: https://doi.org/10.1038/natrevmats.2017.31.

[122] Y. Tokura and N. Kanazawa. "Magnetic skyrmion materials." In: *Chemical Reviews* 121.5 (2020). DOI: https://doi.org/10.1021/acs.chemrev.0c00297.

[123] N. Nagaosa and Y. Tokura. "Topological properties and dynamics of magnetic skyrmions." In: *Nature Nanotechnology* 8.12 (2013). DOI: https://doi.org/10.1038/nnano.2013.243.

[124] W. Koshibae et al. "Memory functions of magnetic skyrmions." In: *Japanese Journal of Applied Physics* 54.5 (2015). URL: https://iopscience.iop.org/article/10.7567/JJAP.54.053001.

[125] S. Mühlbauer et al. "Skyrmion lattice in a chiral magnet." In: *Science* 323.5916 (2009). DOI: https://www.science.org/doi/10.1126/science.1166767.

[126] X.Z. Yu et al. "Real-space observation of a two-dimensional skyrmion crystal." In: *Nature* 465.7300 (2010). DOI: https://doi.org/10.1038/nature09124.

[127] E. Berganza et al. "3D quasi-skyrmions in thick cylindrical and dome-shape soft nanodots." In: *Scientific reports* 12.1 (2022). DOI: https://doi.org/10.1038/s41598-022-07407-w.

[128] M. Goiriena-Goikoetxea et al. "Magnetization reversal in circular vortex dots of small radius." In: *Nanoscale* 9.31 (2017). DOI: https://doi.org/10.1039/C7NR02389H.

[129] T. Okuno et al. "MFM study of magnetic vortex cores in circular permalloy dots: behavior in external field." In: *Journal of Magnetism and Magnetic Materials* 240.1-3 (2002). DOI: https://doi.org/10.1016/S0304-8853(01)00708-9.

[130] N. Rossi. "Force sensing with nanowires." PhD thesis. University_of_Basel, 2019. URL: http://edoc.unibas.ch/diss/DissB_73768.

[131] H. Mattiat et al. "Nanowire magnetic force sensors fabricated by focused-electron-beam-induced deposition." In: *Physical Review Applied* 13.4 (2020). DOI: https://doi.org/10.1103/PhysRevApplied.13.044043.

[132] Maxime Rollo et al. "Quantitative study of the response of a single NV defect in diamond to magnetic noise." In: *Physical Review B* 103.23 (2021), p. 235418.

[133] Junjia Ding et al. "Spin vortex resonance in non-planar ferromagnetic dots." In: *Scientific reports* 6.1 (2016), p. 25196.

[134] Sang-Koog Kim et al. "Resonantly excited precession motion of three-dimensional vortex core in magnetic nanospheres." In: *Scientific reports* 5.1 (2015), p. 11370.

[135] SS Cherepov et al. "Core-core dynamics in spin vortex pairs." In: *Physical Review Letters* 109.9 (2012), p. 097204.

[136] R Badea, E Haber, and J Berezovsky. "Stochastic Dynamics of a Ferromagnetic Vortex Revealed by Single-Spin Magnetometry." In: *Physical Review Applied* 10.6 (2018), p. 064031.

[137] Toeno Van der Sar et al. "Nanometre-scale probing of spin waves using single electron spins." In: *Nature communications* 6.1 (2015), p. 7886.

[138] L. Körber et al. "Symmetry and curvature effects on spin waves in vortex-state hexagonal nanotubes." In: *Physical Review B* 104.18 (2021). DOI: https://doi.org/10.1103/PhysRevB.104.184429.

[139] J.M. De Teresa and R. Cordoba. "Arrays of densely packed isolated nanowires by focused beam induced deposition plus Ar+ milling." In: *ACS nano* 8.4 (2014). DOI: https://doi.org/10.1021/nn500525k.